Elastic J/ψ production at HERA

DISSERTATION

zur Erlangung des Doktorgrades
des Fachbereichs Physik
der Universität Hamburg

vorgelegt von

PHILIPP FLEISCHMANN

aus Hamburg

Hamburg
2004

Abstract

In this thesis an analysis of diffractive J/ψ photoproduction and electroproduction in ep-collisions is presented. The data were collected with the H1 detector and correspond to an integrated luminosity of $54.79\,\mathrm{pb}^{-1}$. The kinematic range covers the region of $40\,\mathrm{GeV} < W < 160\,\mathrm{GeV}$ and $-t < 1.2\,\mathrm{GeV}^2$, where W is the centre-of-mass energy in the photon-proton system and $-t$ is the squared four-momentum transfer at the proton vertex. The photon virtuality is $Q^2 < 1\,\mathrm{GeV}^2$ for J/ψ photoproduction and $2\,\mathrm{GeV}^2 < Q^2 < 80\,\mathrm{GeV}^2$ in the region of deep inelastic scattering.

Elastic photon-proton cross sections are derived as a function of W, $-t$ and Q^2 in both regions. Also the effect of shrinkage i.e. the change of the t dependence with W, is studied. For this purpose the t dependence of the cross section is measured as a function of W and vice versa. For the first time at H1 shrinkage is also measured for J/ψ electroproduction. All results in both kinematic regions are compared with each other, with previous results from H1 and ZEUS as well as with predictions from different theoretical models.

The W dependence of the elastic J/ψ photoproduction cross section, parameterised as W^δ, is measured as $\delta = 0.71 \pm 0.04 \pm 0.07$. No Q^2 dependence of δ is observed within errors. In the region of deep inelastic scattering $\delta = 0.78 \pm 0.15 \pm 0.09$ is found. The t dependence of the differential J/ψ cross section is well described by e^{bt} yielding a value of $b = 4.57 \pm 0.07 \pm 0.14\,\mathrm{GeV}^{-2}$ for J/ψ photoproduction and $b = 4.10 \pm 0.16 \pm 0.20\,\mathrm{GeV}^{-2}$ for J/ψ electroproduction. The analysis of the W dependence of the slope parameter b yields an effective Pomeron trajectory slope of $\alpha' = 0.177 \pm 0.034 \pm 0.017\,\mathrm{GeV}^{-2}$ for J/ψ photoproduction. For J/ψ electroproduction $\alpha' = 0.018 \pm 0.103 \pm 0.064\,\mathrm{GeV}^{-2}$ is derived, compatible with no shrinkage.

The helicity structure of diffractive J/ψ production is analysed. Differential photon-proton cross sections are calculated as a function of three different angles which describe the process. The results are compared to previous measurements and the assumption of s-channel helicity conservation. For J/ψ photoproduction the assumption is confirmed, while for deep inelastic scattering small deviations are visible.

Kurzfassung

In dieser Arbeit wird die diffraktive Produktion von J/ψ-Mesonen im Bereich der Photoproduktion sowie im Bereich der tief-inelastischen Streuung bei ep-Kollisionen untersucht. Die analysierten Daten wurden mit dem H1 Detektor gemessen und entsprechen einer integrierten Luminosität von $54.79\,\mathrm{pb}^{-1}$. Der abgedeckte kinematische Bereich erstreckt sich über $40\,\mathrm{GeV} < W < 160\,\mathrm{GeV}$ und $-t < 1.2\,\mathrm{GeV}^2$. Dabei ist W die Schwerpunktsenergie des Photon-Proton-Systems und $-t$ ist der quadrierte Impulsübertrag am Protonvertex. Die Virtualität des Photons beträgt $Q^2 < 1\,\mathrm{GeV}^2$ für die J/ψ-Photoproduktion und $2\,\mathrm{GeV}^2 < Q^2 < 80\,\mathrm{GeV}^2$ im Bereich der tief-inelastischen Streuung.

Elastische Photon-Proton-Wirkungsquerschnitte werden als Funktion von W, $-t$ und Q^2 in beiden kinematischen Bereichen bestimmt. Auch der Effekt der Energieabhängigkeit der t-Verteilung (*shrinkage*) wird für die J/ψ-Photoproduktion, sowie erstmals bei H1 auch für die J/ψ-Elektroproduktion gemessen. Dazu wird die t-Abhängigkeit als Funktion von W und umgekehrt analysiert. Ein Vergleich mit Ergebnissen früherer Analysen sowie einigen Vorhersagen verschiedener theoretischer Modelle wird durchgeführt.

Die W-Abhängigkeit der elastischen J/ψ Photoproduktion wird durch den Ansatz W^δ mit $\delta = 0.71 \pm 0.04 \pm 0.07$ gut beschrieben. Eine Q^2-Abhängigkeit des Steigungsparameters δ wird innerhalb der Fehler nicht beobachtet. Im Bereich der tief-inelastischen Streuung wird ein Wert von $\delta = 0.78 \pm 0.15 \pm 0.09$ gemessen. Die t-Abhängigkeit des differentiellen J/ψ Wirkungsquerschnitts läßt sich durch e^{bt} beschreiben und liefert für die Photoproduktion einen Wert von $b = 4.57 \pm 0.07 \pm 0.14\,\mathrm{GeV}^{-2}$ und für die J/ψ Elektroproduktion ergibt sich $b = 4.10 \pm 0.16 \pm 0.20\,\mathrm{GeV}^{-2}$. Die Analyse der W-Abhängigkeit des Steigungsparameters b ergibt eine effektive Pomeron-Trajektorie mit einer Steigung $\alpha' = 0.18 \pm 0.03 \pm 0.02\,\mathrm{GeV}^{-2}$ für J/ψ Photoproduktion. Für die J/ψ Elektroproduktion ergibt sich $\alpha' = 0.018 \pm 0.103 \pm 0.064\,\mathrm{GeV}^{-2}$.

Desweiteren wird die Zerfallswinkelverteilung der diffraktiven J/ψ-Produktion untersucht. Dafür werden differentielle Photon-Proton Wirkungsquerschnitte berechnet als Funktion dreier Winkel, die den Produktionsprozess charakterisieren. Die Ergebnisse werden mit früheren Messungen verglichen, sowie mit der Annahme der Helizitätserhaltung im s-Kanal. Diese Annahme wird für die J/ψ-Photoproduktion durch die Daten bestätigt. Im Bereich der Tiefinelastischen Streuung sind jedoch leichte Abweichungen erkennbar.

Contents

Introduction

The goal of high energy physics is to improve our understanding of the fundamental constituents of matter and the forces between them. High energies are necessary to create heavy particles and to explore the structure of hadrons. The HERA collider with its experiments offers the possibility to probe and improve our understanding of the interactions in electron-proton collisions.

Since 1992 the experiments at HERA are analysing proton structure functions and hadronic final states. One type of reactions was observed, which showed many characteristics of optical diffraction and are therefore referred to as diffractive processes. Diffraction was previously observed in hadron-hadron collisions and is successfully described in the framework of Regge theory. In diffractive interactions with real and virtual photons at fixed target experiments vector mesons can be formed, carrying the same quantum numbers as the exchanged photon. The phenomenology can be related to hadron-hadron interaction via the Vector-Meson-Dominance-Model. However, at HERA energies some discrepancies in the description of the production of heavy vector mesons have been observed. More recent models successfully describe diffractive processes within the language of Quantum Chromodynamics (QCD), where in the simplest case the interaction is modelled by the exchange of a system of two gluons. In the case of heavy vector mesons, like the J/ψ, it has been found that perturbative calculations are applicable.

In this thesis the diffractive production of J/ψ mesons is analysed using data collected in the years 1999 and 2000 with the H1 detector. Two disjoint data samples are analysed. In the photoproduction sample quasi-real photons are emitted from the electron interacting with the proton. The scattered electron is not measured in the main detector. In the second sample, referred to as the region of deep inelastic scattering, the exchanged photon is virtual. In this region the scattered electron is observed in the main detector.

In the present analysis the J/ψ is detected via its decay into two muons which gives a clean experimental signature in the detector. In elastic J/ψ production the proton stays intact and scatters undetected under small angles into the beam pipe. Events in which the proton dissociates into a low-mass exited final state form the largest background contribution. The main focus in the present analysis is on elastic J/ψ production. Only for a part of this thesis the cross sections of the combined elastic and proton dissociative J/ψ production are used to analyse the helicity structure of diffractive J/ψ production.

Elastic J/ψ production has already been subject of a few analyses at HERA. In this thesis an effort is made to further reduce the systematic uncertainties and to make use of the increased statistics. The largest systematic uncertainties in previous analyses have

originated from the identification of the decay leptons and from the separation of the elastic events from those with proton dissociation.

The thesis starts with an overview of the phenomenological description of diffractive J/ψ production processes. Predictions of different theoretical models concerning the kinematic range of this analysis are presented. Also the Monte Carlo simulations used in this analysis are introduced.

In chapter 2 an overview of the ep-collider HERA and the H1 detector is given. The detector components relevant to this analysis are briefly described.

A detailed description of the data selection is given in chapter 3. The main emphasis in this chapter is on the rejection of background coming from cosmic ray muons.

An important part of this thesis is the determination of the detector efficiencies concerning the muon identification, the triggering and the separation of elastic and proton dissociative events as well as their description in the MC simulation. These are presented in chapter 4. Here the calculation of the cross section and the estimation of the systematic uncertainties is described.

In chapter 5 all results on the elastic diffractive J/ψ production are presented. First the J/ψ photoproduction is studied and compared to previous measurements as well as theoretical predictions. Then the J/ψ electroproduction is analysed and compared to the results of photoproduction. Also a comparison to published measurements from the H1 and ZEUS collaborations as well as to theoretical predictions is performed. In both kinematic regions the helicity structure of the diffractive J/ψ production is analysed and compared to previous measurements and theoretical predictions.

Finally the whole analysis and its results are summarised.

1 Charmonium Production

In this chapter an overview of the theory and phenomenology of diffractive J/ψ production in ep-collisions is given. After introducing the variables relevant to this analysis, the diffractive J/ψ production process is described. Different theoretical models are briefly summarised. At the end of this chapter a description of the Monte Carlo event generators that are used to model the theoretical predictions is given.

1.1 Kinematics
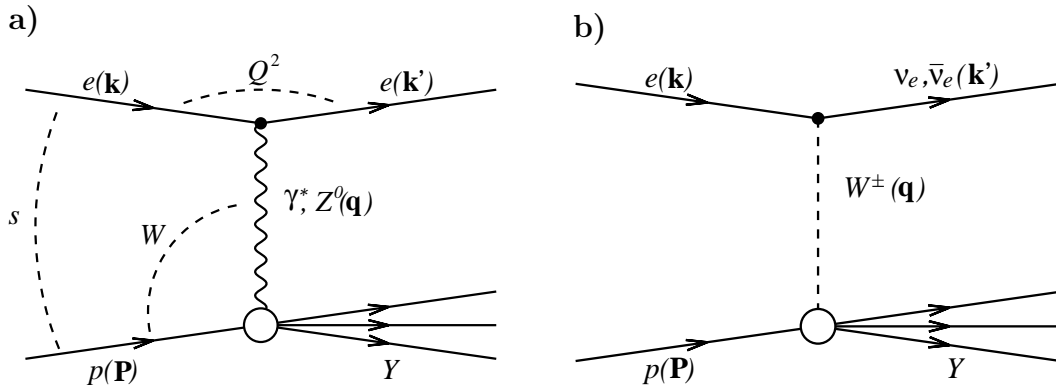
Figure 1.1: ep-scattering Feynman diagrams for a) the neutral current process and b) the charged current process.

In ep-scattering two different types of processes are distinguished:

$$(NC) \qquad e + p \quad \to \quad e + \text{hadrons}$$
$$(CC) \qquad e + p \quad \to \quad \nu_e + \text{hadrons}$$

The neutral current (NC) process is mediated by the exchange of a virtual photon γ^* or a Z^0 gauge boson. The charged current (CC) process is mediated by the exchange of a $W^\pm$ gauge boson, depending on the charge of the lepton beam. Figures 1.1 a) and b) show the first order Feynman diagrams of both processes. In the charged current case an electron neutrino is produced at the eW-vertex which cannot be directly detected.

In the kinematic region relevant for the present analysis at low Q^2 the exchange of a Z^0 or a $W^\pm$ gauge boson is suppressed relative to the photon exchange. Therefore only the

neutral current process via the exchange of a photon is discussed. The processes can be described by a set of variables indicated in figure 1.1 a):

The centre-of-mass energy squared s of the ep-system is given by

$$s = (\mathbf{k} + \mathbf{P})^2 \approx 4E_e E_p \tag{1.1}$$

where $\mathbf{k}$ and $\mathbf{P}$ are the four-momenta of the incoming electron and the incoming proton respectively. E_e and E_p are the beam energies of the electron and the proton beam respectively. The approximation neglects the masses of the electron and proton.

The four-momentum transfer squared at the electron vertex Q^2 is defined by

$$Q^2 = -\mathbf{q}^2 = -(\mathbf{k} - \mathbf{k}')^2$$

where $\mathbf{q}$ and $\mathbf{k}'$ are the four-momenta of the emitted photon and the scattered electron respectively. Q^2 is often referred to as the photon *virtuality*. It can also be written in terms of the Bjorken scaling variable x and the inelasticity y:

$$
\begin{aligned}
x &= \frac{-\mathbf{q}^2}{2\mathbf{q} \cdot \mathbf{P}} \\
y &= \frac{\mathbf{q} \cdot \mathbf{P}}{\mathbf{k} \cdot \mathbf{P}} \\
Q^2 &= xys
\end{aligned}
$$

In the Quark Parton Model x denotes the fraction of the proton momentum carried by the parton struck by the photon. The fraction of the electron energy transferred to the proton in its rest frame is given by the variable y.

At HERA two regions in Q^2 are defined. In the limit of $Q^2 \to 0$ the exchanged photon is quasi-real. This region is called photoproduction. For large Q^2 virtual photons γ^* are radiated off the lepton and this region is referred to as Deep Inelastic Scattering (DIS). Experimentally the limit between the two regions is $Q^2 \approx 1 - 2\,\mathrm{GeV}^2$ since for $Q^2 \gtrsim 1\,\mathrm{GeV}^2$ the scattered electron is detected in the main detector.

High energy ep-collisions are a source of $\gamma^* p$ collisions. The centre-of-mass energy of the photon-proton-system W is given by

$$W^2 = (\mathbf{P} + \mathbf{q})^2 = Q^2 \cdot \left(\frac{1}{x} - 1\right) + m_p^2$$

where m_p denotes the mass of the proton. Neglecting m_p, in photoproduction this equation reduces to

$$W^2 \approx ys. \tag{1.2}$$

1.2 Diffractive J/ψ Production

The neutral current process $e + p \to e + X$, where X denotes final state hadrons, can be further classified into different types of reactions: inelastic and diffractive processes.
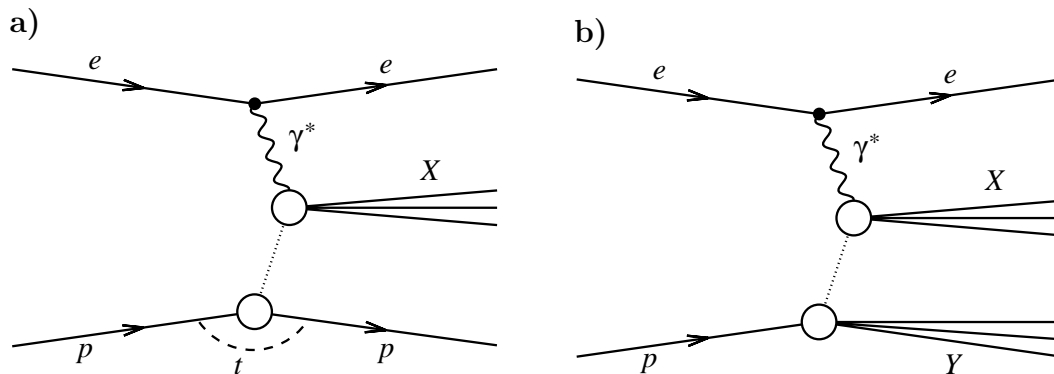
Figure 1.2: Feynman diagrams of diffractive ep-scattering: a) the elastic process and b) the process with proton dissociation.

Figure 1.2 shows the generic graphs of diffractive ep-scattering, which are the subject of this analysis. In experiments diffractive events show a visible gap, *rapidity gap*, between the final states X and Y of the photon and of the proton respectively. Examples of diffractive final states X at HERA are vector mesons or jets. In diffractive processes the incoming proton can remain either completely intact (*elastic* scattering) and is scattered at a small angle, or the proton dissociates giving rise to an excited state Y of low mass with the same quantum numbers as the proton (*proton dissociative* scattering). The four-momentum transfer squared at the proton vertex t is defined by

$$t = (\mathbf{P} - \mathbf{P}')^2$$

where $\mathbf{P}'$ is the four-momentum of the scattered proton [1].

The J/ψ vector meson was discovered in 1974 [1, 2]. It consists of a charm and an anti-charm quark and has an invariant mass [3] of $m_{J/\psi} = 3096.87 \pm 0.04\,\text{MeV}$. It is a vector meson with the quantum numbers $J^{PC} = 1^{--}$, where J is the total angular momentum, P denotes the parity and C the charge conjugation quantum numbers. The J/ψ meson decays mostly hadronically with a total width of $\Gamma = 87 \pm 5\,\text{keV}$. The decays into an electron-positron pair or a pair of two muons contribute 6% each (see table 1.1). This analysis uses the decay into two muons to identify the J/ψ, since it leaves a clean experimental signal in the detector.

decay	branching ratio
$J/\psi \rightarrow$ hadrons	$(87.7 \pm 0.5)\%$
$J/\psi \rightarrow e^+e^-$	$(5.93 \pm 0.10)\%$
$J/\psi \rightarrow \mu^+\mu^-$	$(5.88 \pm 0.10)\%$

Table 1.1: Branching ratios of J/ψ decays [3].

---

[1]There is a minimum value for $|t|$ kinematically allowed for the process $\gamma^* \rightarrow X$ which is given by $|t_{\min}| \approx (M_X^2 + Q^2)^2 m_p^2/(ys)^2$. For elastic processes the effect of $t_{\min}$ is negligible in the kinematic range analysed here.

One can distinguish between two different theoretical approaches to describe the diffractive vector meson production: on the one hand the Vector-Meson-Dominance-Model [4–7] and the Regge theory [8–11] where the interaction of the photon and the proton is described in terms of the exchange of so-called Regge-trajectories and on the other hand more recent models based on perturbative QCD [12–31] in which the interaction is modelled as an exchange of a system of at least two gluons.

1.2.1 Regge Theory and Vector-Meson-Dominance-Model

In Regge theory the total cross section for the scattering of two hadrons A and B is written as a sum over Regge trajectories

$$\sigma_{\text{tot}}^{AB}(s) = \sum_i \beta_{Ai}(0)\beta_{Bi}(0)\left(\frac{s}{s_0}\right)^{\alpha_i(0)-1}$$

where β is a form factor describing the coupling of a trajectory i to the hadrons A and B and s_0 is an arbitrary hadronic scale, often chosen to be $s_0 = 1\,\text{GeV}$. $\alpha_i(t)$ are trajectories which are parameterised as

$$\alpha_i(t) = \alpha_i(0) + \alpha_i' \cdot t = 1 + \epsilon + \alpha_i' \cdot t. \tag{1.3}$$

For typical hadron-hadron scattering two trajectories contribute to the total cross section.

$$\sigma_{\text{tot}}^{AB} = \beta_{A\mathbb{P}}(0)\beta_{B\mathbb{P}}(0)\left(\frac{s}{s_0}\right)^{\epsilon} + \beta_{A\mathbb{R}}(0)\beta_{B\mathbb{R}}(0)\left(\frac{s}{s_0}\right)^{-\eta} \tag{1.4}$$

where $\epsilon = 1 - \alpha_{\mathbb{P}}(0)$ and $\eta = 1 - \alpha_{\mathbb{R}}(0)$. The first contribution is called *Reggeon* trajectory $\alpha_{\mathbb{R}}$ and is mostly relevant at low energies. At higher energies the *Pomeron* trajectory $\alpha_{\mathbb{P}}$ dominates. A Reggeon trajectory can be related to observed particles (e.g. ρ, ω, f_2, a_2), while there are no observed particles which correspond to the Pomeron trajectory. A fit to experimental hadron-hadron data [32, 33] led to the value $\epsilon = 0.0808$ (and $\eta = 0.4525$). It is thus the contribution of the Pomeron trajectory that leads to an increase of the cross section with increasing energy s. This trajectory is often referred to as the *soft Pomeron* trajectory. Due to the fact that the proton consists of different quarks than the J/ψ meson (OZI rule [34–36]) only the Pomeron trajectory contributes to the diffractive J/ψ production. $\alpha_{\mathbb{P}}(0)$ is called the *Pomeron intercept* and $\alpha_{\mathbb{P}}'$ the *Pomeron slope*. In Regge theory the slope parameter $\alpha_{\mathbb{P}}'$ is universal. At high energies the elastic differential cross section at low values of t can be written as

$$\frac{d\sigma_{\text{el}}^{AB}}{dt} = \frac{1}{16\pi}\beta_{A\mathbb{P}}^2(t)\beta_{B\mathbb{P}}^2(t)\left(\frac{s}{s_0}\right)^{2\alpha_{\mathbb{P}}(t)-2}.$$

With an exponential ansatz for the form factors $\beta_{i\mathbb{P}}$

$$\beta_{i\mathbb{P}}(t) = \beta_{i\mathbb{P}}(0) \cdot e^{b_i t}$$

one obtains

$$\frac{d\sigma_{\text{el}}^{AB}}{dt} = \frac{1}{16\pi}\beta_{A\mathbb{P}}^2(0)\beta_{B\mathbb{P}}^2(0)e^{b_{\text{el}}t}\left(\frac{s}{s_0}\right)^{2\alpha_{\mathbb{P}}(0)-2} \tag{1.5}$$

with

$$b_{\mathrm{el}}(s) = 2b_{0;A} + 2b_{0;B} + 2\alpha'_{\mathbb{P}} \ln \frac{s}{s_0} \qquad (1.6)$$

where $b_{0;A}$ and $b_{0;B}$ are energy independent terms originating from the form factors. A fit to experimental proton-proton scattering results gave $b_{0;p} \approx 2 - 3\,\mathrm{GeV}^{-2}$. An increase of $b(s)$ with increasing energy s has been observed. This effect is called *shrinkage*. In a geometrical interpretation the slope parameter [27,37,38] $b(s)$ is related to the mean-square of the interaction radius $r^2 = 2b(s)$. At proton-proton experiments $b(s)$ varies between $b \approx 8\,\mathrm{GeV}^{-2}$ at small energies (corresponding to the proton radius $r \approx 4\,\mathrm{GeV}^{-1}$) and $b \approx 12\,\mathrm{GeV}^{-2}$ at $s \approx 5000\,\mathrm{GeV}^2$. In this geometrical picture the scattering constituents are regarded as discs oriented transverse to the direction of flight of the beams. According to equation (1.6) the radius of the interaction region consists of two parts: firstly two energy independent terms, which are related to the projectiles A and B respectively, and an energy dependent term increasing with s. The second term grows with $\alpha'_{\mathbb{P}}$. A comparison to data of hadron-hadron scattering experiments [32,33] has given a value of $\alpha'_{\mathbb{P}} \approx 0.25\,\mathrm{GeV}^{-2}$.
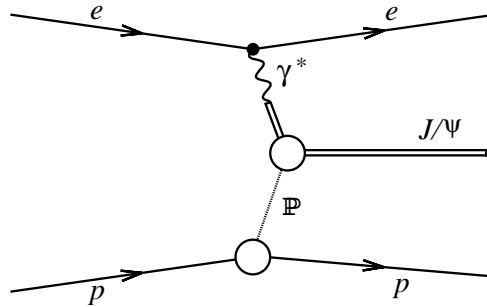
Figure 1.3: Schematic Feynman diagram of the elastic J/ψ production process.

With the help of the Vector-Meson-Dominance-Model (VMD) Regge theory can also be applied to diffractive photon-proton scattering processes (figure 1.3). In the VMD model the photon is a superposition of an electromagnetic part $|\gamma_{\mathrm{QED}}\rangle$ and a hadronic part $|h\rangle$

$$|\gamma\rangle = N_1 |\gamma_{\mathrm{QED}}\rangle + N_2 |h\rangle . \qquad (1.7)$$

The hadronic state must have the same quantum numbers as the photon which is the case for neutral vector mesons. Therefore equation (1.7) can be written as

$$|\gamma\rangle = N_1 |\gamma_{\mathrm{QED}}\rangle + \sum_V \frac{e}{f_V} |V\rangle$$

where f_V denotes the coupling of the vector meson V to the photon and corresponds to the probability that the photon fluctuates into a virtual vector meson V^*. The cross section for photoproduction of a vector meson V is then:

$$\sigma(\gamma^* p \to V p) = \frac{4\pi\alpha_{\mathrm{QED}}}{f_V^2} \sigma(V p \to V p)$$

In this approximation, processes of the form $\gamma^* p \to V^* p \to V' p$ are neglected, where V' denotes a different type of vector meson than V. The corresponding relations to equations (1.5) and (1.6) for photon-proton scattering with the VMD approach are

$$\frac{d\sigma_{\gamma p}}{dt} = \frac{d\sigma_{\gamma p}}{dt}\Big|_{t=0, W=W_0} \cdot e^{b(W)t} \left(\frac{W}{W_0}\right)^{4(\alpha_{\mathbb{P}}(0)-1)} \tag{1.8}$$

$$b(W) = b_0 + 2\alpha'_{\mathbb{P}} \ln \frac{W^2}{W_0^2}$$

At low t the W dependence can be simplified to

$$\sigma_{\gamma p} \propto \left(\frac{W}{W_0}\right)^{4(\alpha_{\mathbb{P}}(0)-1)} = \left(\frac{W}{W_0}\right)^{\delta}. \tag{1.9}$$

The ep cross section is to first order related to the γp cross section via

$$\sigma(\gamma p \to J/\psi Y) = \sigma(ep \to e J/\psi Y)/\Phi_\gamma \tag{1.10}$$

where Φ_γ is the photon flux integrated over Q^2 and y (see section 4.1). This approximation is valid to good accuracy, since the photon flux decreases rapidly with Q^2 and y. In addition it is assumed that the virtual vector meson has the same helicity as the photon and it is conserved during the interaction with the proton (see section 1.3).

Figure 1.4 shows the elastic cross sections for different vector meson production processes and the total photoproduction cross section measured at HERA as a function of the centre-of-mass energy W [39–51]. The total γp cross section as well as the cross sections for elastic production of light vector mesons show a slow rise which can be described by a fit $W^\delta = W^{4(\alpha_{\mathbb{P}}(t)-1)}$ with $\delta \approx 0.22$. The photoproduction cross section of the J/ψ meson, however, yields a value of $\delta \approx 0.7$. The electroproduction $Q^2 \gtrsim 2\,\text{GeV}^2$ of the lighter ρ meson, not shown here, shows a similar steep rise [52,53].

In order to describe the steeper rise with energy, new models have been developed. In [55] an additional hard Pomeron is proposed with a trajectory $\alpha_{\mathbb{P}_h}$

$$\alpha_{\mathbb{P}_h}(t) \approx 1.4 + 0.1 \cdot t.$$

The combination of a soft and a hard Pomeron is able to describe the J/ψ photoproduction qualitatively [42]. The calculations in [56] are based on a dipole Pomeron model assuming a trajectory with a non-linear t-dependence.

For the proton dissociative process at fixed masses M_Y of the hadronic final state the same W dependence as for the elastic process is predicted, while the t dependence is different. The cross section for the diffractive scattering process $AB \to YB$, where the hadron A dissociates into the system Y is given by [38,57,58]

$$\frac{d^2\sigma_{\text{pd}}^{AB}}{dt\,dM_Y^2} \propto \frac{\beta_A(0)\beta_B^2(t)}{s^2} s^{2\epsilon} \left(\frac{s}{M_Y^2}\right)^{2\alpha_{\mathbb{P}}(t)} \left(M_Y^2\right)^{2\alpha_{\mathbb{P}}(0)} = x\beta_A(0)\beta_B^2(0)s^{2\epsilon} \frac{e^{b_{\text{pd}}t}}{M_Y^{2(1+\epsilon)}}. \tag{1.11}$$

M_Y denotes the mass of the hadronic final state. ϵ is as defined in equation (1.3) and b_{pd} is the slope parameter

$$b_{\text{pd}} = 2b_{0;B} + 2\alpha'_{\mathbb{P}} \ln \frac{s}{M_Y^2}.$$

Measurements at HERA [43] yield b_{pd} of the order of $1\,\text{GeV}^{-2}$, while the W dependence of the cross section is similar to the elastic process.
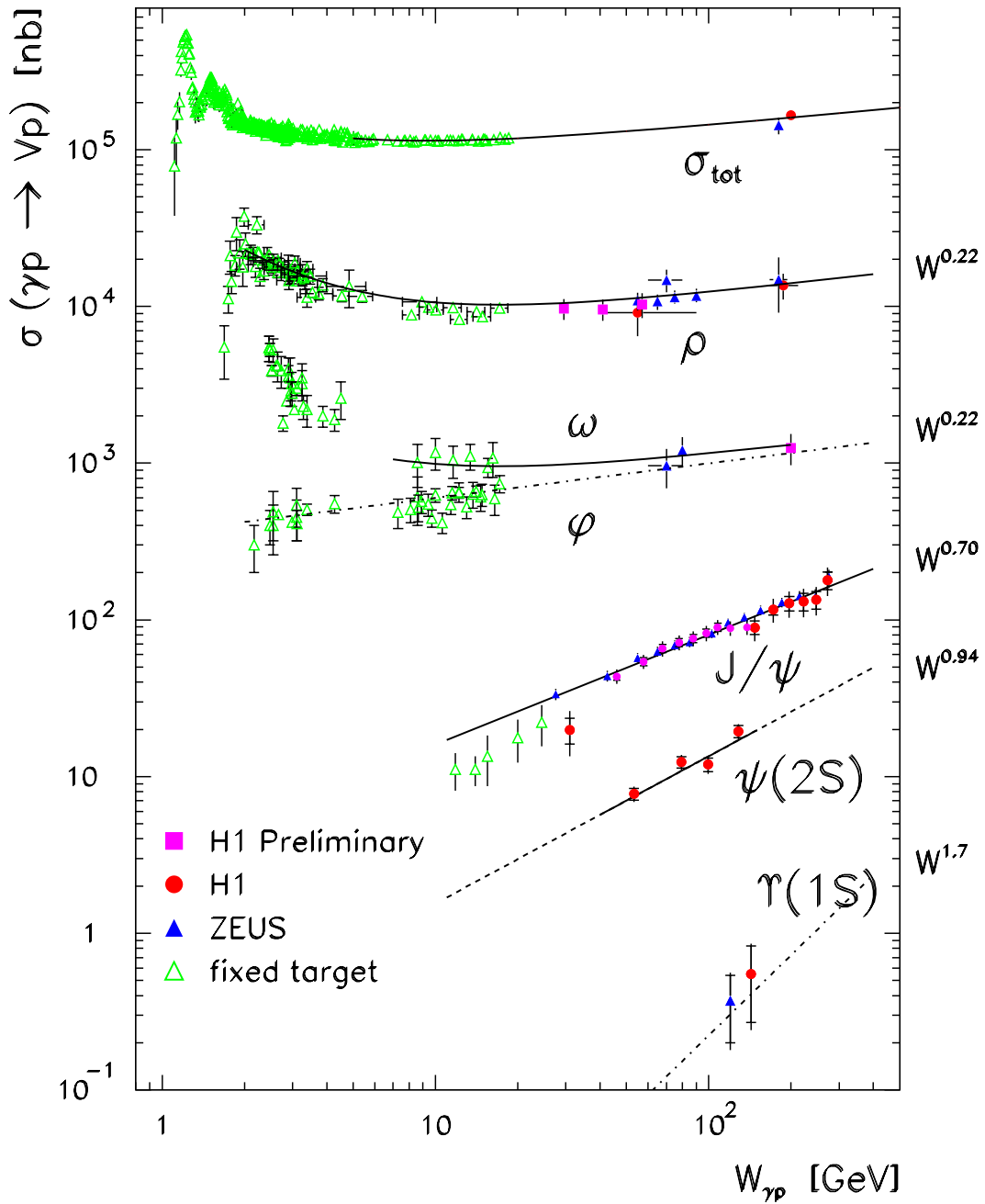
Figure 1.4: Measurements of the total γp cross section and the cross section for elastic vector meson production as a function of W [39–51]. The curves are fits of equation (1.4) to the data. For the heavy vector mesons equation (1.9) is used instead. At the right hand side of the plot the extracted values for δ are shown. Note that for Υ production $\delta \approx 1.7$ is a prediction [54] and not derived from a fit.

1.2.2 QCD based Models

Quantum Chromodynamics (QCD), the theory of the strong force, has been proven to successfully describe a huge amount of data in many different experiments. In a similar way in which Quantum Electrodynamics (QED) describes the interaction between electrons and photons, QCD characterises the interaction of quarks and gluons.

At short distances (smaller than the proton radius) perturbative calculations can be applied. At large distances perturbative calculations in QCD are not possible, since the running coupling is large and the perturbative expansion breaks down. In scattering processes not only short distance effects but also forces at larger distances, of the order of the proton radius, are important.

HERA cannot only test QCD predictions at small distances, but also spans the transition region to larger distances. As mentioned above, *ep*-collisions can be treated as photon-proton scattering processes. At high energies the extension of the emitted virtual photon in the transverse direction can be very small. This leads to the advantage of being able to probe the proton at small distances. On the other hand at low values of the photon virtuality the photon can have a larger transverse extension.

In QCD the factorisation [24–26] of the J/ψ production process into three steps plays an important role. The photon fluctuates into a quark-antiquark pair long before the interaction. In a second step the $q\bar{q}$-pair interacts with the proton. Finally the $q\bar{q}$-pair forms a bound state, a vector meson, a long time after the interaction with the proton.
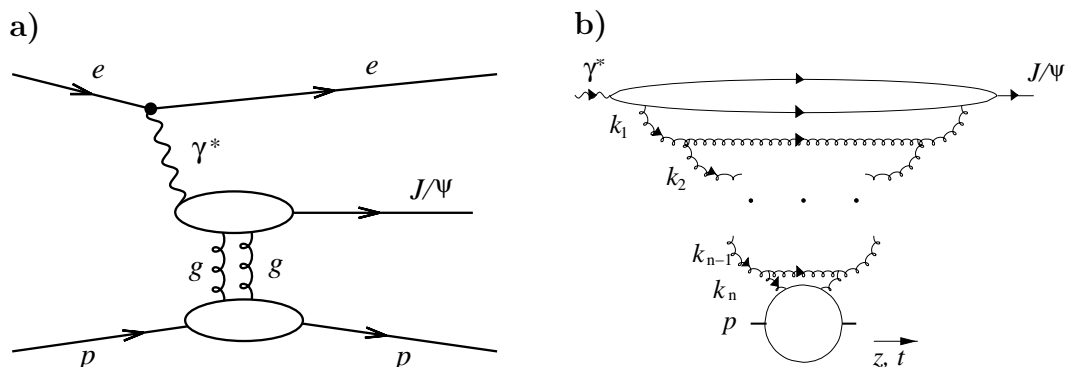
Figure 1.5: a) Feynman diagram of elastic J/ψ production in the QCD framework.
b) Space-time diagram of the elastic J/ψ production in the proton rest frame.

For historical reasons the gluon system exchanged between the photon and the proton is also in QCD referred to as Pomeron. To stress the difference to a real particle it is called *effective* Pomeron trajectory.

The simplest assumption for the diffractive interaction of the photon and the proton is an exchange of a colourless two-gluon system [59, 60]. Figure 1.5 a) shows the lowest order diagram for the elastic process. In the presence of a hard scale, which may be given by a high photon virtuality Q^2 or the mass of a heavy quark m_q, the transverse extension of the photon is small and the interaction can be calculated in perturbative QCD. In [12, 14]

the process is calculated in the leading logarithmic approximation (LLA) taking terms of the order of $\alpha_s \ln(Q^2_{\text{eff}}/\Lambda^2_{\text{QCD}})$ into account, where Λ_{QCD} is the QCD scale and the effective hard scale Q^2_{eff} is given by

$$Q^2_{\text{eff}} = \frac{Q^2 + M^2_\psi}{4}.$$

The differential cross section is calculated as:

$$\left.\frac{d\sigma_{\gamma p}}{dt}\right|_{t=0} = \frac{\Gamma_{ee} M^3_\psi \pi^3}{48\alpha} \frac{\alpha_s(Q^2_{\text{eff}})^2}{Q^8_{\text{eff}}} \left(xg(x, Q^2_{\text{eff}})\right)^2 \left(1 + \frac{Q^2}{M^2_\psi}\right) \qquad (1.12)$$

where

$$x = \frac{4Q^2_{\text{eff}}}{W^2}.$$

Γ_{ee} is the width of the decay $J/\psi \to e^+e^-$. $g(x, Q^2_{\text{eff}})$ is the gluon density. Since $g(x, Q^2_{\text{eff}})$ rises steeply with decreasing x equivalent to increasing W and $\sigma_{\gamma p} \propto \left(xg(x, Q^2_{\text{eff}})\right)^2$ equation (1.12) yields a steep rise of the differential cross section as a function of W, which is in agreement with experimental data [42, 51]. In [12] no prediction for the t dependence of the cross section is made.

The two terms in the last parenthesis in equation (1.12) correspond to the production with transversely and longitudinally polarised photons, respectively. In [31] the two contributions are modified by different factors taking Fermi motion corrections into account.

In [12] it is assumed that the two gluons carry half of the photon momentum each, which is only valid for small values of x. In [19–21] off-diagonal or skewed parton distributions $(x \neq x')$ have been taken into account leading to

$$\sigma_{\gamma p} \propto \left(x'g(x, x', Q^2_{\text{eff}})\right)^2$$

where

$$x = \frac{M^2_{q\bar{q}} + Q^2}{W^2} \qquad \text{and} \qquad x' = \frac{M^2_{q\bar{q}} - M^2_\psi}{W^2} \ll x.$$

In [20] parton-hadron duality is assumed and a prediction for the slope parameter b as a function of Q^2 is given:

$$b(Q^2) = \frac{4}{\langle -t\rangle + 0.71\,\text{GeV}^2} + \frac{2}{Q^2 + M^2_{q\bar{q}} + \langle -t\rangle} + 2\alpha' \ln\left(\frac{W^2 M^2_{q\bar{q}}}{(Q^2 + M^2_{q\bar{q}})^2}\right)$$

Similar calculations have been done in [13, 17, 61] leading to similar W and Q^2 dependence of the cross section as in equation (1.12) in the range considered here.

The t-dependence of the cross section is discussed in [23]. Here the two-gluon form factor is assumed to be

$$\Gamma(t) = \left(1 - t/m^2_{2g}\right)^{-2}$$

with $m^2_{2g} \approx 1\,\text{GeV}^2$. It is argued that the t-dependence does not exactly match an exponential form as in equation (1.8) but is rather given by:

$$\frac{d\sigma}{dt} \propto \Gamma^2(t) = \frac{1}{(1 - t/m^2_{2g})^4}.$$

A different approach to describe the γp interaction is the colour dipole model [28–30], which also uses the factorisation assumption:

$$A_{\gamma^* p \to J/\psi p} \propto \psi(\gamma^* \to q\bar{q}) \cdot \sigma_{q\bar{q}p} \cdot \psi(q\bar{q} \to J/\psi)$$

$A_{\gamma^* p \to J/\psi p}$ is the amplitude of the process and $\psi(\gamma^* \to q\bar{q})$ and $\psi(q\bar{q} \to J/\psi)$ are two wave functions. Here the $q\bar{q}$-pair is seen as a colour dipole. An advantage of the colour dipole model is that it does not necessarily require a hard scale. The dipole cross section $\sigma_{q\bar{q}p}$ includes soft processes and depends on $\hat{b}$, which is the transverse size of the $q\bar{q}$-pair.

In [18, 22] the dipole cross section is given as

$$\sigma_{q\bar{q}p}(\hat{b}^2, x) = \frac{\pi^2}{3}\hat{b}^2 \alpha_s(\bar{Q}^2) xg(x', \bar{Q}^2)$$

where $\hat{b} < \hat{b}_{Q_0} \approx 0.4\,\text{fm}$ is required. x' and $\bar{Q}^2$ are defined by

$$
\begin{aligned}
x' &= x'_{\min}\left(1 + 0.75\frac{\langle\hat{b}\rangle^2}{\hat{b}^2}\right) \\
\bar{Q}^2 &= \frac{\lambda}{\hat{b}^2}
\end{aligned}
$$

where

$$
\begin{aligned}
x'_{\min} &= x\left(1 + \frac{4m_c^2}{Q^2}\right) \\
\langle\hat{b}\rangle^2 &= \frac{\lambda}{Q^2 + 4m_c^2}.
\end{aligned}
$$

$m_c \approx 1.5\,\text{GeV}$ denotes the mass of the charm quark. The parameter λ is introduced to determine the dividing line between perturbative and non-perturbative physics. The energy dependence of the effective trajectory $\alpha'_{\mathbb{P}}$ is modelled by the simple relation

$$\alpha'_{\mathbb{P}}(b) = 0.5\frac{\hat{b}^2}{\hat{b}^2 + \hat{b}_\pi^2}\,\text{GeV}^{-2}.$$

It is designed to give $\alpha'_{\mathbb{P}}(\hat{b} = \hat{b}_\pi \approx 0.65\,\text{fm}) = \alpha'_{\mathbb{P}}(soft) = 0.25\,\text{GeV}^{-2}$ and to tend to zero quadratically at small $\hat{b}$.

The J/ψ production can be interpreted in a radiation picture [27]. The interaction of the photon and the proton at higher orders is sketched in figure 1.5 b). It shows a time-ordered cascade-like emission of gluons from the $q\bar{q}$-pair, where the momenta of the gluons decrease. The first gluon with momentum k_1 has a small transverse size. The subsequently following gluons carry smaller momenta and increase in the transverse direction. This intuitive picture of the perturbative process breaks down when the momentum of the last gluon gets too small. Here non-perturbative forces come into play, as symbolised by the circle in the diagram.

After the interaction with the proton all emitted gluons are recollected and the $q\bar{q}$-pair forms the J/ψ vector meson. It is this cloud of gluons that leads to the steep rise of the cross section with energy as seen in equation (1.12). The rise also depends on the transverse size of the $q\bar{q}$-pair. The transverse size of the vector meson depends on the quark mass $r_V \sim 1/m_q$, where m_q denotes the mass of the quark. Due to the heavy mass of the charm quark the $c\bar{c}$-pair producing a J/ψ has a smaller transverse extension than for example the ρ meson consisting of the light u and d quarks and gluons.

In the case of J/ψ production the perturbative process of the gluon emission dominates over the non-perturbative interaction of the last gluon with the proton even at low photon virtualities Q^2. In the case of ρ photoproduction the soft process is dominant and perturbative QCD is not applicable. At higher values of the photon virtuality, where Q^2 provides a hard scale, the rise of the ρ production cross section with W has been measured to approach the value of J/ψ photoproduction [52].

Also the t-dependence of the cross section as described in equation (1.8) by the impact parameter b can be explained in this picture. As mentioned above the t-dependence is related to transverse size of the scattering system. For ρ photoproduction b values of the order of $10\,\mathrm{GeV}^{-2}$ have been measured, while for larger values of Q^2_{eff} b is measured to be of the order $4 - 5\,\mathrm{GeV}^{-2}$. This again suggests that the transverse size of the interaction region in the case of hard processes is given by the proton radius. At large values of Q^2_{eff} perturbative QCD leads to the expectation that $\alpha'_{\mathbb{P}}$ should be smaller than for the soft Pomeron [27].

1.3 Helicity Structure of J/ψ Production

The assumption that the virtual vector meson has the same helicity as the photon and that it is also conserved during the interaction with the proton is referred to as s-channel helicity conservation (SCHC). The γ^*p cross section is given by a superposition of the transverse and longitudinal cross sections

$$\sigma_{\gamma^*p} = \sigma^T_{\gamma^*p} + \varepsilon \sigma^L_{\gamma^*p} \tag{1.13}$$

where ε describes the ratio of the longitudinally and transversely polarised photon flux and is defined as

$$\varepsilon = \frac{1-y}{1-y+\frac{1}{2}y^2}. \tag{1.14}$$

In the kinematic range of this analysis $\varepsilon \gtrsim 0.95$ with $\langle \varepsilon \rangle = 0.993$.

Real photons do not have a longitudinal contribution. In the photoproduction limit $Q^2 \to 0$ of ep-collisions quasi-real photons are produced and under SCHC no contributions from longitudinally polarised J/ψ mesons are expected. A different Q^2 dependence of the cross section for longitudinally and transversely polarised J/ψ mesons is predicted in [6,62].

$$R = \frac{\sigma^L_{\gamma^*p}}{\sigma^T_{\gamma^*p}} = \xi \frac{Q^2}{M^2_\psi} \tag{1.15}$$

where M_ψ is the mass of the vector meson. ξ is a phenomenological parameter of order 1.

The polarisation of the J/ψ meson is related to the angular distributions of the decay leptons. The distributions can be completely described by 15 spin-density matrix elements [63]. In this context a set of three angles (see figure 1.6) is often introduced [64–68].
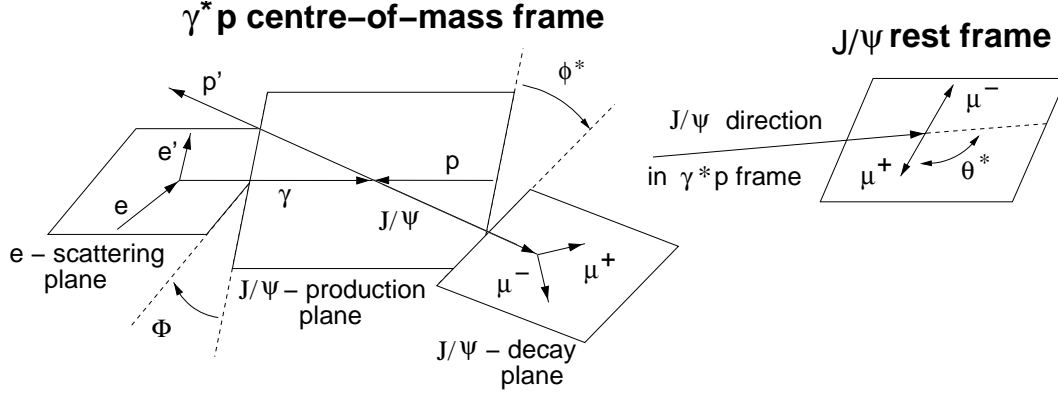
Figure 1.6: Illustration of the angles in the production and decay of J/ψ mesons.

All three angles are measured in the helicity frame, in which the J/ψ direction of flight defines the z-axis in the γ^*p centre-of-mass frame. θ^* is the polar angle of the beam-sign daughter muon in the J/ψ rest frame, with $\theta^* = 0°$ taken as the flight direction of the J/ψ in the γ^*p centre-of-mass frame. ϕ^* is the angle between the J/ψ production plane and the decay plane in the γ^*p centre-of-mass frame. Φ is the angle between the scattering plane of the beam lepton and the J/ψ production plane. Often $\Psi = \phi^* - \Phi$ is used instead of Φ. The angles can be expressed in terms of the momentum vectors of the particles [64]:

$$\cos\theta^* = \frac{\vec{P}_\psi \cdot \vec{p}_{\mu^*}}{|\vec{p}_{\mu^*}||\vec{P}_\psi|}$$

$$\cos\phi^* = \frac{(\vec{q} \times \vec{P}_\psi) \cdot (\vec{P}_\psi \times \vec{p}_\mu)}{|\vec{q} \times \vec{P}_\psi||\vec{P}_\psi \times \vec{p}_\mu|}$$

$$\sin\phi^* = \frac{-[(\vec{q} \times \vec{P}_\psi) \times \vec{P}_\psi] \cdot (\vec{P}_\psi \times \vec{p}_\mu)}{|(\vec{q} \times \vec{P}_\psi) \times \vec{P}_\psi||\vec{P}_\psi \times \vec{p}_\mu|}$$

$$\cos\Phi = \frac{(\vec{q} \times \vec{P}_\psi) \cdot (\vec{k} \times \vec{k'})}{|\vec{q} \times \vec{P}_\psi| \cdot |\vec{k} \times \vec{k'}|}$$

$$\sin\Phi = \frac{(\vec{q} \times \vec{P}_\psi) \times (\vec{k} \times \vec{k'}) \cdot \vec{q}}{|\vec{q} \times \vec{P}_\psi| \cdot |\vec{k} \times \vec{k'}|}$$

where $\vec{q}$ is taken to be equal to $-\vec{P}$ (all vectors have been introduced in section 1.1). $\vec{p}_{\mu^*}$ denotes the momentum vector of the muon in the J/ψ rest frame.

For the θ^* dependence of the cross section one obtains

$$\frac{d\sigma}{d\cos\theta^*} \propto 1 + r_{00}^{04} + \left(1 - 3r_{00}^{04}\right)\cos^2\theta^* \tag{1.16}$$

where r_{00}^{04} is one of the spin-density matrix elements, describing the probability to produce longitudinally polarised J/ψ mesons. In the case of SCHC it is related to equation (1.15) by

$$R = \frac{1}{\varepsilon} \frac{r_{00}^{04}}{1 - r_{00}^{04}}.$$

Under the assumption of SCHC one expects to find $r_{00}^{04} = 0$ in the regime of photoproduction where $R \to 0$, thus reducing equation (1.16) to

$$\frac{d\sigma}{d\cos\theta^*} \propto 1 + \cos^2\theta^*.$$

For the ϕ^* dependence of the cross section one obtains

$$\frac{d\sigma}{d\phi^*} \propto 1 + r_{1-1}^{04} \cos(2\phi^*)$$

giving access to another spin-density matrix element. For SCHC $r_{1-1}^{04} = 0$ is expected. A third matrix element r_{1-1}^1 describes the Ψ dependence of the cross section

$$\frac{d\sigma}{d\Psi} \propto 1 - \varepsilon r_{1-1}^1 + \cos(2\Psi).$$

In the case of SCHC and natural parity exchange (NPE) the spin-density matrix elements r_{00}^{04} and r_{1-1}^1 are related by

$$r_{1-1}^1 = \frac{1}{2}(1 - r_{00}^{04}).$$

1.4 Monte Carlo Simulations

Monte Carlo simulations are used to determine the geometrical acceptance and detector efficiencies.

The first step in the simulation is the event generator. Based on a physics model the generator calculates the four-vectors of the particles in the analysed process. This information is then given to the detector simulation [69, 70], which calculates the detector response. Afterwards the simulated events are run through the same reconstruction software as the experimental data. In this analysis two different event generators are used. The first one, DIFFVM [71], is used to generate $J/\psi \to \mu^+\mu^-$ events. A second generator LPAIR [72] is used to simulate non-resonant lepton pair production, which contributes to the background.

The event generator DIFFVM is based on the Vector-Meson-Dominance-Model and Regge theory.

$$\sigma_{ep}(Q^2, W, t) \propto \left(\frac{W}{W_0}\right)^{4\epsilon} \left(1 + \frac{Q^2}{M_\psi^2}\right)^{-n} e^{b_{el}t}$$

The M_Y dependence of the proton dissociative J/ψ production is modelled according to equation (1.11). It is used to simulate diffractive vector meson production processes.

Due to a large number of free parameters it can be tuned to describe the data. In this analysis four different sets of generated events are used. In both kinematic regions, photoproduction and deep inelastic scattering, a set of elastic events is generated as well as one with proton dissociation.

In the original version of DIFFVM the helicity structure of the J/ψ production is not described consistently. The decay angular distribution for $\cos\theta^*$ is implemented, while a flat distribution for Ψ is implemented for the whole Q^2 range. For the present analysis the Ψ dependence is also implemented according to [67] assuming SCHC. The distribution is implemented as

$$\mathcal{W}(\theta^*, \Psi) = \frac{3}{16\pi}\left(1 + \cos^2\theta^* + \varepsilon\sin^2\theta^*\left(2R - \cos 2\Psi\right) + \sqrt{2\varepsilon R\left(1+\varepsilon\right)}\cos\varrho\cos\Psi\sin 2\theta^*\right)$$

where ϱ is a phase describing the interference between the amplitudes for J/ψ production by longitudinally and transversely polarised photons. In the present analysis $\cos\varrho = 0.9$ is used. The effect of the change in the angular distribution is displayed in figure 1.7 a) for $Q^2 > 2\,\mathrm{GeV}^2$.

In the region of deep inelastic scattering radiative corrections are important. In the case of the DIS MC simulation radiative corrections are added using the generator HERACLES [73, 74]. Diagrams up to order α^3 are taken into account.

For the calculation of the Born cross section in section 4.1 the radiative corrections are taken into account using the relation

$$\sigma^{\mathrm{Born}} = \sigma^{\mathrm{measured}}C_{\mathrm{rad.corr.}}.$$

The correction $C_{\mathrm{rad.corr.}}$ is estimated in each analysis bin using two different MC simulations. The first includes generated $J/\psi \to \mu^+\mu^-$ events without radiative corrections. The second one takes radiative corrections into account. Figure 1.7 shows the W, t and Q^2 dependence of these corrections.

$$C_{\mathrm{rad.corr.}} = \frac{\text{number of generated events without radiative corrections}}{\text{number of generated events including radiative corrections}}$$

Integrated over the range in Q^2, W and t analysed here a total correction factor of $C_{\mathrm{rad.corr.}} = 0.96$ is found. Similar studies of the corrections, which yield compatible results, can be found in [74–76].

The ratio of the cross section for longitudinally and transversely polarised photons is parameterised as

$$R(Q^2) = \frac{\sigma^L_{\gamma^* p}}{\sigma^T_{\gamma^* p}} = \frac{\xi\frac{Q^2}{\Lambda^2}}{1 + \chi\xi\frac{Q^2}{\Lambda^2}}$$

where χ is a free parameter motivated by phenomenology. For $\chi = 0$, $\xi = 1$ and $\Lambda = m_{J/\psi}$ it reproduces equation (1.15).

The relevant parameters used for the generation of diffractive J/ψ events in this analysis are given in table 1.2.

In the diffractive $J/\psi \to \mu^+\mu^-$ data sample the non-resonant lepton pair production is the most dominant contribution to the background. LPAIR generates events of the Bethe-Heitler process. In [77] it has been shown that this is the dominant process in the analysed kinematic region.
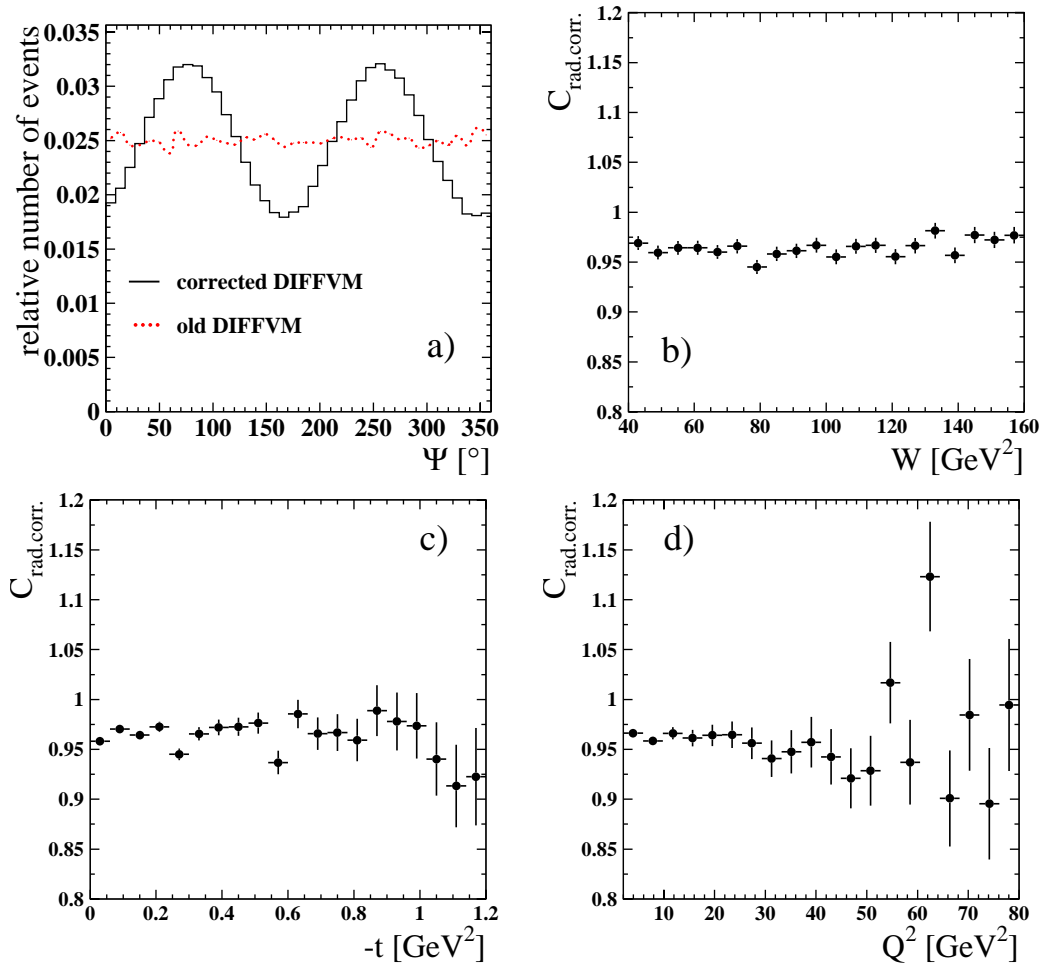
Figure 1.7: Figure a) shows the difference between the original DIFFVM MC generator using a flat Ψ distribution and a corrected version using a distribution according to [67], i.e. assuming SCHC. Figures b)-c) show the radiative correction $C_{\text{rad.corr.}}$ as a function of W, $-t$ and Q^2. For the final results the correction factor is derived for each analysis bin separately.

	Λ	$\cos \varrho$	ξ	χ	ϵ	$\alpha'_{\mathbb{P}}$	b_{el}	b_{pd}
PhP	$m_{J/\psi}$	0.9	1.0	0.0	0.225	0.0	4.8	1.6
DIS	$m_{J/\psi}$	0.9	0.3	0.3	0.225	0.0	4.8	1.6

Table 1.2: Parameter settings used to generate diffractive J/ψ events in photoproduction (PhP) and deep inelastic scattering (DIS).

2 The Experiment

The data used in this analysis were collected at the HERA collider during the years 1999 and 2000 by the H1 detector.

This chapter gives a brief description of the collider and the H1 detector components relevant to this analysis. A detailed description of the detector components can be found in a number of previous analyses [75–81] and a complete description of the H1 detector in [82, 83].

2.1 HERA
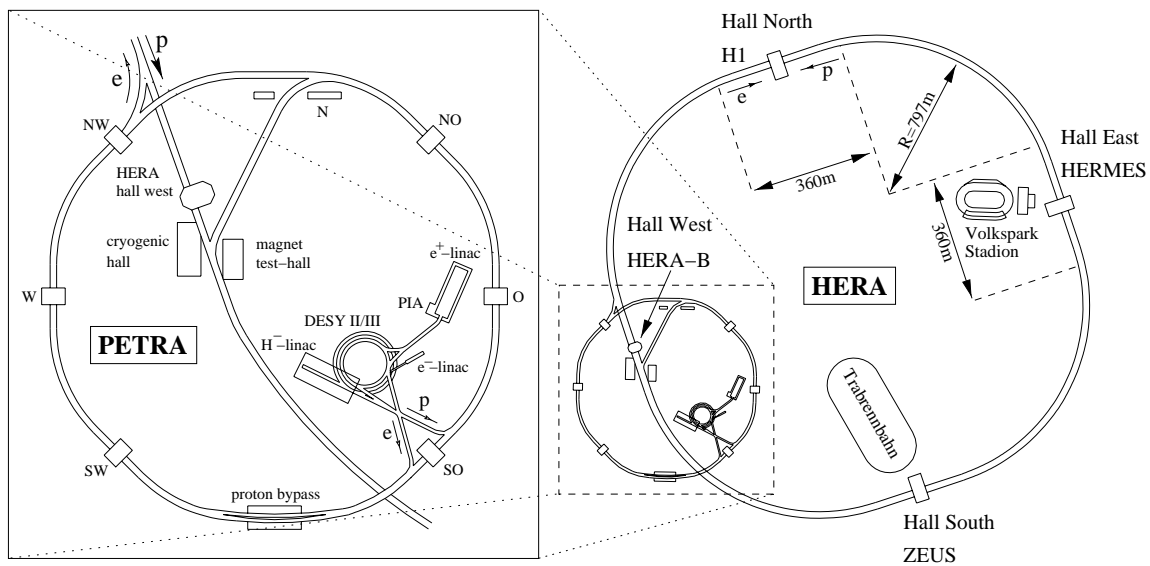
Figure 2.1: The HERA collider with its pre-accelerators and the detectors.

The **H**adron-**E**lectron-**R**ing-**A**ccelerator HERA (figure 2.1) started operating in 1992. Here positrons[1] and protons are accelerated in two separate rings to energies of $27.5\,\mathrm{GeV}$ and $920\,\mathrm{GeV}$, respectively, leading to a centre-of-mass energy of $\sqrt{s} = 318\,\mathrm{GeV}$. The storage rings measure $6.4\,\mathrm{km}$ in circumference. At two opposite points the beams are brought

---

[1]HERA can be operated with both electrons or positrons. During the data taking period for this analysis, only in the first part of the year 1999 electrons were used. Therefore the term 'positrons' will be used throughout this thesis, also for electrons.

to collisions. Here the multi-purpose detectors H1 and ZEUS measure the products of the collisions. There are two additional experiments, HERA-B and HERMES, which use just one of the beams.

The positrons and protons are packed into bunches. There are up to 200 bunches in each storage ring, leading to a time separation of 96 ns between two collisions. This time interval is used as a measure at HERA and its experiments. To analyse the beam background pilot-bunches are used. These are bunches of only positrons or protons without collision partners. Possible sources of beam background are beam-gas- or beam-beampipe-interactions. Some bunches are out of phase, being early or too late. Such bunches are called satellite bunches and are also a cause of background, due to the fact that the interaction point differs from the nominal vertex.

2.2 The H1 Detector
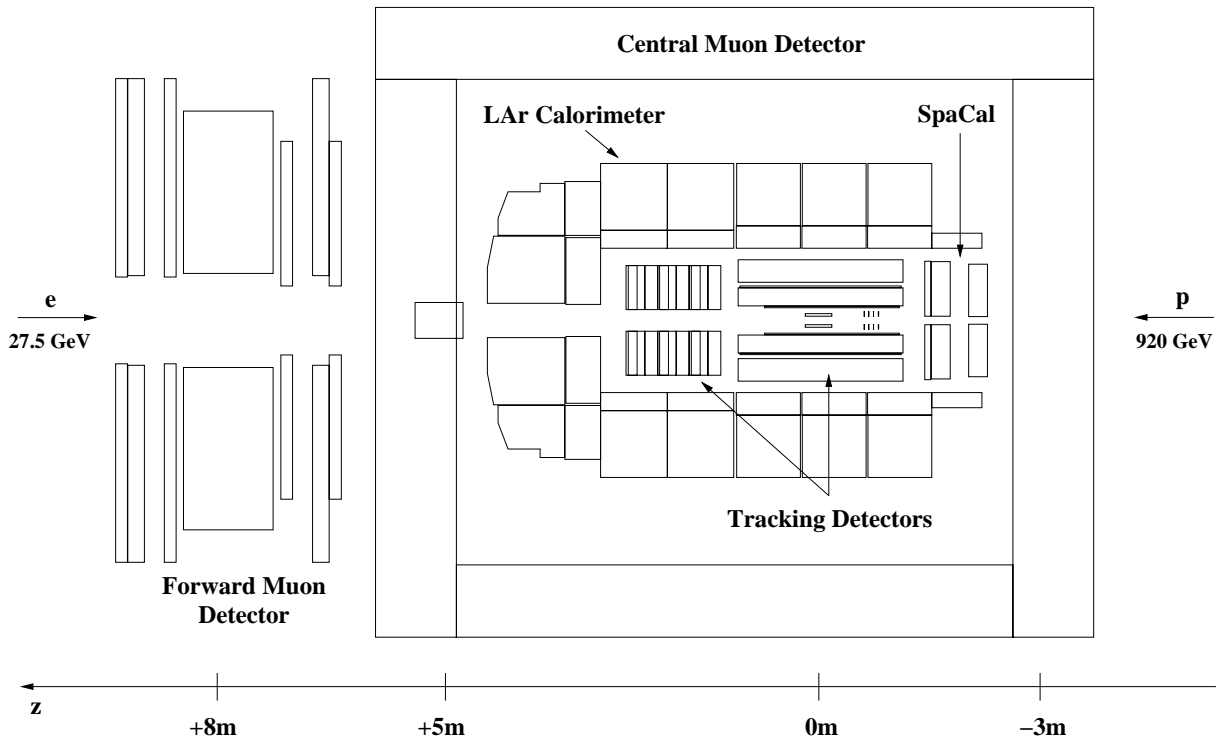
Figure 2.2: Schematic side-view of the H1 detector.

The H1 detector (figure 2.2) is located in hall north of the HERA collider. It is a multi-purpose experiment with different instrumentation in proton and positron direction taking into account the asymmetric beam-particle types and energies.

The co-ordinate system used at the H1 detector has its origin at the nominal interaction point. The z-axis lies along the flight direction of the outgoing protons, which is also referred to as the *forward* direction. The x-axis points toward the centre of the HERA ring, whereas the y-axis points upwards. In many cases co-ordinates are given in terms

of the radial length r and the two angles θ and ϕ. The polar angle θ is measured with respect to the positive z-axis and the azimuthal angle ϕ with respect to the x-axis in the xy-plane.

The detector consists of several components located in different layers around the beampipe. Closest to the beampipe is a tracking system surrounded by a Calorimeter. Next a superconducting coil follows, which provides a homogeneous magnetic field of 1.15 T. The iron return yoke of the coil is instrumented and used as a muon detector. The detector covers almost the full 4π angle in space and has good spatial and momentum resolution. Therefore a good energy measurement and identification of all particles induced by the ep-interaction is possible. In the following sections the relevant parts for this analysis are briefly described.

2.2.1 Tracking System

The tracking system reconstructs tracks of charged particles by measuring their momentum and angle as well as the specific energy loss from ionisation dE/dx. The energy loss can be used to identify isolated tracks, but also jets with high track multiplicity can be reconstructed. The tracking system is divided into two parts, the forward and the central tracking detectors. This analysis uses mainly the Central Tracking Detector, which provides a better momentum resolution. It consists of seven chambers; starting at the beampipe these are the Central Silicon Tracker, the Central Inner Proportional Chamber, the Central Inner z-Drift Chamber and the inner Central Jet Chamber (CJC1) followed by the Central Outer z-Drift Chamber, the Central Outer Proportional Chamber and the outer Central Jet Chamber (CJC2).

The Central Tracking Detector covers polar angles in the range $15° \lesssim \theta \lesssim 165°$. The Proportional Chambers are are used for triggering. The z-Drift Chambers allow a z resolution of $170\mu m$. The Central Jet Chamber consists of 30 (CJC1) and 60 (CJC2) cells, which are shifted by $30°$ compared to the radial direction. This guaranties that each track has to cross at least one cell, allowing a good time resolution (less than 1 ns), which is used to reject muons from cosmic rays.

2.2.2 Calorimeters

There are two main calorimeters in the H1 detector. The Liquid Argon Calorimeter (LAr) [84–87] in the central and forward region and the SpaCal [88] in the backward direction.

The Liquid Argon Calorimeter covers the polar angular range of $4° \lesssim \theta \lesssim 153°$. It is used to detect the scattered positron at high photon virtualities of $Q^2 > 100\,\text{GeV}^2$ or particles belonging to the hadronic final state. Electrons can be identified and their energy be measured. Muons can be identified as minimum ionising particles. The Liquid Argon Calorimeter has a depth of $5 - 8$ hadronic interaction lengths. The inner electromagnetic part of the Calorimeter has an energy resolution of $\sigma_E/E \approx 0.12/\sqrt{E[\,\text{GeV}]} \oplus 0.01$, while the hadronic part has a resolution of $\sigma_E/E \approx 0.50/\sqrt{E[\,\text{GeV}]} \oplus 0.02$ [85]. In this analysis

it is used to identify the decay muons of the J/ψ meson. The identification efficiency is described in section 4.6.1. In addition the forward part of the Liquid Argon Calorimeter is used to distinguish between elastic and proton dissociative events.

The SpaCal is a 'spaghetti' type electromagnetic lead scintillating-fibre calorimeter, which covers the polar angular range of $158° \lesssim \theta \lesssim 178°$. In this analysis it is used to measure the scattered positron in events with photon virtualities in the range $2\,\mathrm{GeV}^2 < Q^2 < 80\,\mathrm{GeV}^2$.

2.2.3 Muon Detectors

Two detectors at H1 are designed to identify muons. The Central Muon Detector uses the return yoke of the H1 magnet. The iron is instrumented with limited streamer tubes. The Forward Muon Detector (FMD) is a spectrometer with an iron toroid magnet.

The Central Muon Detector covers an angular range of $5° \lesssim \theta \lesssim 175°$ and is divided into three parts. The forward endcap ($5° \lesssim \theta \lesssim 35°$), the barrel ($35° \lesssim \theta \lesssim 130°$) and the backward endcap ($130° \lesssim \theta \lesssim 175°$). Only muons with a transverse momentum $p_t \gtrsim 1.5\,\mathrm{GeV}$ are able to reach the iron. In this analysis the Central Muon Detector is used together with the Liquid Argon Calorimeter to identify the decay muons.

The Forward Muon Detector [89] complements the central part in the region $3° \lesssim \theta \lesssim 17°$. In this analysis it is used to tag events with proton dissociation.

2.2.4 Forward Detectors

In addition to the forward part of the Liquid Argon Calorimeter and the Forward Muon Detector there is one more detector used in this analysis to tag events where the proton dissociates. This is the Proton Remnant Tagger (PRT). It is situated at $z = +24\,\mathrm{m}$ and consists of seven scintillation counters. The polar angular acceptance of the PRT is $0.06° \lesssim \theta \lesssim 0.17°$.

2.2.5 Luminosity System

The luminosity at H1 [90] is measured using the Bethe-Heitler process $e + p \rightarrow e + p + \gamma$, the cross section of which is known precisely. For the measurement of this process a photon detector at $z = -102.9\,\mathrm{m}$ and an electron tagger at $z = -33.4\,\mathrm{m}$ are used during data taking. During the reconstruction the luminosity is calculated using the information of the photon detector only to reduce the systematic uncertainty.

2.2.6 Trigger System

Not all events measured at the H1 detector are induced by ep-collisions. An even higher rate of events comes from different sources of background. First of all there are collisions of beam particles with the rest gas inside the beampipe or the beampipe itself. Another source is the synchrotron radiation from the positron beam. The number of these events

can be reduced by collimators around the beampipe in the area close to the detector. Finally there are particles from cosmic rays travelling through the H1 detector at a rate of roughly 10 kHz. The muons from cosmic rays play an important role as background of the selected events in this analysis (see section 3.3.2). To suppress the background a system of four trigger levels is used.

At the first level [91] the event rate of the bunch crossings of approximately 10 MHz is reduced to 5 kHz within $2.3 \mu s$. All detector components provide trigger elements, which are logically combined to 128 subtriggers. If the conditions of any of these subtriggers are fulfilled by an event, an *L1 keep* signal is sent to all subdetectors.

Due to the fact that the third trigger level is not used during HERA I data taking, the first trigger level has to reduce the event rate further down. Therefore certain high rate L1 subtriggers get a prescale n which forces them to take only each nth event fulfilling their conditions. The prescale factor is taken into account later on in this analysis, when the number of events is corrected for detector effects [92].

In this analysis four out of the 128 subtriggers are used.

s15: (Mu_Bar || Mu_ECQ) && DCRPh_THig && zVtx_sig
is a muon trigger with one muon candidate in the Central Muon Detector, one high momentum track in the CJC and a reconstructed primary vertex.

s54: zVtx_Cls && DCRPh_TNeg && DCRPh_THig && Topo_BR
is a topological trigger requiring two back-to-back tracks, a negative charged particle, a high momentum track and a reconstructed primary vertex.

s56: (SPCLe_IET>1 || SPCLe_IET_Cen_2) && DCRPh_Ta && Mu_Any
is a muon trigger with one muon candidate in the Central Muon Detector, a central track and an energy deposition of more than 2 GeV in the SpaCal.

s61: (SPCLe_IET>2 || SPCLe_IET_Cen_3) && DCRPh_THig && zVtx_sig
is a DIS trigger with a high momentum track, a reconstructed primary vertex and an energy deposition in the SpaCal of more than 6 GeV in the SpaCal.

The **Muon Trigger** uses five limited streamer tubes of the Central Muon Detector. In the barrel region (Mu_Bar) two of the first four layers are required and in the endcaps (Mu_ECQ) three out of the five layers.

The **DCRPh Trigger** [93] is based on the $r\phi$ information of the Central Jet Chamber. DCRPh_Ta requires at least one track with $p_t \gtrsim 450$ MeV. Tracks with a transverse momentum of $p_t \gtrsim 800$ MeV fulfil the trigger condition DCRPh_THig. The trigger element DCRPh_TNeg requires at least one track corresponding to a negative charged particle.

The **zVtx Trigger** [94] uses information of the Central Proportional Chambers. If a track is reconstructed pointing to a vertex in the region of $|z| < 40$ cm a 16-bin histogram is filled corresponding to the z-position. The element zVtx_Cls requires entries in up to four neighbouring bins of the histogram. This trigger element was broken during some parts of the 1999 $^+$ data taking. Therefore this run region is excluded from this analysis.

zVtx_sig has requirements concerning the ratio between the number of all entries in the histogram and the maximum bin content.

The **Topological Triggerelement** Topo_BR requires two tracks which in the $r\phi$-plane have a back-to-back topology.

The **SpaCal Trigger** [95] is divided into two different sets of trigger elements. One set of elements is used to veto background events which are early or late in time compared to the nominal event timing. The other set of trigger elements is used to trigger ep-collision events. The SpaCal is divided into 16 regions, called *trigger towers*. The element SP-CLe_IET>1 requires at least one such tower with an energy deposition of $E > 2\,\mathrm{GeV}$ in the outer region $R > 16\,\mathrm{cm}$. The condition SPCLe_IET>2 consists of the same requirements, but with an increased energy cut $E > 6\,\mathrm{GeV}$. The other two SpaCal trigger elements used in this analysis repeat the same requirements for the inner $R < 16\,\mathrm{cm}$ part of the SpaCal.

The second trigger level [96] is used to validate the L1 decisions and to further reduce the event rate. The L2 decision has to be taken within $20\mu s$. Without the third trigger level in action the rate has to be reduced to even $50\,\mathrm{Hz}$ using the prescale of the first trigger level. There are two different types of trigger used at level two; a topological trigger [97, 98] and a neural network trigger [99, 100]. The L1 subtriggers used in this analysis in the regime of photoproduction are confirmed by a L2 neural network trigger each [101].

L2NN(4): is a neural network trained to find di-muon events and is used to confirm the L1 subtrigger *s54*.

L2NN(5): is a neural network designed to select events with at least one muon. This network is used to confirm the L1 subtrigger *s15*.

If an event is accepted by any of these level two triggers a *L2 keep* signal is sent. Now the readout of the detector information follows within a dead time of $1 - 2$ ms.

The third level is not used during the data taking periods of this analysis and will be added for the running of HERA II.

The fourth trigger level verifies the previous decisions. It is implemented as a farm of processors, which have the full event information. A reconstruction is performed and the events are classified in several different physics groups. In this analysis events of the L4 trigger class 16 are used. This class consists of heavy flavour event candidates having at least two tracks with an invariant mass above $2\,\mathrm{GeV}$, which are subsequently divided into six subclasses differing in a set of electron-, muon- and track requirements (see appendix C in [77]). In total an event rate of $10\,\mathrm{Hz}$ is written out to permanent storage.

3 Selection

In this analysis two different kinematic regions are studied. This chapter describes the criteria to select the two different data samples. Both contain elastic J/ψ candidates, the first one in the regime of photoproduction and the second one of deep inelastic scattering events.

3.1 Run Selection

For this analysis not all data taken by H1 during the years 1999 and 2000 are useful. During 1999 some special runs, so called *minimum bias* runs were taken with a special trigger setup. In 2000 there were some dedicated runs, with a shifted interaction point. These two special types of runs are not included in this analysis.

During the data taking each run is classified as *good*, *medium* or *bad* depending on the high voltage and readout status of the detector components. Only runs labelled as good or medium runs are considered here. The runs are divided into different trigger phases, according to the trigger setup. Runs of trigger phase one, which corresponds to runs taken at an early stage of a luminosity fill, are excluded. It is required that all relevant detector components were operational. In addition, runs with known problems with detector components important for this analysis are not included (e.g. during 1999 there have been problems with the Outer Jet Chamber CJC2 and several runs with trigger problems are excluded). A full list of all runs excluded due to such problems is given in appendix A.

The same run selection is applied when calculating the integrated luminosity taking also the trigger level one prescale factors into account (see section 4.6.2). A correction for the luminosity from early or late satellite bunches is applied. To reject these events a cut on the vertex $|z_{\mathrm{vtx}} - z_{\mathrm{nom}}| < 40\,\mathrm{cm}$ is applied to the data. An overview of the luminosities produced by HERA and the fraction used in this analysis is given in table 3.1.

Figure 3.1 shows the number of signal events without activity in the forward detectors per integrated luminosity for diffractive J/ψ photoproduction and electroproduction after the full selection described in this chapter. For a better comparison the numbers for the data taking periods in 1999 are scaled by the ratios of the total efficiencies (see section 4.8) in 1999 (e^- or e^+) and 2000. The flat distributions show that there are no big changes in the detector and trigger setup during each data taking period.

		1999 e$^-$	1999 e$^+$	2000	sum
$\mathcal{L}$ prod. by HERA	[pb^{-1}]	18.32	29.39	70.59	118.30
$\mathcal{L}$ delivered to H1		17.42	27.63	67.89	112.94
$\mathcal{L}$ H1 on tape		15.73	24.78	59.26	99.77
$\mathcal{L}$ H1 G + M runs		14.81	23.36	56.08	94.25
$\mathcal{L}$ HV ok		11.17	20.03	51.54	82.74
$\mathcal{L}$ sat. bunch corr.		10.74	18.91	49.18	78.83
$\mathcal{L}$ used in analysis		8.71	6.20	39.88	54.79
d$\mathcal{L}$ total	[%]	1.30	1.50	1.45	1.43

Table 3.1: Integrated luminosities 1999 to 2000 [102]. The last row gives the uncertainty on the luminosity measurement.
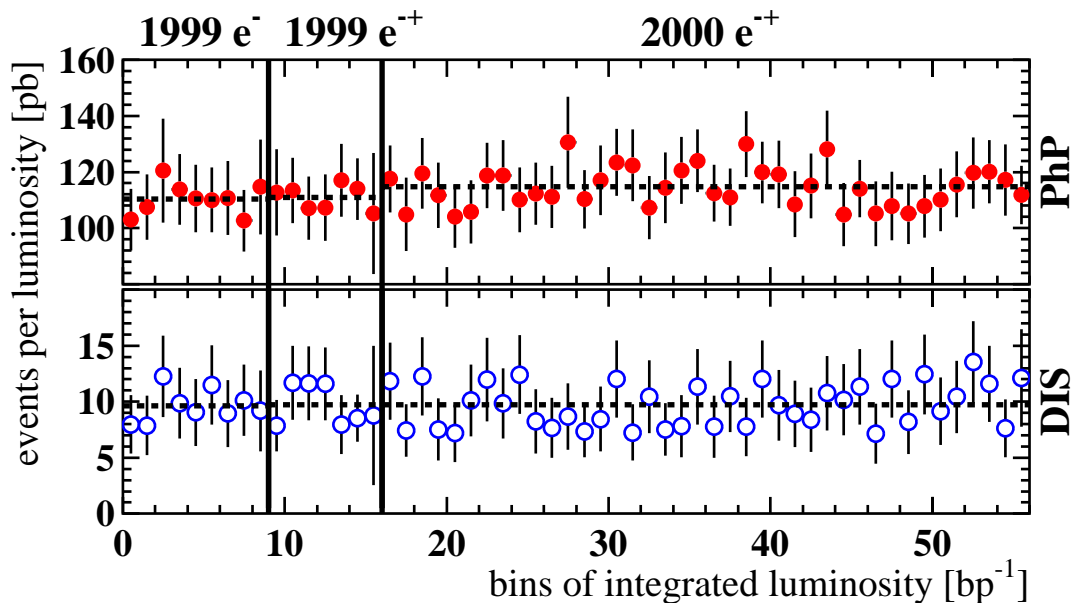
Figure 3.1: Number of untagged J/ψ candidates in bins of $\sim 1\,\text{pb}^{-1}$ for photoproduction (PhP) and electroproduction (DIS) after the full selection. The numbers for the data taking periods in 1999 are scaled by the ratios of the total efficiencies (see section 4.8) in 1999 (e^- or e^+) and 2000. The error bars show the statistical errors only. The dashed lines display the mean value derived for each data taking period separately.

3.2 Decay Lepton Identification

The J/ψ meson is identified here via its decay into two muons. The muons have to fulfil two sets of requirements. A summary of the decay lepton related cuts can be found in table 3.2.

3.2.1 Tracks

First there are conditions on the tracks measured in the central tracking detector. In order to select J/ψ candidates all events with exactly two central tracks originating from the primary vertex are selected. The polar angular range is $20° \leq \theta < 160°$. Only for the proton dissociation background one additional track below $\theta < 10°$ is allowed. The two good central tracks[1] are required to have opposite charges. To improve the quality of the track reconstruction a minimal track length of 10 cm and a starting point in CJC1 is required.

Here only the applied cuts are discussed. A more detailed description of the reconstruction of tracks at H1 can be found in [76, 103].

tracks	identification
$20° \leq \theta < 160°$	≥ 1 CMD linked track OR
$p_t > 0.8\,\text{GeV}$	≥ 1 track with $Q_\mu \geq 2$
$C_1 \neq C_2$	
$R_{\text{start}} < 50$ cm	
$R_{\text{track}} > 10$ cm	

Table 3.2: Requirements for the decay leptons.

3.2.2 Muon Identification

The second requirement concerns the identification of tracks as muons. More information on that topic can be found in [78, 79, 104].

The muons are identified in the LAr Calorimeter and/or in the Central Muon Detector (CMD). To be able to pass the Calorimeter or to reach the instrumented iron, the muons need a minimal momentum. Therefore a cut $p_t > 0.8\,\text{GeV}$ is applied.

In the LAr Calorimeter the muons are identified by the characteristic signature of a minimally ionising particle. Using different energy and track length criteria a muon identification quality is derived. This quality Q_μ covers a range of *none* ($Q_\mu = 0$) up to *good* ($Q_\mu = 3$). For this analysis a quality $Q_\mu \geq 2$ is required. Figure 3.2 shows the mass spectra for the two-track data sample requiring no, one and two identified muons. For this analysis at least one of the two decay tracks has to be identified as a muon either by the CMD or the LAr Calorimeter. The identification efficiency of one muon track is typically around 80% depending on its p_t and θ (see section 4.6.1).

---

[1]In H1 terminology these tracks are referred to as *Lee-West-tracks* described in [103].
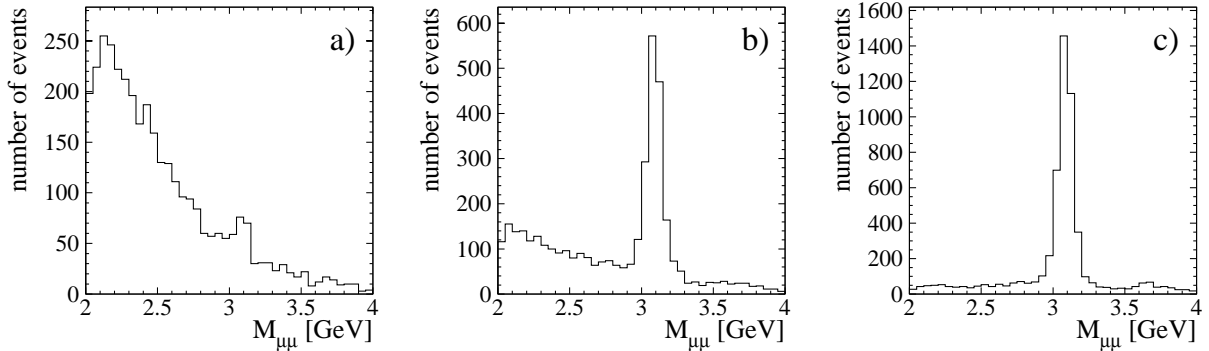
Figure 3.2: Mass spectra for a) no, b) one and c) two identified muons in events of the year 2000 passing all other analysis cuts.

3.3 Background Suppression

The next step in the selection chain is the background suppression. The aim is to reject as much background as possible, without losing too much signal. One has to consider the processes which also pass the selection criteria. In this analysis there are two different types of background.

3.3.1 Resonant Background

On the one hand there is a resonant background coming from $\psi(2S)$ decays. In $(23.9 \pm 1.2)\%$ the $\psi(2S)$ decays into a J/ψ and neutral particles [3], where the J/ψ subsequently decays into two muons. The ratio of the elastic cross sections for the J/ψ and the $\psi(2S)$ production has been measured at H1 [43]:

$$\sigma_{\psi(2S)}/\sigma_{J/\psi} = 0.166 \pm 0.007(stat.) \pm 0.008(sys.) \pm 0.007(BR)$$

Therefore one expects a contribution of $(4.0 \pm 0.5)\%$ to the J/ψ signal arising from decays of $\psi(2S)$ which is not suppressed. The mode

$$\psi(2S) \to J/\psi \pi^+ \pi^-$$

has the biggest branching ratio $(30.5 \pm 1.6)\%$ of the $\psi(2S)$ decays including a J/ψ meson. For elastic photoproduction it has been shown that this background is suppressed by the two track requirement and therefore negligible [77].

3.3.2 Non-Resonant Background

There is also non-resonant background due to lepton pair production and cosmic ray muons. Some of those events are filtered out by the trigger system. To increase the purity of the data sample additional cuts are applied to reduce the background from cosmic ray muon events.

Cosmic ray muons travelling through the H1 detector from top to bottom will be reconstructed as two tracks, which have a back-to-back topology. There is a relationship between the invariant mass $M_{\mu\mu}$ of the two muons and the γp centre-of-mass energy W:

$$M_{\mu\mu}^2 = (p_{\mu 1} + p_{\mu 2})^2 \simeq 2p_{\mu 1}p_{\mu 2} = 4p^2$$

where

$$
\begin{aligned}
p_{\mu 1} &= (p, 0, p\sin\theta, p\cos\theta) \\
p_{\mu 2} &= (p, 0, -p\sin\theta, -p\cos\theta)
\end{aligned}
$$

are the four-vectors of the two tracks of a cosmic ray muon seen in the detector. In the region of photoproduction the squared centre-of-mass energy W is given by equation (1.2) which can be transformed into (using the equations (1.1) and (3.1))

$$W^2 \approx ys = \frac{E - p_z}{2E_e} 4E_e E_p = 2(E - p_z)E_p = 4pE_p \simeq 2M_{\mu\mu}E_p$$

leading to the relation

$$W \simeq \sqrt{2M_{\mu\mu}E_p}$$

where E_e and E_p are the positron and the proton beam energy respectively. In figure 3.3 a) the relation can be seen as a broad band in the $M_{\mu\mu}W$-plane. The following cuts remove this band leading to a slightly reduced selection efficiency at $W \approx 80\,\mathrm{GeV}$ for the photoproduction sample.
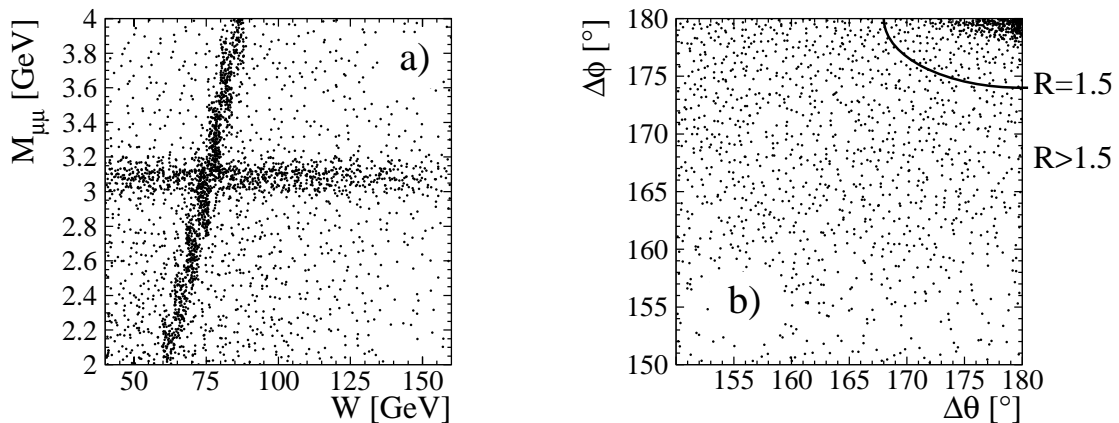
Figure 3.3: a) Mass $M_{\mu\mu}$ versus centre-of-mass energy W before applying cuts against cosmic ray background. The horizontal band shows J/ψ candidates, while the vertical band refers to cosmic ray muons. b) $\Delta\theta\Delta\phi$-plane of the muon tracks. The solid line shows the ellipse corresponding to $R = 1.5$ explained in the text.

For cosmic ray muons the timing of the upper track is early compared to the lower track, because a cosmic ray muon traverses first the upper, then the lower half of the jet chamber, while a J/ψ decaying into two muons and coming from the vertex region generates two

29
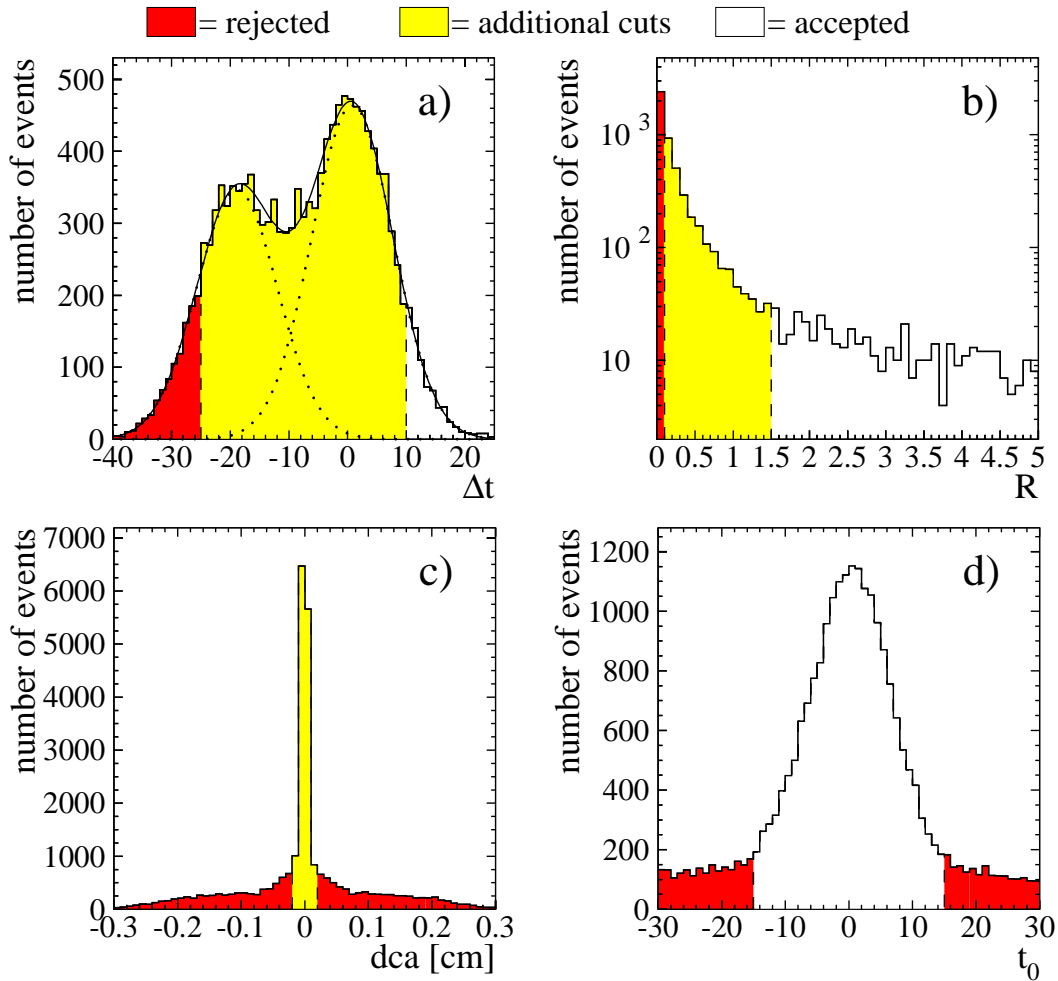
Figure 3.4: Distributions used to cut on background events. In each plot the dark shaded region is cut. The light shaded region is subject to additional cuts shown in the next plot. The sequence of the cuts follows from a) to d).

tracks at the same time. Figure 3.4 a) shows the difference Δt of the two track timings. The Gaussian distribution around zero contains the J/ψ events, whereas the cosmic ray muons are contained in a second peak at -18 ticks (500 ticks $= 96$ ns). Due to the fact that the two peaks are overlapping, the events are classified into three regions in Δt:

- Events in the region $\Delta t < -25$ are rejected as cosmic ray muons.

- Events with $\Delta t > 10$ are considered good J/ψ candidates and are kept without further cuts against cosmic ray background.

- In the intermediate region additional cuts are applied to reduce the remaining cosmic ray muons.

A cut on the angles $\Delta\theta$ and $\Delta\phi$ between the two tracks is applied by cutting on the ellipse

variable R

$$R = \sqrt{\left(\frac{180° - \Delta\theta}{8°}\right)^2 + \left(\frac{180° - \Delta\phi}{4°}\right)^2}$$

shown in figure 3.4 b). The ellipse in the $\Delta\theta\Delta\phi$-plane (see figure 3.3 b)), accounts for the different resolutions of the H1 detector in both variables. All cosmic ray muon tracks have a back-to-back topology. However, in the reconstruction of the tracks a beam spot constrained vertex fit is applied in the $r\phi$-plane. Therefore close-by tracks are forced to point to the nominal vertex leading to an additional migration in the $\Delta\theta\Delta\phi$-plot.

As before three regions of interest are defined:

- Events with $R < 0.1$ are rejected as cosmic ray muons.

- Events with $R > 1.5$ are kept as good J/ψ candidates.

- In the intermediate region two more cuts are applied.

Both additional cuts use the fact, that cosmic ray muons are equally distributed over time and space in the detector. A cut on the distance of closest approach of the track to the run vertex $dca < 0.02\,\mathrm{cm}$ is applied. The last criterium to suppress cosmic ray muons is a cut on the event timing t_0. Here $|t_0| < 15$ ticks is requested.

Figure 3.5 shows the effect of the applied cuts in the $M_{\mu\mu}W$-plane and the Δt distribution.
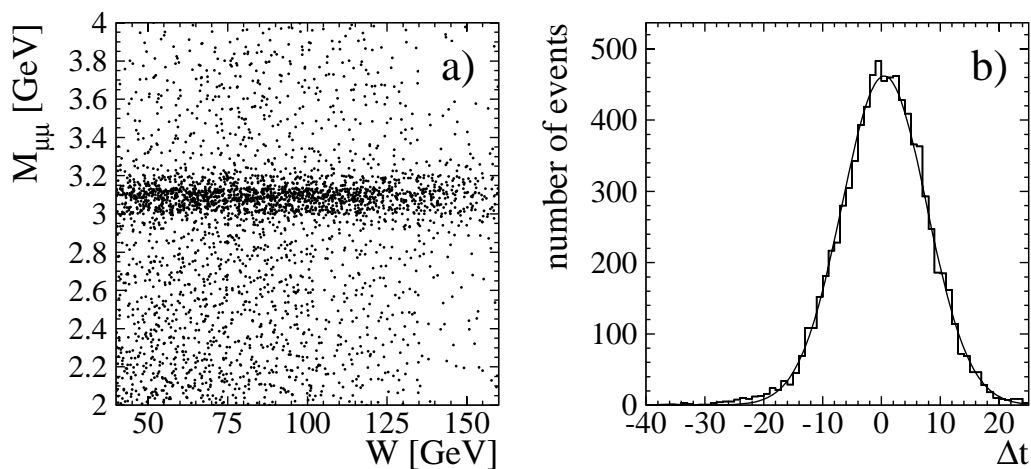
Figure 3.5: a) shows the mass $M_{\mu\mu}$ versus the centre-of-mass energy W after applying cuts against cosmic ray background. b) shows the difference of the track timing of the two muons Δt after the cuts.

3.4 Separation of Elastic and Proton Dissociative Events

In this analysis the main focus is on the elastic production of J/ψ mesons. The largest background contribution is diffractive J/ψ production with proton dissociation[2].

The main criteria used to distinguish elastic events from those with a dissociating proton is activity in the forward region of the detector. This section describes the separation of the data into a sample of events with and without activity in the forward detectors. The cuts discussed in this section are summarised in table 3.3 and illustrated in figure 3.6.

Most of the events with proton dissociation are rejected by demanding no deposits in the forward section of the LAr calorimeter ($\theta < 10°$), the Proton Remnant Tagger ($0.06° < \theta < 0.26°$) and the Forward Muon Detector ($3° < \theta < 17°$).

	elastic J/ψ selection		proton dissociative J/ψ selection
	$E_{\text{LAr10}} < 0.75\,\text{GeV}$		$E_{\text{LAr10}} \geq 0.75\,\text{GeV}$
AND	$N_{\text{FMD}} \leq 1$	OR	$N_{\text{FMD}} > 1$
AND	$N_{\text{PRT}} = 0$	OR	$N_{\text{PRT}} > 0$
AND	no track with $\theta < 10°$	OR	≤ 1 track with $\theta < 10°$

Table 3.3: Cuts to separate elastic events from those with proton dissociation.
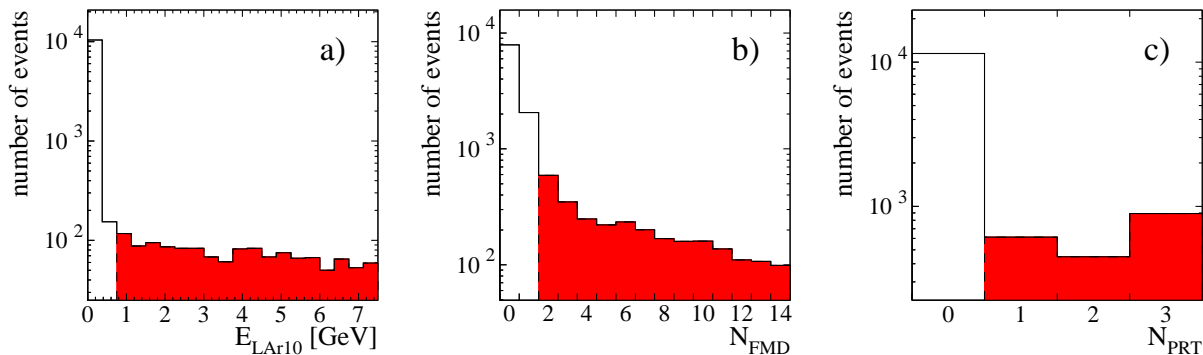
Figure 3.6: Distributions used to separate elastic events from those with proton dissociation. The dark shaded region is cut away for elastic events. a) Energy deposition in the forward region of the calorimeter. b) Number of hits in the layers of the Forward Muon Detector. c) Number of hits in the first three scintillators of the Proton Remnant Tagger.

For each of the three detector components one quantity is used for the forward selection. In the LAr Calorimeter the energy deposition E_{LAr10} for the region $\theta < 10°$ has to be less than $0.75\,\text{GeV}$. The number of hits N_{FMD} in the layers of the Forward Muon Detector must be less than two. Finally no hits in the first three scintillators of the Proton Remnant Tagger are allowed. Only the first three of the total seven scintillators of the Proton Remnant Tagger are used, because the description in the MC simulation of all channels

---

[2]Events with proton dissociation are not simply cut-out as the non-resonant background, but are selected into a separate data sample also used in the analysis of the helicity structure in section 5.3

simultaneously failed. The first three channels are those with the highest efficiencies. These cuts are motivated by the attempt to balance the efficiency of the selection on the one hand and the miss-identification on the other hand. After this requirement a fraction of around 15% of the remaining events in the data sample are proton dissociative, while around 10% of the elastic events are rejected. The determination of the number of elastic events from the number of events with and without activity in the forward region is described in section 4.5.

3.5 Kinematic Region

In this analysis two different kinematic regions are considered: J/ψ photoproduction and the production in deep inelastic scattering (DIS) are distinguished according to the photon virtuality Q^2. First the scattered positron is searched for by looking for an energy deposition in the backward calorimeter SpaCal. A clustering algorithm assigns each cell to a local energy maximum. Events with an energy deposition of less than $8\,\mathrm{GeV}$ in the SpaCal cluster with the highest energy are collected in the photoproduction sample. The DIS data sample contains events with an energy deposition of more than $12\,\mathrm{GeV}$ and $Q^2 > 2\,\mathrm{GeV}^2$.

Depending on the region in Q^2 different methods are used to reconstruct other kinematic variables. In the photoproduction regime, where the scattered positron disappears undetected down the beam pipe, the kinematic variables y and W are reconstructed using the Jacquet-Blondel method [105]

$$
\begin{aligned}
y_{\mathrm{JB}} &= \frac{\sum_{had}(E - p_z)}{2E_e} \\
W_{\mathrm{JB}} &= \sqrt{s\, y_{\mathrm{JB}} - Q^2 + m_p^2} \\
&\approx \sqrt{s\, y_{\mathrm{JB}} + m_p^2}
\end{aligned}
\tag{3.1}
$$

where $\sum_{had}(E - p_z)$ is the difference between energy and longitudinal momentum summed over the entire hadronic final system (in the elastic case the two muon tracks). E_e denotes the beam energy of the incoming positrons. $\sqrt{s}$ is the total centre-of-mass energy and m_p the proton mass. The four-momentum transfer squared at the proton vertex t is given by

$$
t = (\mathbf{p}_e - \mathbf{p}_\psi)^2 \simeq -(\vec{p}_{t,e} + \vec{p}_{t,\psi})^2
$$

where $\mathbf{p}_e$ and $\mathbf{p}_\psi$ denote the four momenta of the incoming positron and the vector meson, respectively, while $\vec{p}_{t,e}$ and $\vec{p}_{t,\psi}$ denote the momentum components transverse to the beam direction. In photoproduction the mean value of the photon virtuality is $\langle Q^2 \rangle = 0.05\,\mathrm{GeV}^2$, thus $\vec{p}_{t,e}$ is negligible and t can be approximated by the transverse momentum of the vector meson

$$
t \simeq -\vec{p}_{t,\psi}^{\,2}.
$$

In the deep inelastic scattering region, the scattered positron is detected. Here the double angle method [106] using the polar angles $\theta_{e'}$ and θ_ψ of the scattered positron and the J/ψ meson respectively can be used to reconstruct Q^2, y and W:

$$Q^2_{\mathrm{DA}} = 4E_e^2 \frac{\sin\theta_\psi(1 + \cos\theta_{e'})}{\sin\theta_\psi + \sin\theta_{e'} - \sin(\theta_{e'} + \theta_\psi)}$$

$$y_{\mathrm{DA}} = \frac{\sin\theta_{e'}(1 - \cos\theta_\psi)}{\sin\theta_\psi + \sin\theta_{e'} - \sin(\theta_{e'} + \theta_\psi)}$$

$$W_{\mathrm{DA}} = \sqrt{s\, y_{\mathrm{DA}} - Q^2 + m_p^2}$$

$$t \simeq -(\vec{p}_{t,e} + \vec{p}_{t,\psi})^2$$

where $\vec{p}_t, e$ is reconstructed using the measured energy deposition $E_{e'}$ of the scattered positron.

For both data samples a cut on the centre-of-mass energy of the photon-proton system $40\,\mathrm{GeV} < W < 160\,\mathrm{GeV}$ is applied. In addition a cut on the four-momentum transfer squared at the proton vertex is used. For the selection of the elastic J/ψ candidates $|t| < 1.2\,\mathrm{GeV}^2$ is required. The selection in W is motivated by the geometrical detector acceptance (see section 4.8). The cut on t is motivated by the separation of the elastic and proton dissociative events by the forward detectors. For higher values of t the number of elastic events with activity in the forward region increases (see section 4.6).

To improve the quality of the reconstruction of the kinematic variables in the case of deep inelastic scattering some additional requirements on the scattered positron are applied. An overview of the cuts used to define the two kinematic regions can be found in table 3.4. Figures 3.7 and 3.8 show control distributions of the scattered positron from the DIS data sample comparing data and MC. The MC contains elastic J/ψ events and a contribution of proton dissociation as in the data, both corrected as discussed in chapter 4. The number of events in the MC is normalised to the number of events in the data.

Photoproduction	DIS
$E_{e'} < 8\,\mathrm{GeV}$	$E_{e'} > 12\,\mathrm{GeV}$
	$Q^2 > 2\,\mathrm{GeV}^2$
	$r_{\theta_{e'}} > 9.1\mathrm{cm}$
	$\sum(E - p_z) > 45\,\mathrm{GeV}$
	$E_{\mathrm{veto}} < 2\,\mathrm{GeV}$
	$r_{\mathrm{cl}} < 3.5\mathrm{cm}$
	$155° < \theta_{e'} < 178°$
$40\,\mathrm{GeV} < W < 160\,\mathrm{GeV}$	
$|t| < 1.2\,\mathrm{GeV}^2$	

Table 3.4: Cuts on the scattered positron defining the kinematic regions of photoproduction and deep inelastic scattering (DIS).

The cut on the positron energy $E_{e'}$ assures that the background from misidentified hadrons is small. The energy is derived from clusters in the SpaCal. $r_{\theta_{e'}}$ is the radial distance of the cluster from the beam axis. Another cut to discriminate between electromagnetic
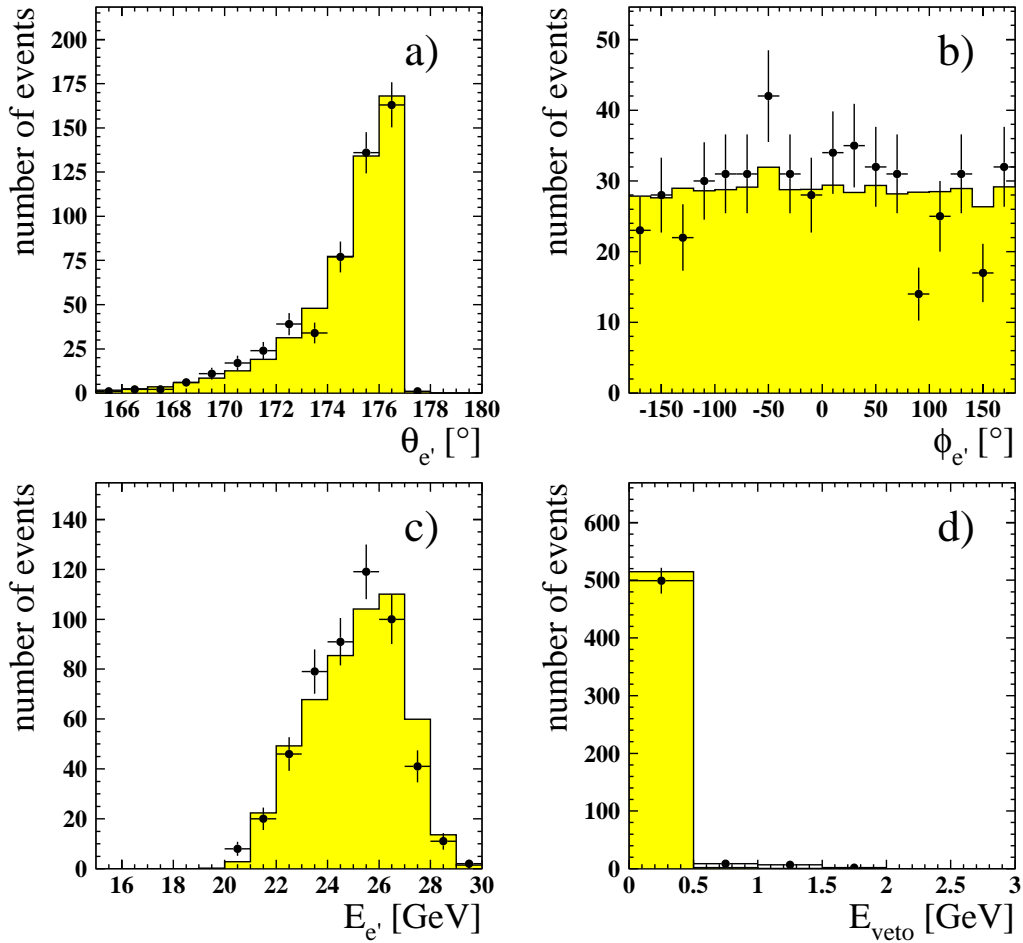
Figure 3.7: Comparison of distributions of the scattered positron in data (points) and MC (shaded histograms) for the DIS selection. The MC contains elastic and proton dissociative events at the same ratio as in data. The number of MC events is normalised to the number in the data. a) and b) show the angular distributions. c) the energy of the scattered positron d) the energy in the veto layers of the SpaCal.

and hadronic showers, which are on average broader, is applied to the energy-weighted cluster radius

$$r_{\rm cl} = \frac{1}{E_{e'}} \sum E_i |\vec{r}_i - \vec{r}_{\rm cog}|$$

where $\vec{r}_{\rm cog}$ is the position of the centre-of-gravity of the cluster relative to the nominal beam axis. The innermost circular layers of the SpaCal are used as veto layers. Requiring an energy $E_{\rm veto} < 2\,{\rm GeV}$ assures that the cluster of the scattered positron candidate lies completely within the SpaCal. The cut on the angle $\theta_{e'}$ of the scattered positron serves the same purpose.
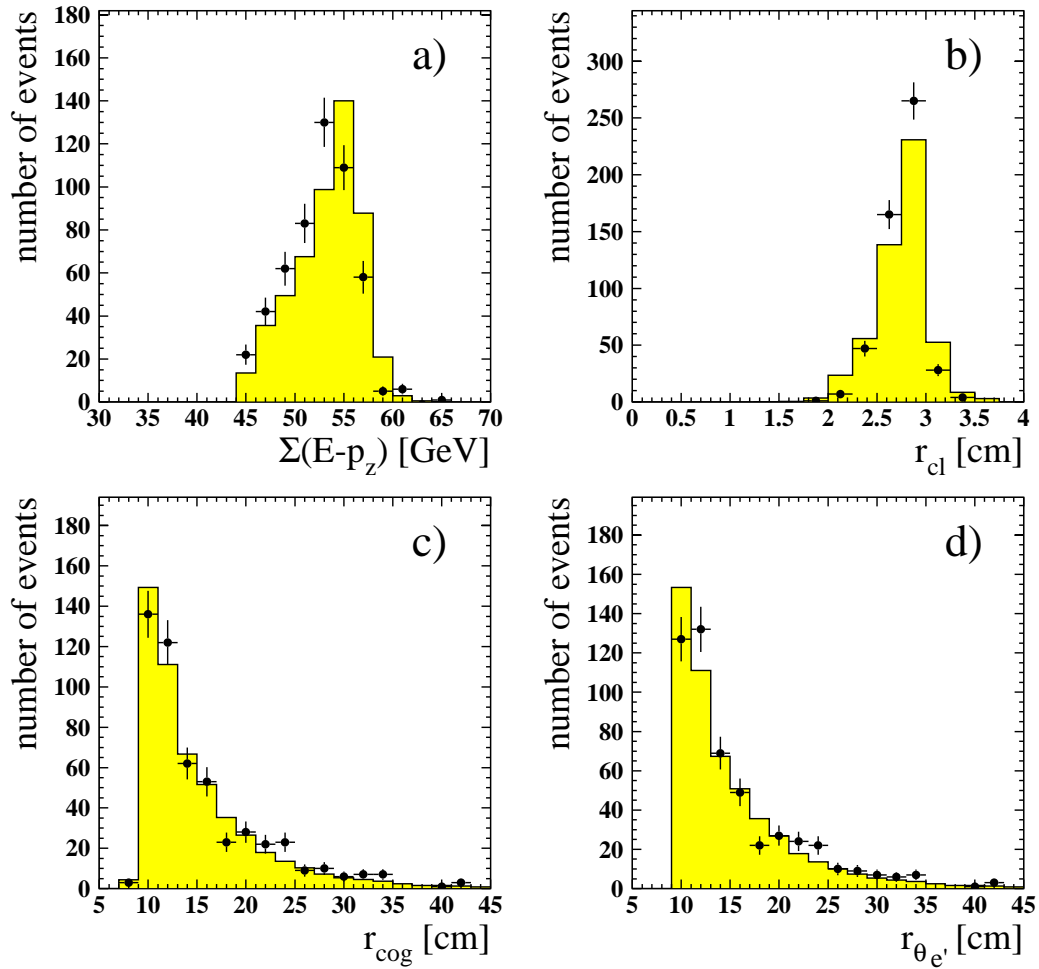
Figure 3.8: Comparison of distributions of the scattered positron in data (points) and MC (shaded histograms) for the DIS selection. The MC contains elastic and proton dissociative events at the same ratio as in data. The number of MC events is normalised to the number in the data. a) difference of the energy and the z-component summed over all particles including the scattered positron, b) energy-weighted cluster radius, c) radial distance of the cluster from the nominal beam axis (centre-of-gravity), d) radial distance of the cluster from the beam axis.

3.6 Trigger and Event Classification

Depending on the kinematic region different subtriggers are used (see also section 2.2.6). For J/ψ photoproduction the two L1 subtriggers $s15$ and $s54$ are used, both verified by L2 neural network triggers. In the regime of deep inelastic scattering subtriggers $s56$ and $s61$ are used. In both cases events that are classified as heavy flavour events in the L4 trigger class 16 are used.

3.7 Selection Summary

After applying all cuts discussed in the previous sections, two data samples remain. Figure 3.9 shows the di-muon mass spectra for the photoproduction and deep inelastic scattering sample. Table 3.5 summarises the effect of the different cuts on the number of events.
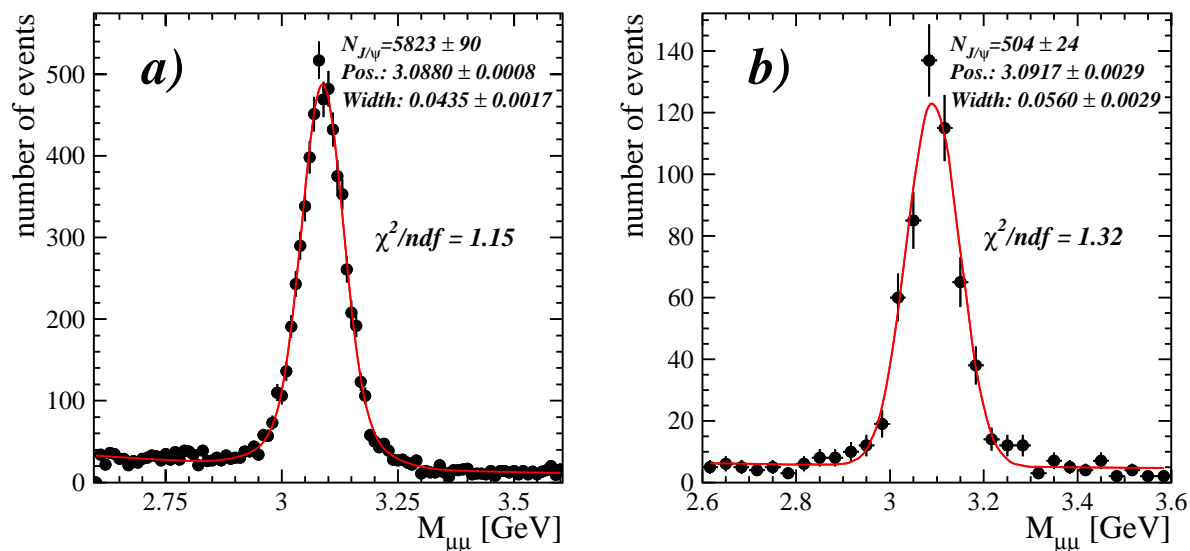
Figure 3.9: The di-muon mass spectra for the two data samples in photoproduction (a) and deep inelastic scattering (b) including all data from the years 1999 and 2000. The solid lines show the results of fits to the data using the sum of a Gaussian and a power law to describe the non-resonant background.

Figure 3.10 shows two J/ψ candidate events as seen in the H1 detector. Event a) is taken from the photoproduction sample. The detector shows a clean two track event signature, where both tracks are identified as minimum ionising particles in the Liquid Argon Calorimeter. In addition, one of the tracks reaches the iron. Because of the high activity in the forward region this event is classified as proton dissociative.

The event b) is of the DIS data sample. The event display shows a clean three-track event without activity in the forward region. One of the tracks is identified as the scattered positron leaving a large energy deposition in the electronic part of the SpaCal. The two

other tracks are identified as minimum ionising particle in the hadronic part of the Liquid Argon Calorimeter. As above one of the muon candidates reaches the Central Muon Detector in the iron.

	number of events (signal / background)		see section
two-track events on DST	38.9k / 86.8k		
run selection	27.2k / 37.3k		3.1
decay lepton identification	18.6k / 7.3k		3.2
background suppression	18.4k / 3.7k		3.3
untagged events	8.9k / 1.5k		3.4
	PhP	DIS	
kinematic region	7.6k / 1.2k	0.55k / 0.06k	3.5
trigger & event classification	5.8k / 0.9k	0.55k / 0.06k	3.6

Table 3.5: Overview of the data selection. The number of estimated signal and background events are given after each step in the analysis chain for the combined data samples of the years 1999 and 2000. The numbers are derived using the sum of a Gaussian and a power law to fit the invariant mass spectra.

a) Run: 262530   Event: 15653

b) Run: 270090   Event: 29223
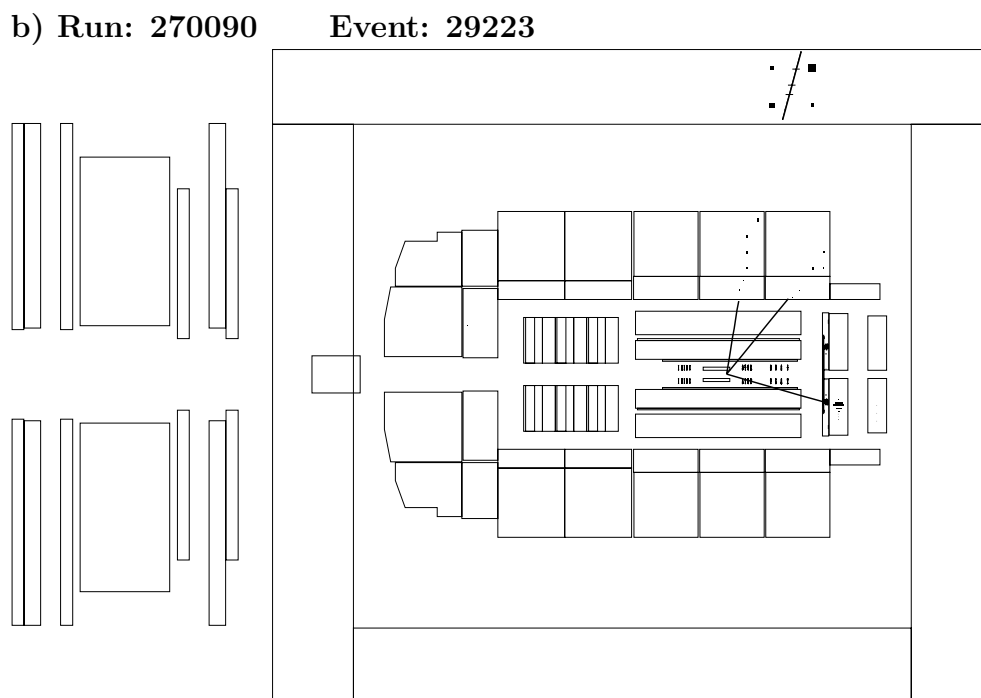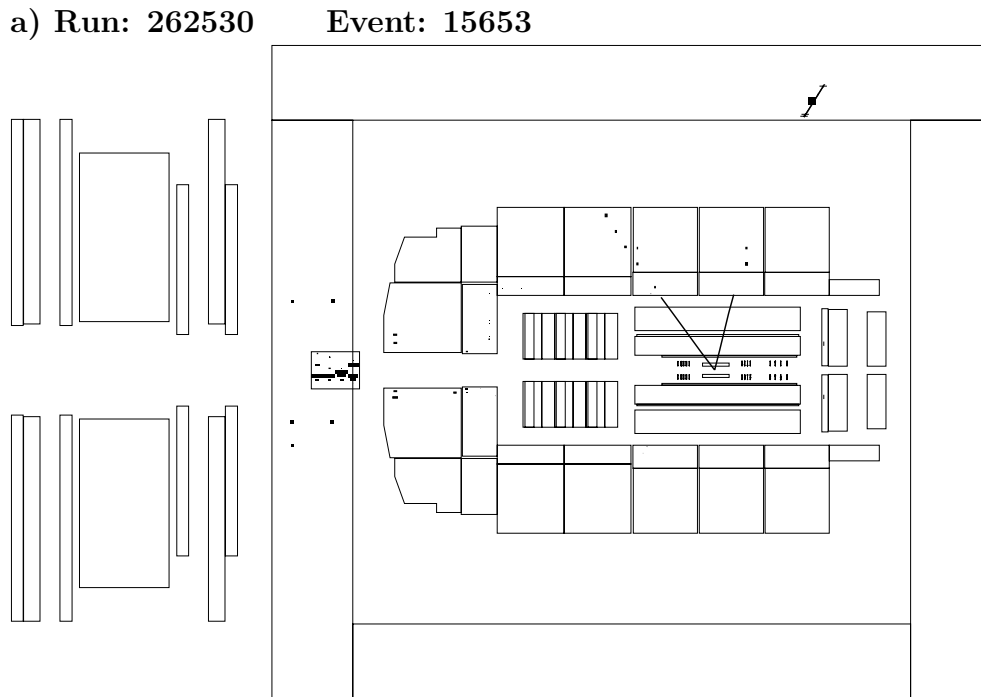
Figure 3.10: Event display of two reconstructed J/ψ candidates. a) shows an event of the J/ψ photoproduction sample with forward activity, while b) shows a forward untagged event of the DIS data sample.

4 Cross Section Extraction

This chapter describes how the cross sections are determined from the data samples discussed in the previous chapter. The cross section is defined and a description of how the analysis bins are chosen follows. In each bin the number of signal events is determined. These numbers are corrected for detector effects using a MC simulation. A comparison of the Monte Carlo simulations with the data is performed. At the end of this chapter the systematical uncertainties are estimated.

4.1 Cross Section Definition

The cross section for diffractive elastic J/ψ production $ep \to eJ/\psi p$ is calculated as

$$\sigma(ep \to eJ/\psi p) = \frac{N_{\text{no tag}} \cdot (1 - f_{\psi(2S)})(1 - f_{pd})}{\epsilon_{tot} \cdot BR \cdot \mathcal{L}} \tag{4.1}$$

where $N_{\text{no tag}}$ denotes the number of events without activity in the forward region. $f_{\psi(2S)} = 0.040 \pm 0.005$ is the correction for background events coming from $\psi(2S)$ decays (see section 3.3). f_{pd} is a correction for events with proton dissociation in the data sample after applying all selection cuts. It is described in more detail together with the total efficiency ϵ_{tot} in section 4.8. BR is the branching ratio for the decay of J/ψ mesons into two muons $(5.88 \pm 0.10)\%$ [3]. $\mathcal{L}$ is the total integrated luminosity for the data taking period (see table 3.1). All cross sections are calculated for each data taking period separately and combined afterwards weighted by the luminosity.

For J/ψ electroproduction radiative corrections are taken into account. The measured cross sections in DIS include processes of higher orders which are negligible for J/ψ photoproduction. The Born cross section in deep inelastic scattering is derived using

$$\sigma^{\text{Born}} = \sigma^{\text{measured}} C_{\text{rad.corr.}}$$

where $C_{\text{rad.corr.}}$ is the correction estimated in each analysis bin (described in section 1.4). Using this relation equation (4.1) transforms to

$$\sigma(ep \to eJ/\psi p) = \frac{N_{\text{no tag}} \cdot (1 - f_{\psi(2S)})(1 - f_{pd})}{\epsilon_{tot} \cdot BR \cdot \mathcal{L}} C_{\text{rad.corr.}}$$

The ep cross sections are to compare with previous experiments converted to γp cross sections according to equation (1.10) $\sigma(\gamma p \to J/\psi p) = \sigma(ep \to eJ/\psi p)/\Phi_\gamma$. Note that

this is only an approximation using the Weizsäcker-Williams-Approximation [107], where the Born cross section is given by

$$\frac{d\sigma_{ep}(y, Q^2)}{dy dQ^2} \approx \Phi_\gamma^T \sigma_{\gamma^* p}.$$

Φ_γ^T denotes the flux of transversely polarised virtual photons and is given by [108]

$$\Phi_\gamma^T = \frac{\alpha_{\text{QED}}}{2\pi y Q^2} \left(1 + (1-y)^2 - 2m_e^2 \frac{y^2}{Q^2} \right).$$

Integration over y and Q^2 leads to

$$\sigma_{ep} = \int_{y_{\text{min}}}^{y_{\text{max}}} dy \int_{Q^2_{\text{min}}}^{Q^2_{\text{max}}} dQ^2 \Phi_\gamma^T(y, Q^2) \sigma_{\gamma^* p}(y, Q^2)$$

The minimum required Q^2 is given by

$$Q^2_{\text{min}} = m_e^2 \frac{y^2}{1-y}.$$

Using the relation between y and W, equation (1.10) is then valid for

$$\Phi_\gamma = \int_{W_{\text{min}}}^{W_{\text{max}}} dW \int_{Q^2_{\text{min}}}^{Q^2_{\text{max}}} dQ^2 \Phi_\gamma^T(W, Q^2)$$

at a certain point (W_0, Q_0^2). This point is defined by the equation

$$\Phi_\gamma = \int_{W_{\text{min}}}^{W_{\text{max}}} dW \int_{Q^2_{\text{min}}}^{Q^2_{\text{max}}} dQ^2 \Phi_\gamma^T(W, Q^2) \left(\frac{W}{W_0} \right)^\delta \left(\frac{M_\psi^2 + Q_0^2}{M_\psi^2 + Q^2} \right)^{-n} \tag{4.2}$$

assuming

$$\sigma_{\gamma^* p} \propto \frac{W^\delta}{(M_\psi^2 + Q^2)^{-n}}.$$

4.2 Bin Centre Correction

In the case that the cross section changes rapidly in a given analysis bin, the calculated value of the cross section does not correspond to the centre of the bin. To correct for these effects different methods are used in this analysis.

In the case of W and Q^2 the approximation described in the previous section i.e. equation (4.2) is used to calculate the values W_0 and Q_0^2. $\delta = 0.7$ and $n = 2.4$ are used which results from the data (see sections 5.1.1 and 5.2.1).

For the t dependence the bin centre is determined using

$$\frac{d\sigma_{\gamma^* p}}{dt}(\langle t \rangle) = \frac{1}{t_1 - t_2} \int_{t_1}^{t_2} dt \frac{d\sigma_{\gamma^* p}}{dt}(t) \tag{4.3}$$

assuming $d\sigma_{\gamma^*p}/dt(t) \propto e^{bt}$. Starting with the centre of the bins b is fitted and a bin centre correction is calculated. This determination is done recursively.

For the angular distributions the mean values of each bin are used, derived from the MC distributions.

In chapter 5 the corrected bin centre values are referred to as mean values.

4.3 Resolutions

Differential cross sections will be given as functions of $W, t, Q^2, \theta^*, \phi^*$ and Ψ. The bin boundaries used to measure the cross section as a function of these variables are determined by the resolution of the detector and the available statistics. To minimise systematic errors the bin size used in the analysis needs to be large compared to the resolution. The resolution is studied with the MC simulation. Figure 4.1 shows distributions of the form $(x_{rec} - x_{gen})/x_{gen}$ where x denotes one of the different variables used in the analysis. The subscript rec denotes the quantities after the reconstruction, while gen denotes the quantities at generator level. The width of a Gaussian distribution fitted to the data is used as a measure of the mean detector resolution.

Figure 4.2 shows the extracted bin resolutions as a function of the variables used. The resolution is always significantly smaller than the bin sizes in the analysis. The values of the bin boundaries used can be found in the tables of chapter 5.

4.4 Purity & Stability

The chosen analysis bins are investigated for their purity and stability. The purity and stability are a measure for the migration between close-by bins. Purity and stability can be extracted using the MC simulation and are determined for each bin used in the analysis according to

$$\text{Purity(i)} = \frac{\text{number of events generated and reconstructed in bin } i}{\text{number of events reconstructed in bin } i}$$

$$\text{Stability(i)} = \frac{\text{number of events generated and reconstructed in bin } i}{\text{number of events generated in bin } i}.$$

The purity gives an estimate of the migration into a bin, whereas the stability shows the fluctuation out of a bin. In figure 4.3 the two functions are given as a function of different variables used in the analysis.
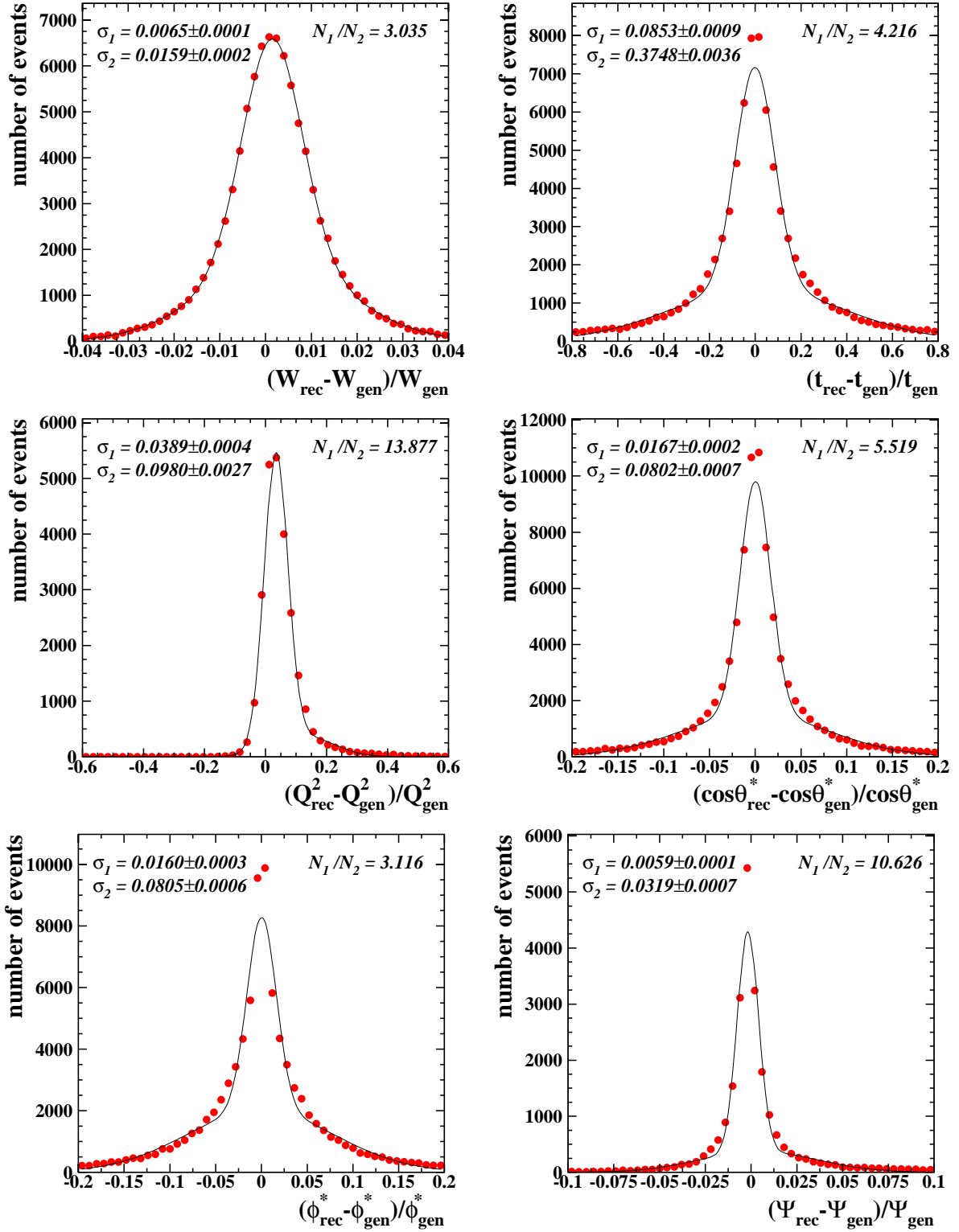
Figure 4.1: Mean detector resolution for different variables extracted from the DIFFVM simulation. The solid lines are the result of a fit to the data using the sum of two Gaussians. The widths of the two Gaussians are given in each plot, together with the ratio of the two amplitudes.
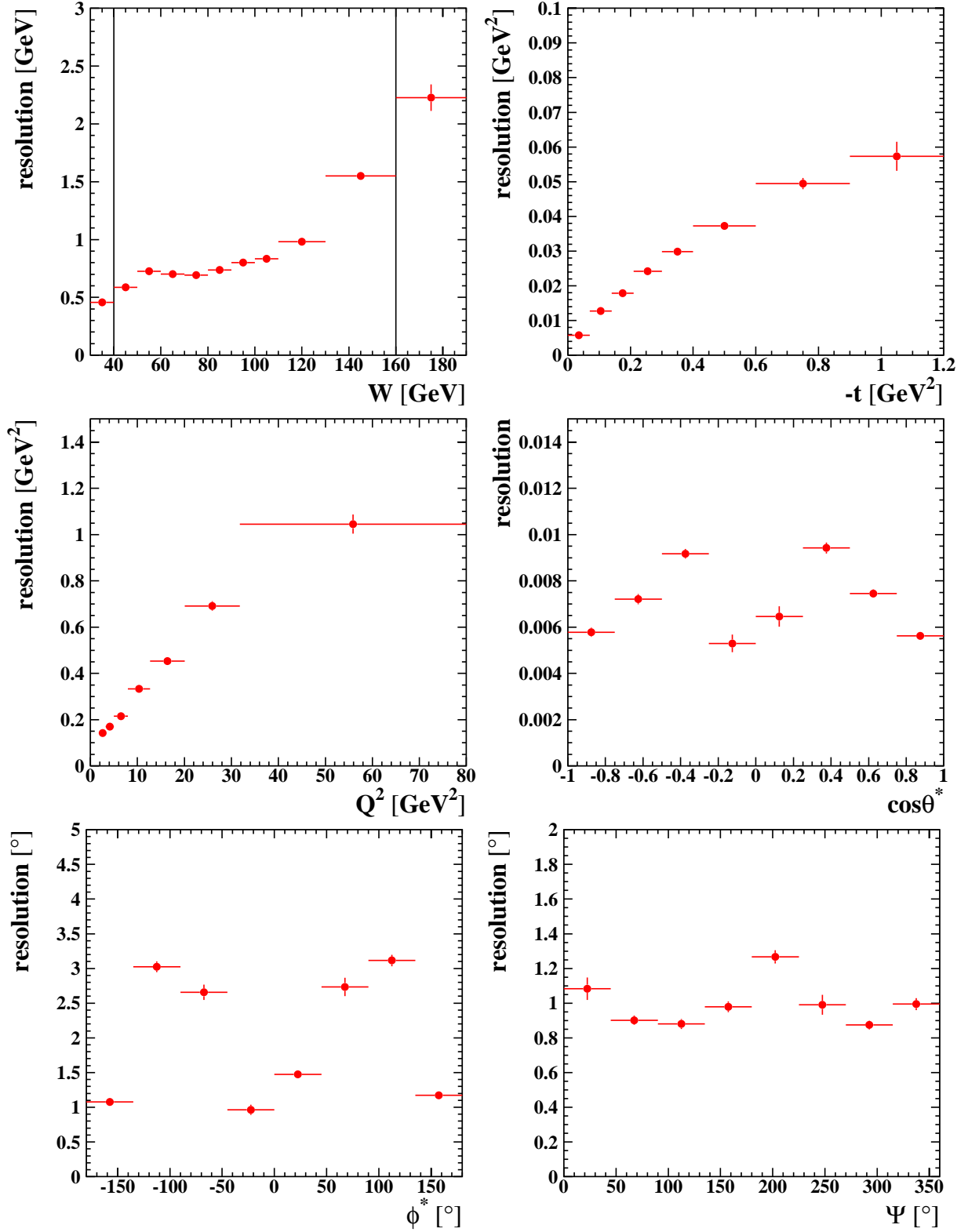
Figure 4.2: Detector resolution as a function of $W, t, Q^2, \theta^*, \phi^*$ and Ψ. Given is the width of a Gaussian fitted to the distribution $x_{rec} - x_{gen}$ in bins of x_{gen}, where x denotes the different variables. The bin sizes chosen for the analysis are indicated by the horizontal error bars. They are significantly larger than the resolution. The vertical lines in the W distribution mark the final analysis region. For the other distributions this cut is already applied.
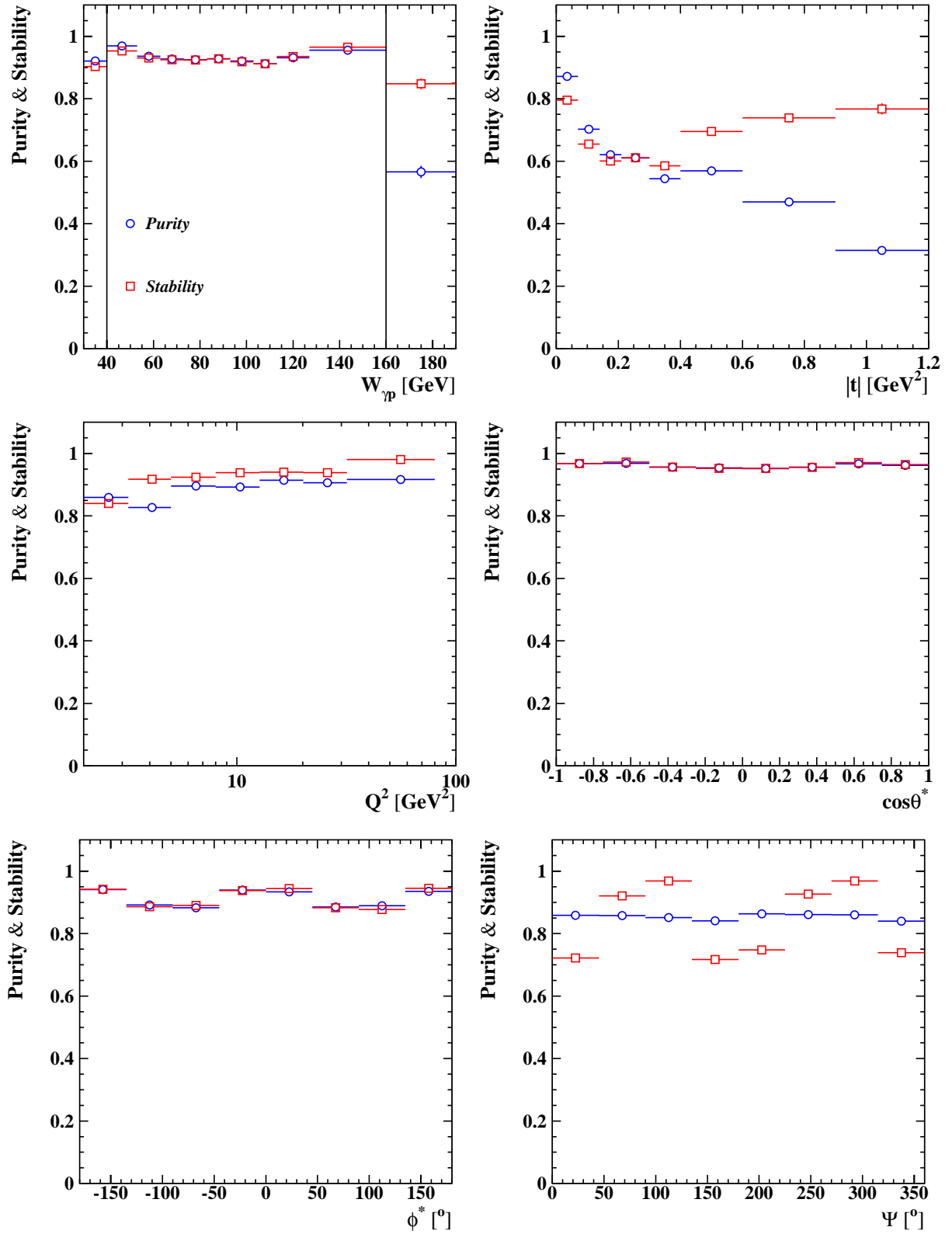
Figure 4.3: Purity and stability as a function of different variables. W, t, Q^2, $\cos\theta^*$, ϕ^* and Ψ. An extended region is shown for W with the analysis boundaries marked in the plot.

4.5 Number of Events

To extract the number of events in a given analysis bin, the invariant mass of the di-muon system is determined and a fit to the data is applied. Figures 4.4 and 4.5 show the mass distributions for different bins in W for the photoproduction data sample as well as the DIS data sample. The signal is fitted using a single Gaussian to which a power law is added to describe the non-resonant background. In some analysis bins i.e. in the DIS data sample of the 1999 e^+ data taking, the statistics are too low to fit the background. In those cases the number of background events is counted in the regions $2.7\,\mathrm{GeV} < M_{\mu\mu} < 2.9\,\mathrm{GeV}$ and $3.3\,\mathrm{GeV} < M_{\mu\mu} < 3.5\,\mathrm{GeV}$ outside the mass window of $\pm 200\,\mathrm{MeV}$ around the nominal J/ψ peak position and an estimate is calculated for the number of background events inside the mass window. The number of signal events is then taken as the difference of the total number of events inside the mass window and the estimated number of background events.
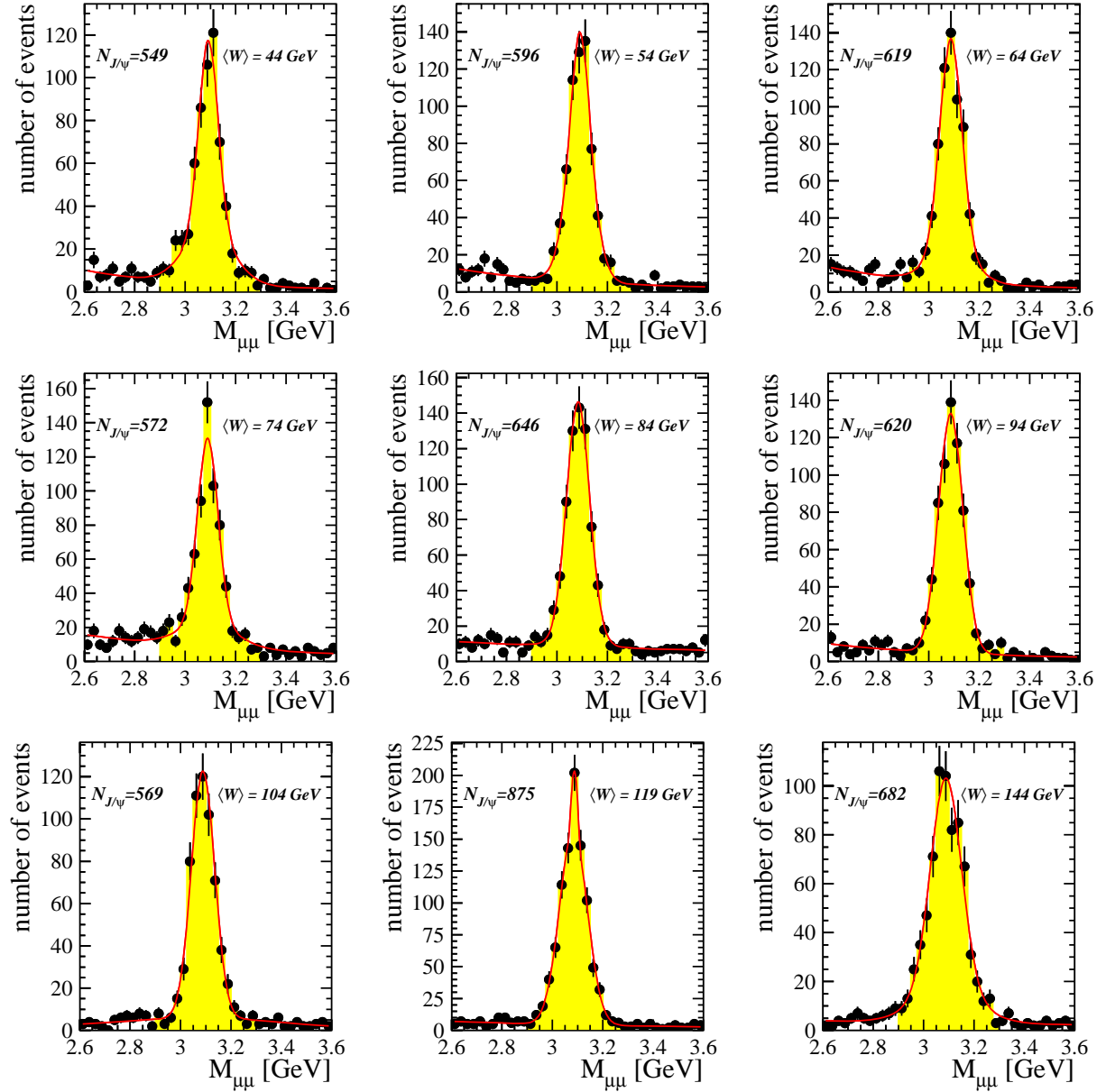
Figure 4.4: Mass distribution of the **photoproduction** data sample in different bins of W. The values of W increase from left to right and from top to bottom. The bin boundaries can be found in chapter 5.
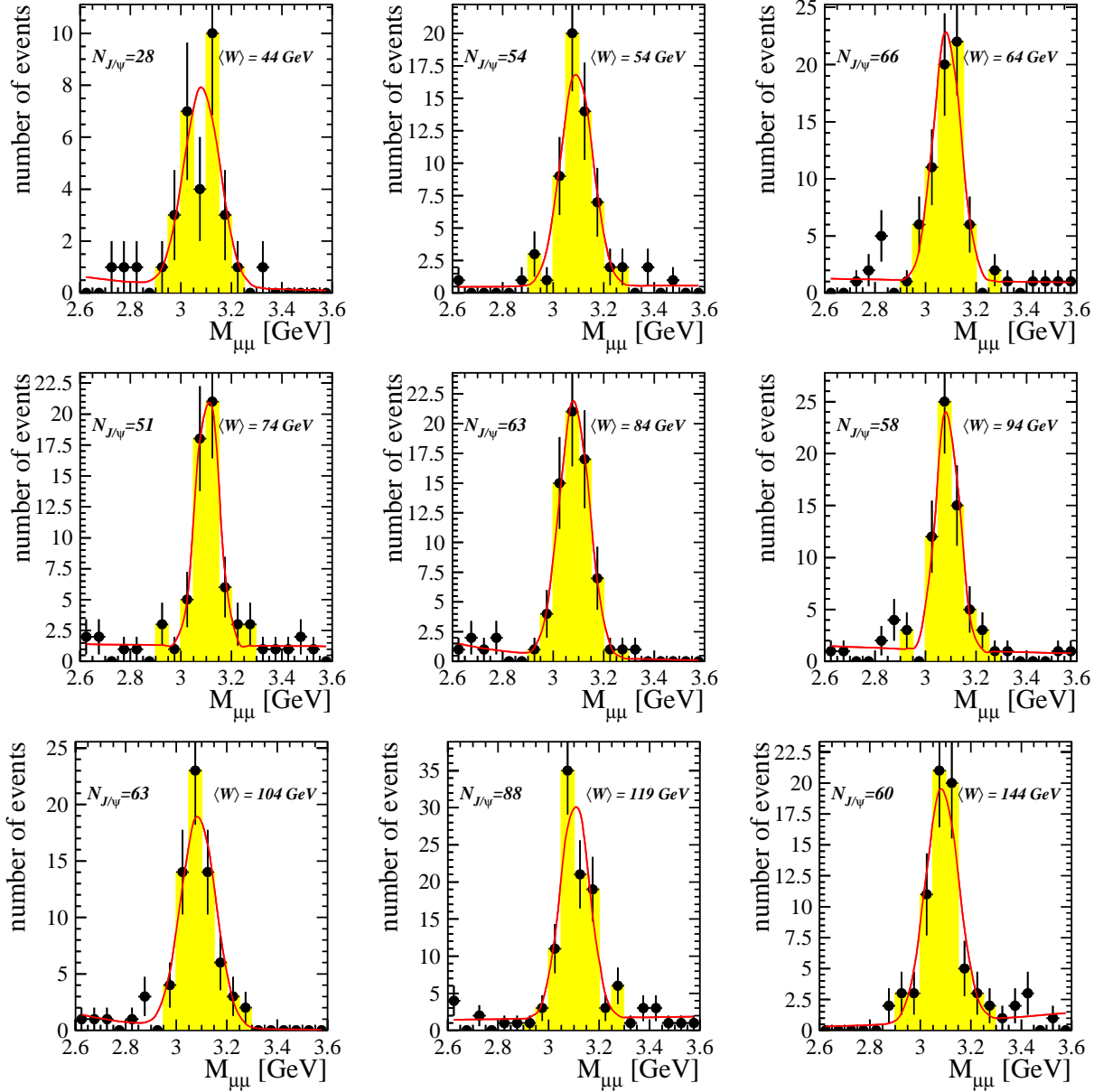
Figure 4.5: Mass distribution of the **DIS** data sample in different bins of W. The values of W increase from left to right and from top to bottom. The bin boundaries can be found in chapter 5.

4.6 Efficiency Correction in the MC

The Monte Carlo generator DIFFVM is used to determine the efficiencies and acceptances of the detector. It is necessary to verify that the MC is able to describe the data. Small adjustments are applied to the simulation where necessary.

The comparison is done in several steps. First the muon identification efficiency is compared between the MC simulation and the data. Next the efficiencies of individual trigger elements are verified. The third step is a comparison of the forward tagging procedure used to separate elastic events and events with proton dissociation.

4.6.1 Muon Identification

In previous analyses [77, 79, 80] of elastic J/ψ production at low t both decay muons have been required to be identified as muons and the identification efficiency in the MC simulation has been corrected as a function of θ. In this analysis also two track events with only one identified muon are included to increase statistics. Due to the high statistics in the year 2000 a more detailed comparison of the identification efficiencies in data and MC is achieved.

For this study a data sample is selected using all cuts described in chapter 3 except for the lepton identification cuts, the trigger selection and the separation of events with proton dissociation. The standard trigger selection is not used, because the subtriggers $s15$ and $s56$ have a muon requirement, which would introduce a bias. Therefore only events triggered by the subtriggers $s54$ and $s61$ are used.

A loop over all tracks in all two prong events in the J/ψ mass region $2.9\,\mathrm{GeV} < M_{\mu\mu} < 3.3\,\mathrm{GeV}$ is performed, testing if at least one of the tracks is identified as a good muon. Under the precondition that the first track is identified as a muon the second track of the current event is then investigated to see if it is also identified as a muon. Figure 4.6 shows ratios of the number of two muon events over the number of all muon tagged events as a function of θ in data and in MC.

This study is performed for muons identified in the LAr Calorimeter and in the Central Muon Detector separately. More muons are identified in the simulation than in data. To extract a correction function for the MC simulation, a polynomial is fitted to the ratio of the efficiency in the data over the one in the simulation as a function of θ. In the analysis this procedure has been repeated separately in three different bins of the transverse momentum p_t (figure 4.7).

A correction function f_i for a single muon track i as a function of θ and p_t is obtained using these polynomials. In order to get the full correction factor which has to be applied to a simulated event, it is necessary to distinguish between events with one or two identified muons.

The simpler case is the one where just one of the two tracks is identified as a muon. Here the correction factor used for the simulated event is just the factor corresponding to θ and p_t of the identified track. In the case that both tracks are identified as muons, the
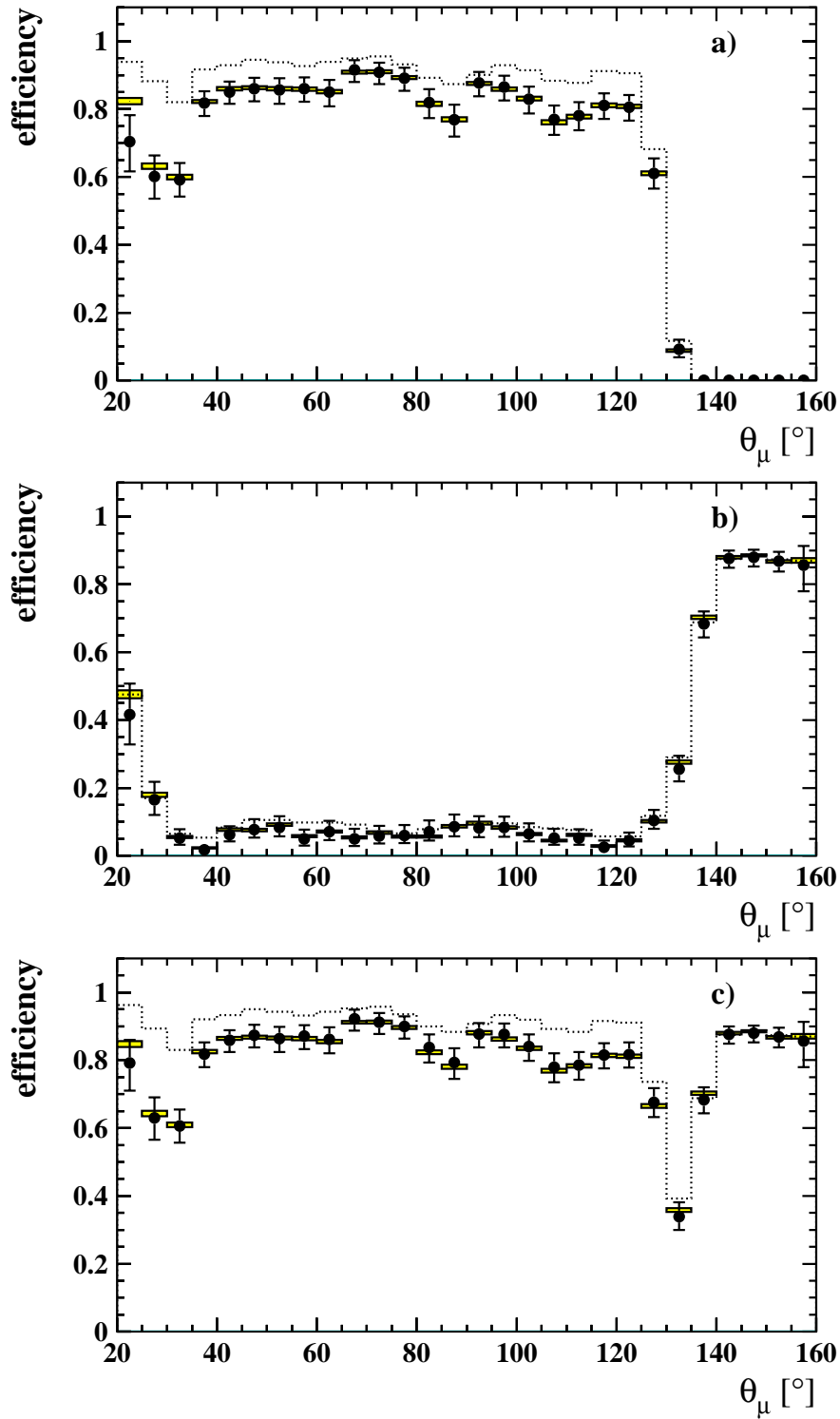
Figure 4.6: Muon identification efficiency in data and MC simulation a) in the calorimeter and b) in the iron and c) for the OR of both as a function of θ integrated over the full range in p_t. The efficiencies of the data are shown as black points with statistical errors. The uncorrected simulation is given as a dotted histogram, whereas the corrected simulation using the equations 4.4 and 4.5 is shown as error boxes.
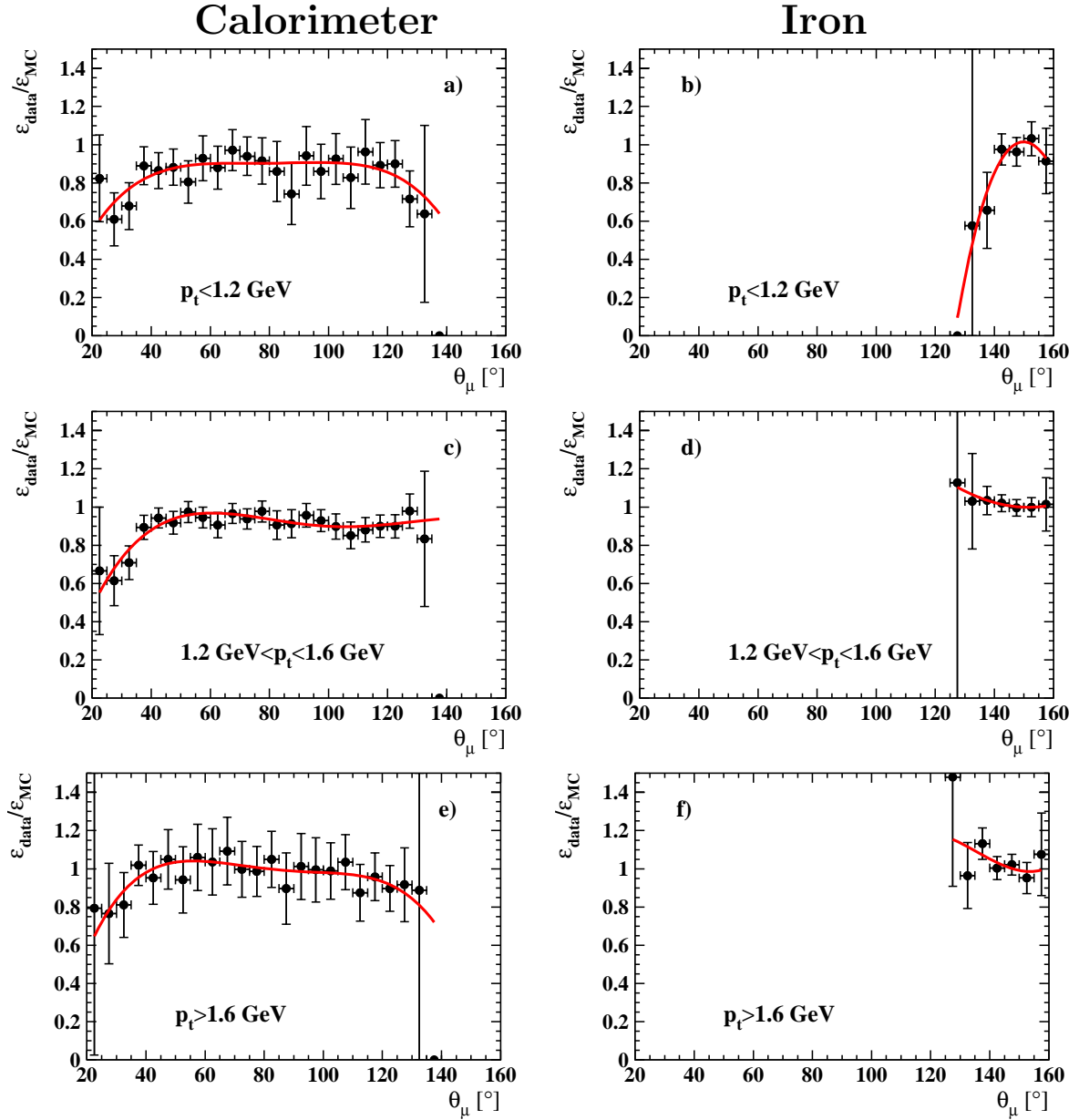
Figure 4.7: Ratio of the muon identification efficiency in data and MC simulation in the calorimeter (a,c,e) and in the iron (b,d,f) as a function of θ in three bins of p_t.

correction has to take into account that only one muon is required to be identified as a muon in the present analysis and will be derived in the following.

Let p_i and $\tilde{p}_i$ be the probability to identify the ith track as a muon in data and MC simulation respectively and let f_i be the correction as explained above.

$$p_i = f_i \, \tilde{p}_i. \tag{4.4}$$

The correction factor $f_{1\bar{2}\|\bar{1}2}$ is needed for the case that only one of the two identified muons is required to be identified [1]. The following relation holds for the probabilities p and $\tilde{p}$:

$$
\begin{aligned}
p_{1\bar{2}\|\bar{1}2} &= p_1(1-p_2) + (1-p_1)p_2 + p_1 p_2 \\
&= p_1 + p_2 - p_1 p_2
\end{aligned}
$$

The correction factor for events with two identified muons under the condition that only one muon is required to be identified is given by

$$
\begin{aligned}
f_{1\bar{2}\|\bar{1}2} &= \frac{p_{1\bar{2}\|\bar{1}2}}{\tilde{p}_{1\bar{2}\|\bar{1}2}} \tag{4.5} \\
&= \frac{p_1 + p_2 - p_1 p_2}{\tilde{p}_1 + \tilde{p}_2 - \tilde{p}_1 \tilde{p}_2} \\
&= \frac{f_1 \, \tilde{p}_1 + f_2 \, \tilde{p}_2 - f_{12} \, \tilde{p}_1 \tilde{p}_2}{\tilde{p}_1 + \tilde{p}_2 - \tilde{p}_1 \tilde{p}_2} \tag{4.6}
\end{aligned}
$$

with

$$f_{12} = f_1 \, f_2.$$

The efficiency of the corrected MC simulation is also shown in figure 4.6.

4.6.2 Triggers

A similar data sample as in the previous section is used to analyse the trigger efficiency in data and in the MC simulation. Now the standard cuts on the muon identification (see section 3.2.2) are applied and the simulation is corrected for the muon identification efficiency. Independent subtriggers are used to obtain an unbiased determination of the trigger efficiencies. Due to the limited statistics of such event samples the checks are not done for the complete subtriggers, but for the trigger elements, which the subtriggers consist of (see section 2.2.6). The simulation of each individual trigger element is compared to the data and corrected if necessary. In the case of the trigger elements used in the photoproduction analysis the correction is applied as a function of θ, while the DIS trigger

---

[1] The subscript $1\bar{2}\|\bar{1}2$ does not mean that only one track is identified as a muon. In fact both tracks are identified as a muon, but only one identified muon is required.

elements are corrected as a function of Q^2. The correction factors are determined as for the muon identification efficiency using the ratio between the efficiencies in data and MC simulation.

Figure 4.8 shows the efficiency of the trigger elements as a function of W and Q^2. All but the last tow histograms show the efficiencies of L1 trigger elements. The events triggered by the subtriggers *s15* and *s54* are verified by neural net triggers on L2, which are shown in the last two histograms. The efficiencies of the L4 conditions have been monitored during the data taking and found to be above 98%. In addition, all subtriggers use veto conditions to reduce non-*ep* background. Their efficiencies are above 99% and their inefficiency can be neglected in comparison to the L1 trigger elements [75].

Beside the corrections for each trigger element, the L1 subtriggers must be corrected for the prescale factors [92] used during the data taking (see section 2.2.6). The probability that subtrigger i triggers the event j in run k is given by

$$P_{ijk} = \frac{r_{ij}}{d_{ik}}$$

where $r_{ij} \in \{0, 1\}$ is the raw L1 bit of subtrigger i in event number j and d_{ik} is the downscaling factor of subtrigger i in run k. The probability that at least one of N subtriggers triggers the event j in run k is

$$P_{jk} = 1 - \prod_i^N \left(1 - \frac{r_{ij}}{d_{ik}}\right)$$

The weight to be assigned to the event j in run k is

$$w_{jk} = \frac{1}{P_{jk}}$$

The final weight of a subtrigger used in the analysis is averaged over the full run range

$$w_j = \frac{\sum_{k=1}^N \int \mathcal{L}_k}{\sum_{k=1}^N \int \mathcal{L}_k P_{jk}} \tag{4.7}$$

where $\int \mathcal{L}_k$ is the integrated luminosity of run k. The weights are determined for each combination of all used subtriggers (see table'4.1) and applied as a scaling factor $1/w_j$ to the simulated events.

	s15	s54	s15‖s54	s56	s61	s56‖s61
1999 e^-	1.019	1.412	1.010	1.000	1.031	1.000
1999 e^+	1.003	1.340	1.002	1.000	1.036	1.000
2000 e^+	1.046	1.182	1.031	1.000	1.188	1.000

Table 4.1: Event weights calculated using equation (4.7).

Figure 4.9 shows the final comparison of the efficiencies of the simulated subtriggers compared to the data. A good overall agreement can be seen. The trigger description is checked again in figure 4.10. Here the ratio of the cross section determined using a single subtrigger and the cross section calculated using both subtriggers as a function of W and t is shown.
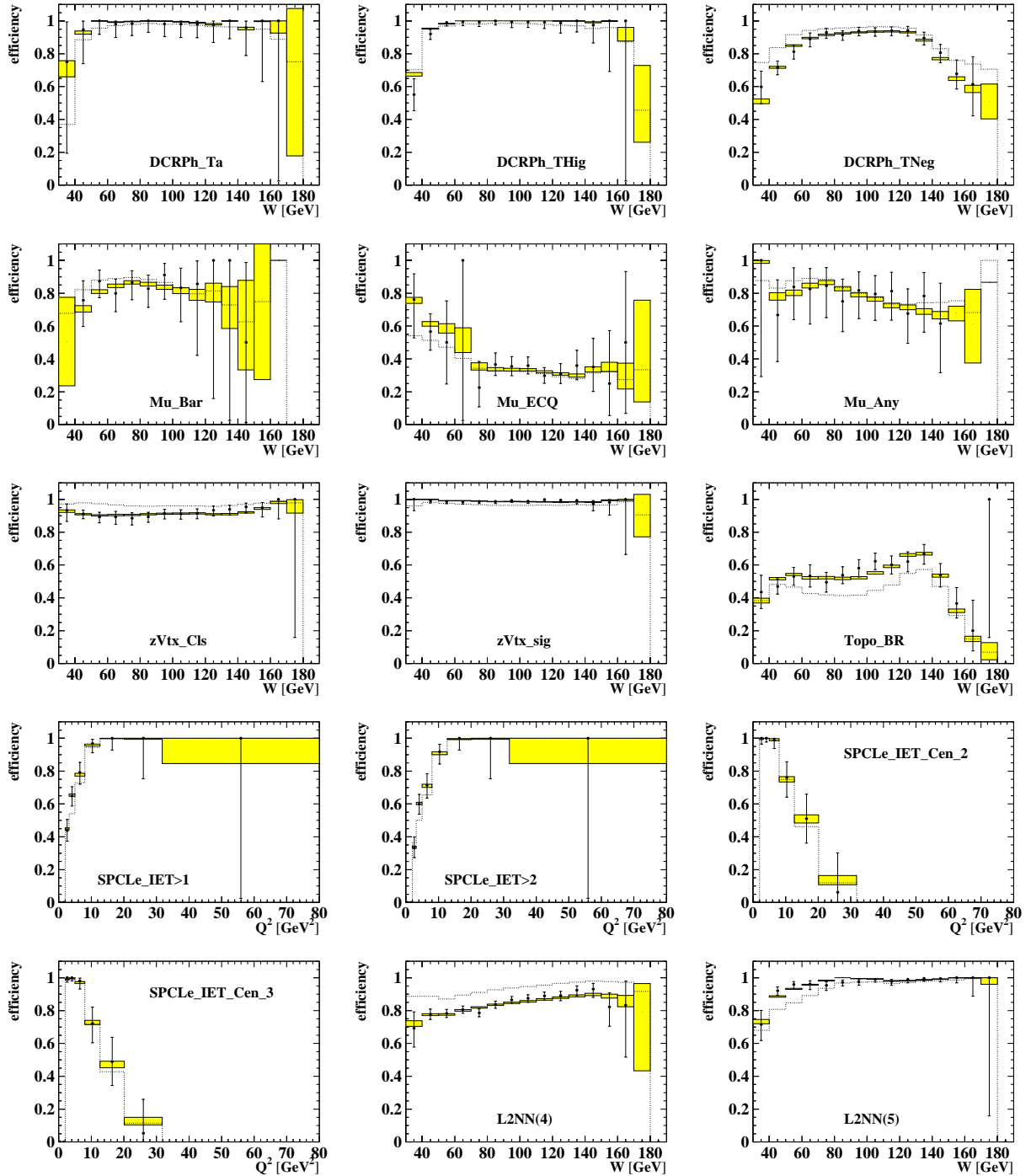
Figure 4.8: Efficiencies of L1 trigger elements as a function of W. In the analysis only the range $40\,\text{GeV} < W < 160\,\text{GeV}$ is used. For the SpaCal trigger elements the efficiencies are shown as a function of Q^2. The efficiencies in data (points) are compared to those in the uncorrected simulation (dotted histograms). Where necessary corrections are applied to the simulation (shaded error boxes).
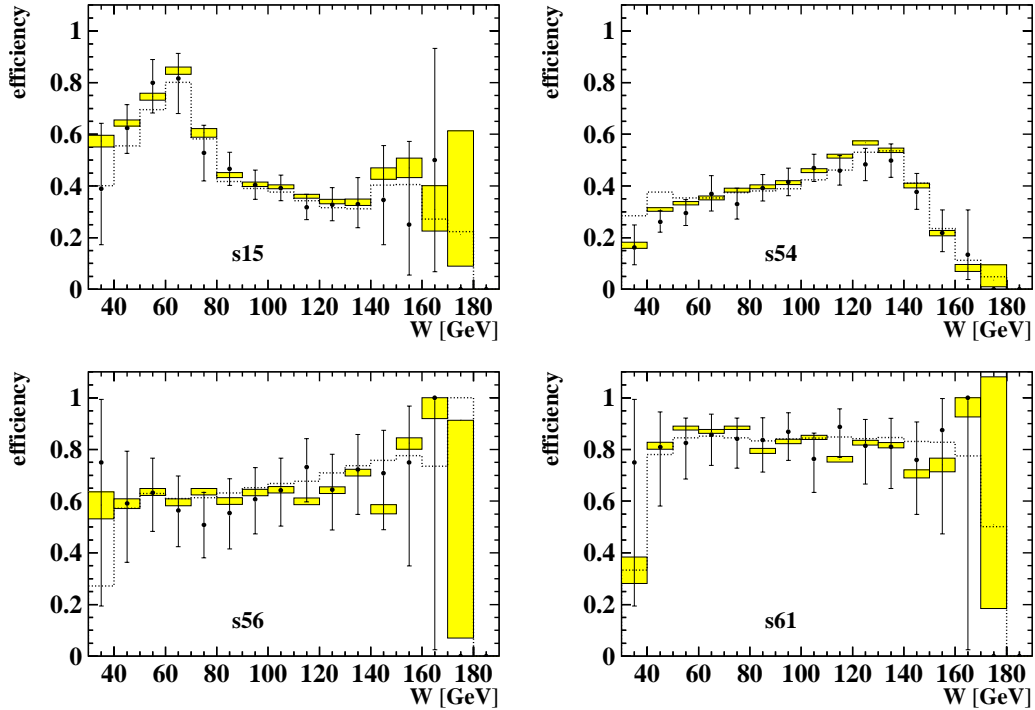
Figure 4.9: Efficiencies of the subtriggers as a function of θ. The efficiencies in data (points) are compared to those in the corrected simulation (shaded error boxes). The efficiency of the uncorrected MC is also included (dotted line). To increase the statistics a data sample is used, which is not independent of the subtriggers. Therefore this comparison is only used as a rough estimation. The correction factors for the simulation are determined for each individual trigger element.
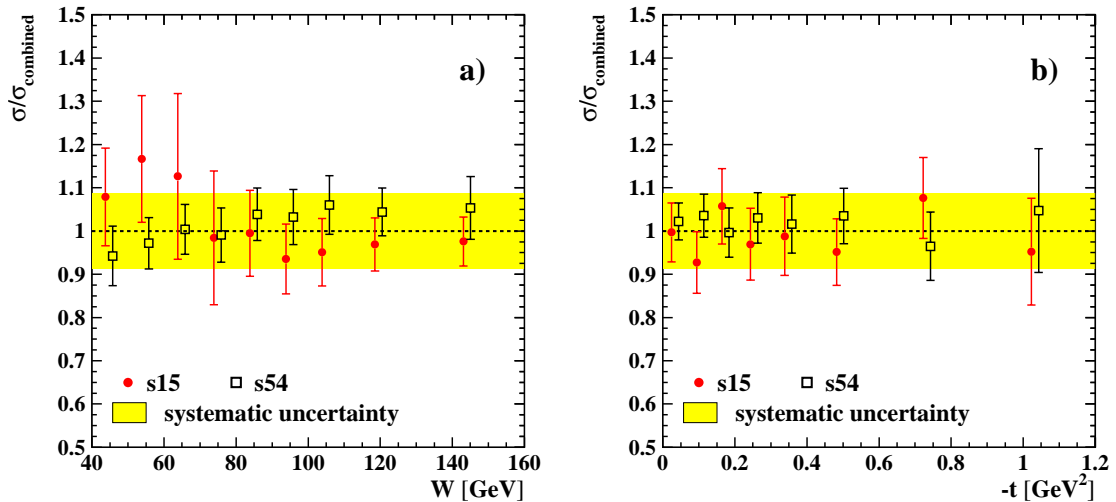
Figure 4.10: Comparison of the photoproduction cross sections for the year 2000 as derived using subtrigger *s15* or *s54* only. a) shows the ratio of the cross section and the combined cross section using both subtriggers as a function of W, while b) shows the ratio as a function of t. The shaded band shows the systematic uncertainties as discussed in section 4.9. In both figures the data points are slightly shifted along the x-axis to make all data points visible.

4.6.3 Forward Tagging

Another important check of the simulation concerns the description of the forward detectors. The data sample used to do this comparison is based on the one used in the previous section. In addition the standard trigger selection is added and the corrections applied to the simulation.

Figure 4.11 a) shows the energy deposition in the forward section of the LAr calorimeter. A systematic shift towards higher values of E_{LAr10} can be seen in the uncorrected simulation. Therefore a polynomial is fitted to the ratio of the distribution in the data and the MC simulation, which is then used as correction function. The corrected simulation is also shown in the figure.
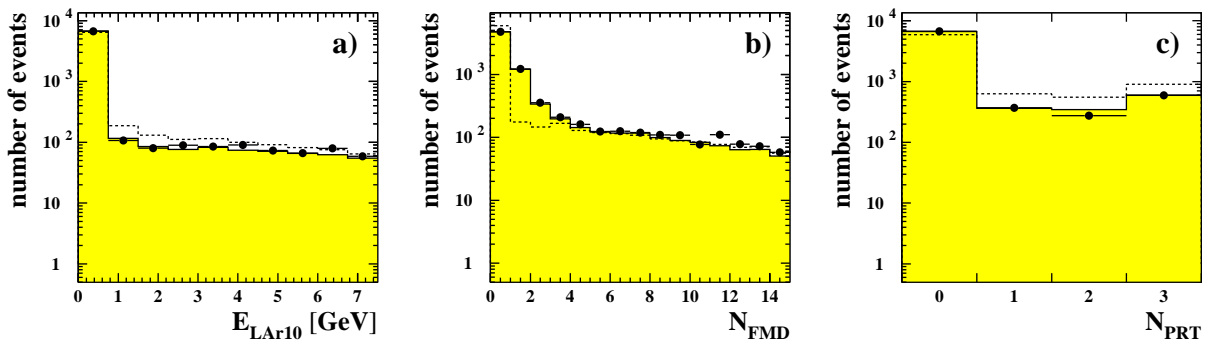
Figure 4.11: a) Energy deposition in the forward section of the calorimeter. The data (points) are compared to the uncorrected simulation (dashed histogram). To get a better description corrections have been applied (solid histogram). b) Number of hits in the Forward Muon Detector. Electronic noise is not contained in the simulation and added using equation 4.8. c) Number of hits in the first three scintillators of the Proton Remnant Tagger.

The second variable used in the forward selection is the number of hits in the pre-toroid layers of the Forward Muon Detector N_{FMD}. Here electronic noise is not included in the simulation and is added as follows. A constant probability p is assumed to get one additional hit. There can be fluctuations into the bin i with the bin content N_i from all bins $j < i$. On the other hand there can be fluctuations out of bin i into each bin $k > i$. The probability p is extracted from a fit to the data yielding a value of $p = 18.6\%$. The corrected number $\tilde{N}_i$ of events with i hits in the Forward Muon Detector is then given by

$$\tilde{N}_i = \sum_{j=1}^{i-1} p^{i-j} N_j + N_i - \sum_{k=i+1}^{\infty} p^{k-i} N_i. \tag{4.8}$$

Taking the final cut $N_{\mathrm{FMD}} \leq 1$ into account this corresponds to an effective noise level of 5%, which is in agreement with results in a previous analysis [77]. The noise corrected distribution in the simulation is in a second step compared to the data and a correction function is derived as for the energy deposition E_{LAr10}. The results are shown in figure 4.11 b).

Finally a correction for the number of hits in the first three scintillators of the Proton Remnant Tagger N_{PRT} is determined in an analogous way. The result is shown in figure 4.11 c).

An overview of the description of the forward selection is given by figure 4.12 for the full kinematic region. It has been verified that the quality of the description of the forward detectors does not have a strong dependence on W, t or Q^2.
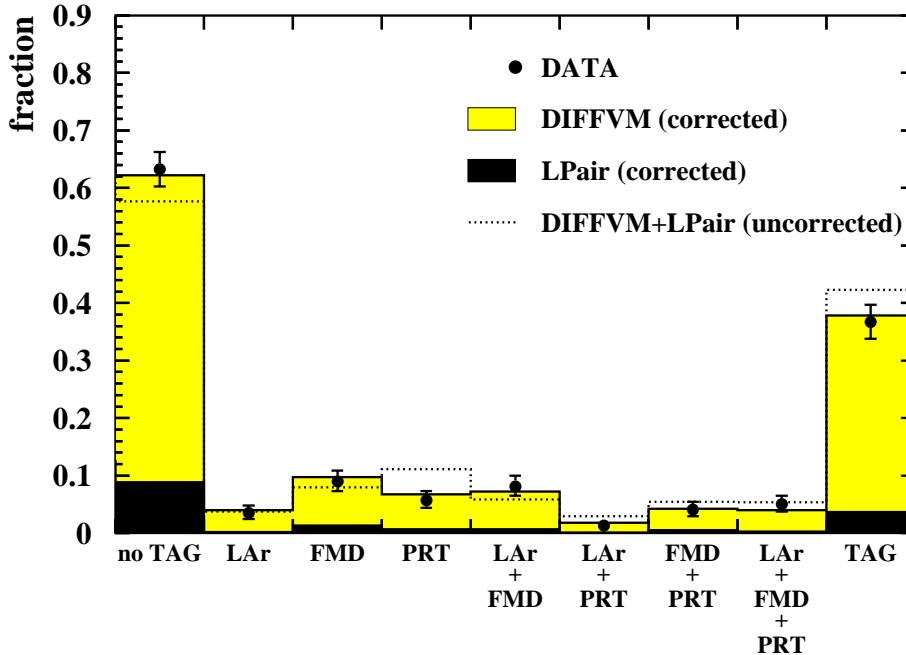
Figure 4.12: Overview of the forward selection for the J/ψ photoproduction. Shown is the fraction of events which are not tagged (no TAG) and which are tagged by the counters as indicated. The '+' indicates a logical AND. The last bin shows the fraction of all tagged events. The data (points) are compared to the sum of the corrected DIFFVM simulation (light shaded histogram) and the LPAIR simulation (dark shaded histogram). In addition the uncorrected simulation is shown (dotted histogram).

After correcting the description of the forward detectors the number of elastic events can be calculated from the number of events with and without a forward tag. Two different ways are used which also serve as control for each other.

In the first method the number of events is extracted from the MC simulation. This is model dependent, because it uses the unknown ratio of σ_{el}/σ_{pd}. In previous analyses [75, 77] it has been shown that an equal number of generated events N_{el} and N_{pd} gives best results. The second method uses the linear equations

$$\begin{pmatrix} N_{\mathrm{no\ tag}} \\ N_{\mathrm{tag}} \end{pmatrix} = \begin{pmatrix} \epsilon^{\mathrm{el}}_{\mathrm{no\ tag}} & \epsilon^{\mathrm{pd}}_{\mathrm{no\ tag}} \\ \epsilon^{\mathrm{el}}_{\mathrm{tag}} & \epsilon^{\mathrm{pd}}_{\mathrm{tag}} \end{pmatrix} \cdot \begin{pmatrix} N_{\mathrm{el}} \\ N_{\mathrm{pd}} \end{pmatrix}$$

where ϵ^i_j denotes the fraction of elastic or proton dissociative events in the sample of tagged or untagged events. The values for ϵ^i_j are taken from the MC simulation. This

way does not depend on the ratio of the cross sections for elastic and proton dissociative events. The factors ϵ_j^i already include the detector efficiencies. This has to be taken into account in equation (4.1).

In this analysis the first method is used as default. However, the ratio $\sigma_{el}/\sigma_{pd} \approx 1$ is verified using the second method. A comparison of the results can be seen in figure 4.13.
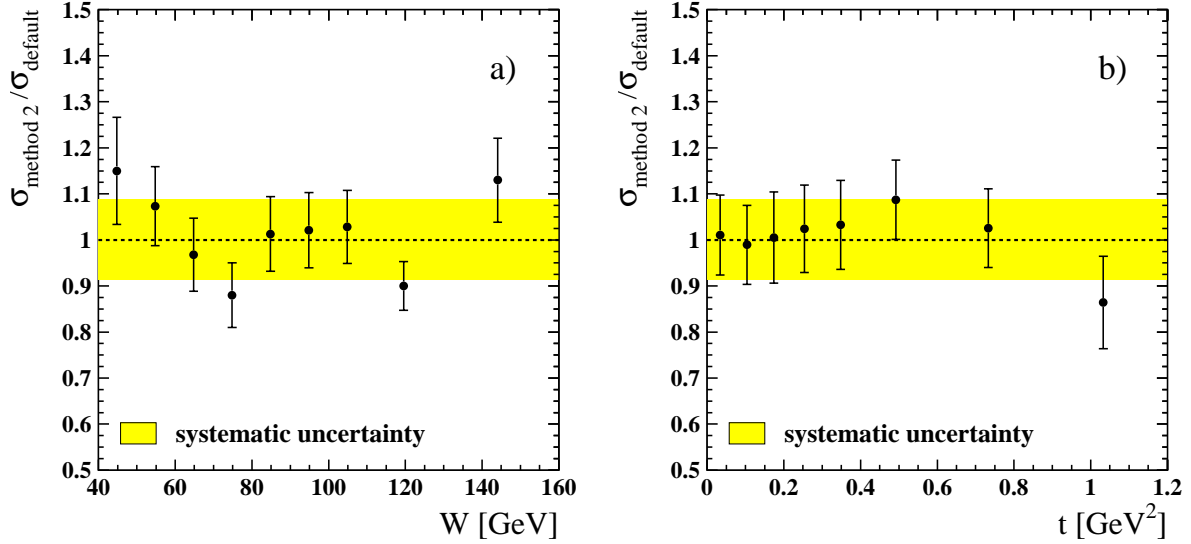
Figure 4.13: Comparison of the photoproduction cross sections for the two different methods used to derive the number of elastic events from the number of events with and without forward tag. a) shows the ratio of the two results as a function of W, while b) shows the ratio as a function of t. The shaded band shows the systematic uncertainties as discussed in section 4.9.

4.7 Comparison of Data and corrected MC

Figure 4.14 shows the distribution of the correction factors for all MC events after correcting the simulation for the muon identification, triggers and forward counters as described in section 4.6. Now a final comparison of data and simulation is performed. The distribution of variables used to analyse the cross section are well described by the simulation as seen in figure 4.15 for the regime of photoproduction for the combined data taking periods. In figure 4.16 distributions for the decay muons and the J/ψ meson are shown.

Figure 4.17 and 4.18 show the corresponding comparisons for the same variables and in addition for Q^2 and Ψ in deep inelastic scattering. A comparison for distributions of the scattered positron can be seen in the figures 3.7 and 3.8 in the previous chapter (page 35 and 36). A good overall agreement between data and MC simulation is obtained.
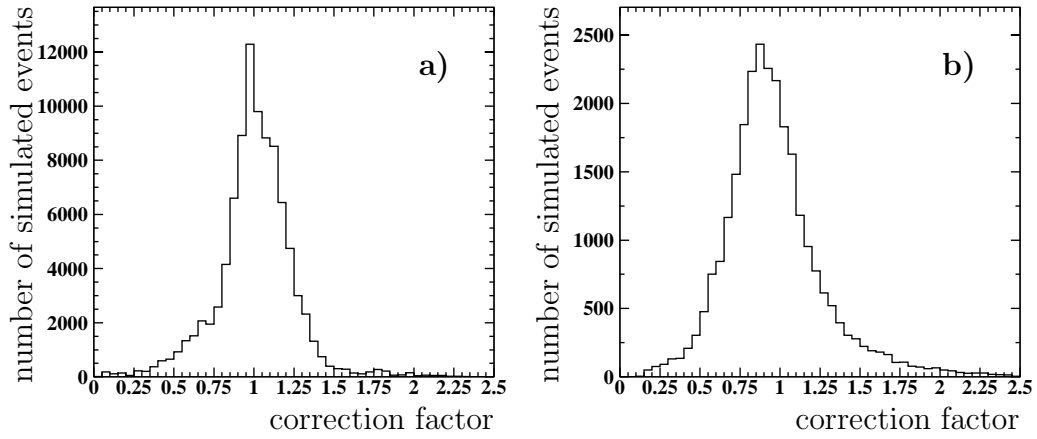
Figure 4.14: Distribution of the correction factors applied to the MC simulation for a) photoproduction and b) deep inelastic scattering.
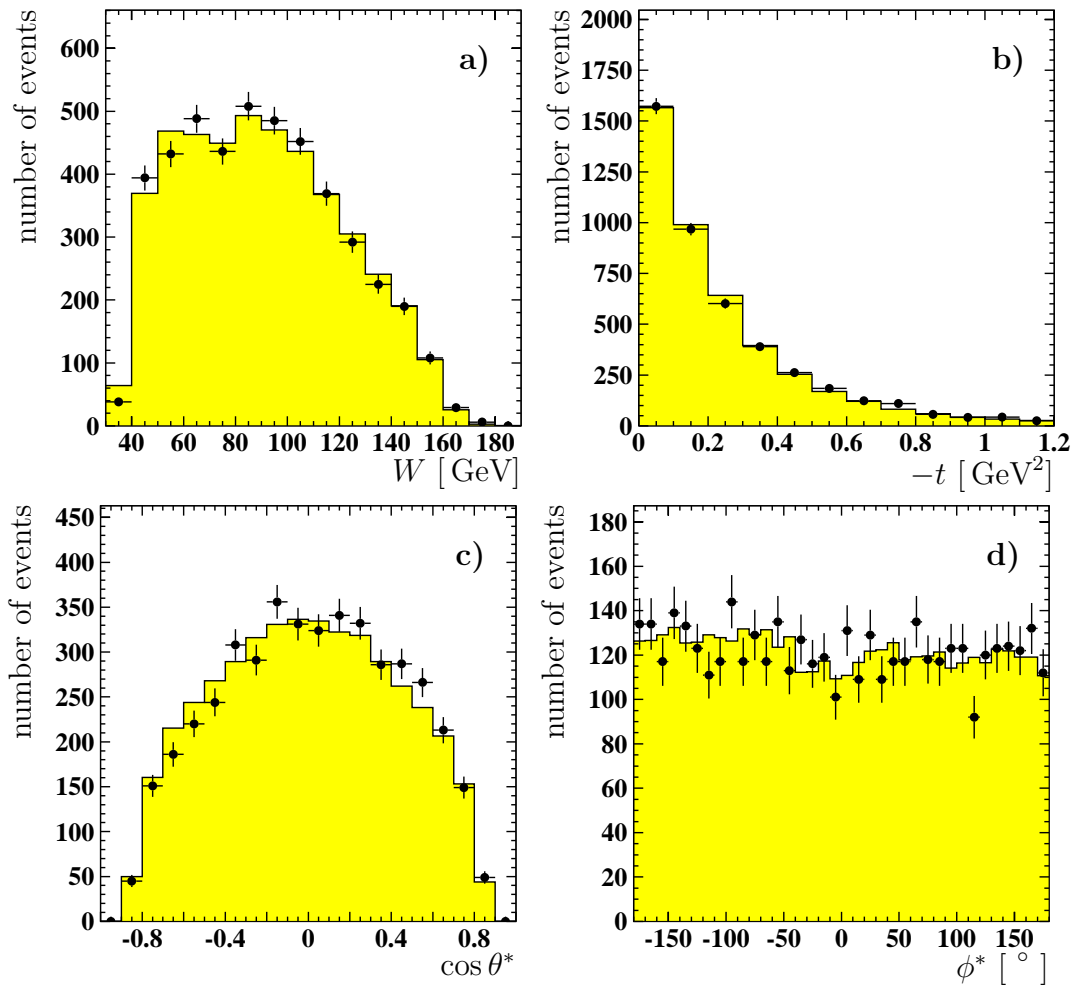
Figure 4.15: Comparison of distributions in data (points) and MC (shaded histograms) used to calculate the cross section in the regime of **photoproduction**. A good overall agreement can be seen.
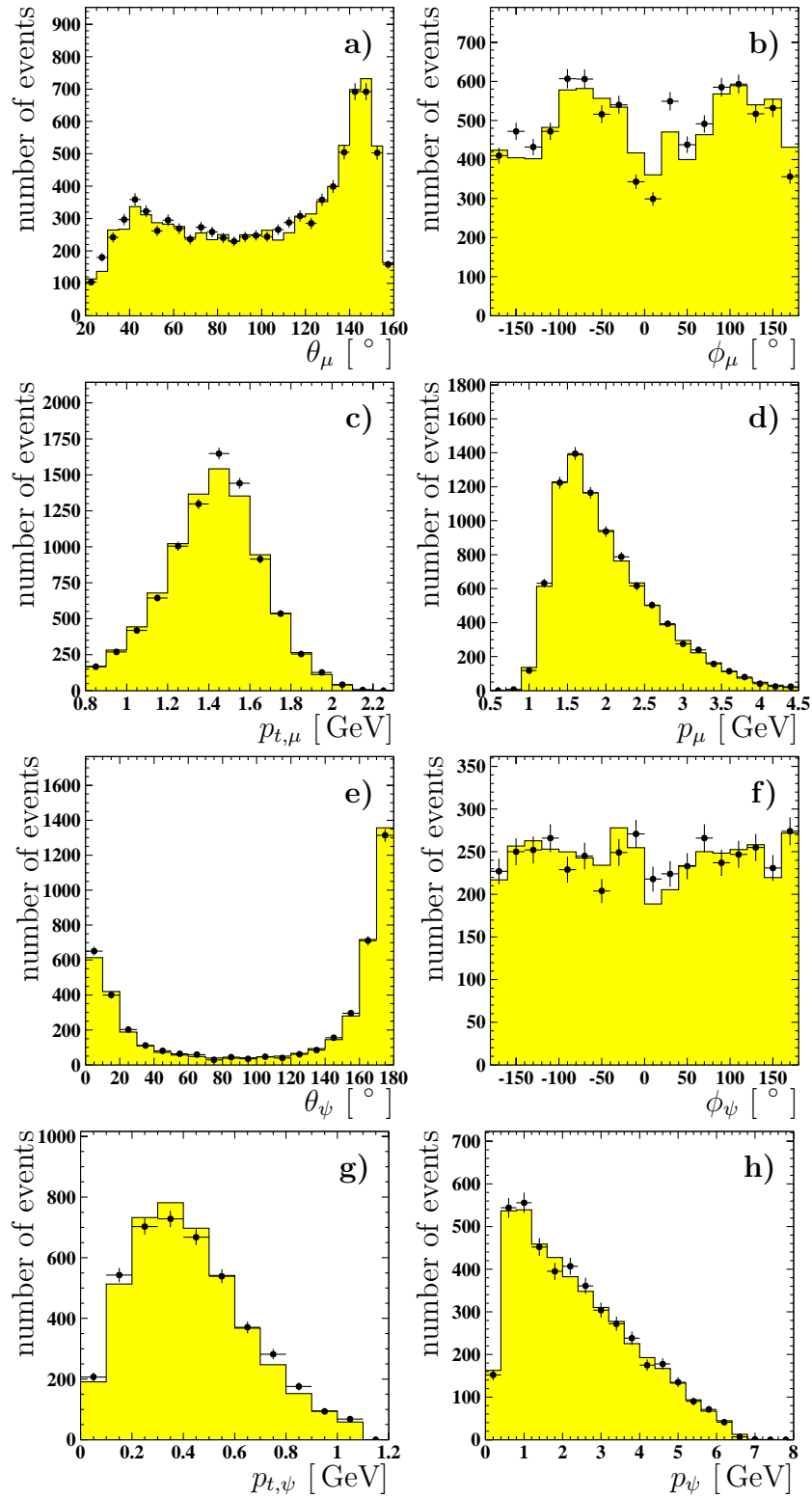
Figure 4.16: Comparison of decay muon (a-d) and J/ψ meson (e-h) distributions in data (points) and MC (shaded histograms) in **photoproduction**.
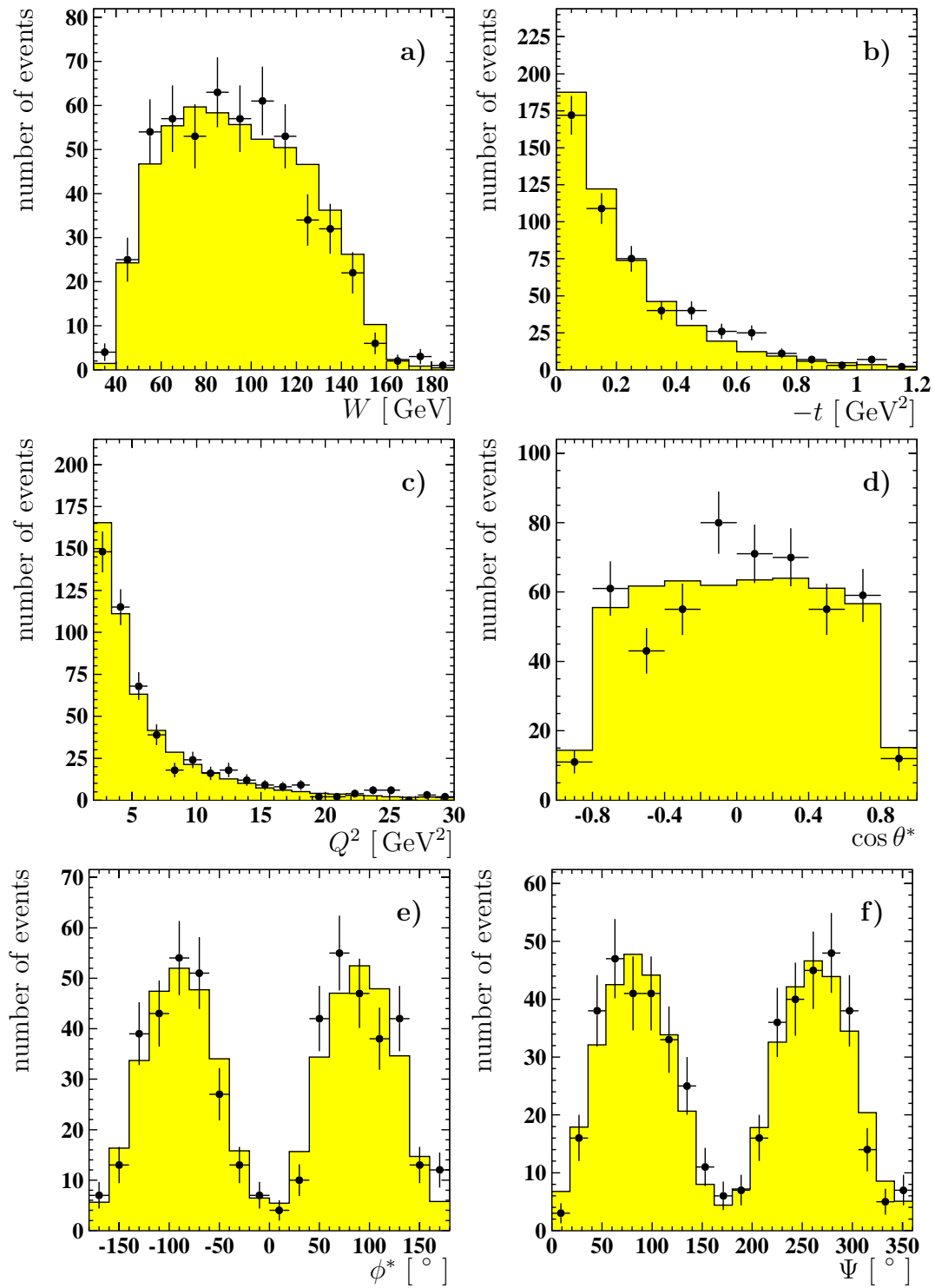
Figure 4.17: Comparison of distributions in data (points) and MC (shaded histograms) used to calculate the cross section in the regime of **deep inelastic scattering**. A good overall agreement can be seen.
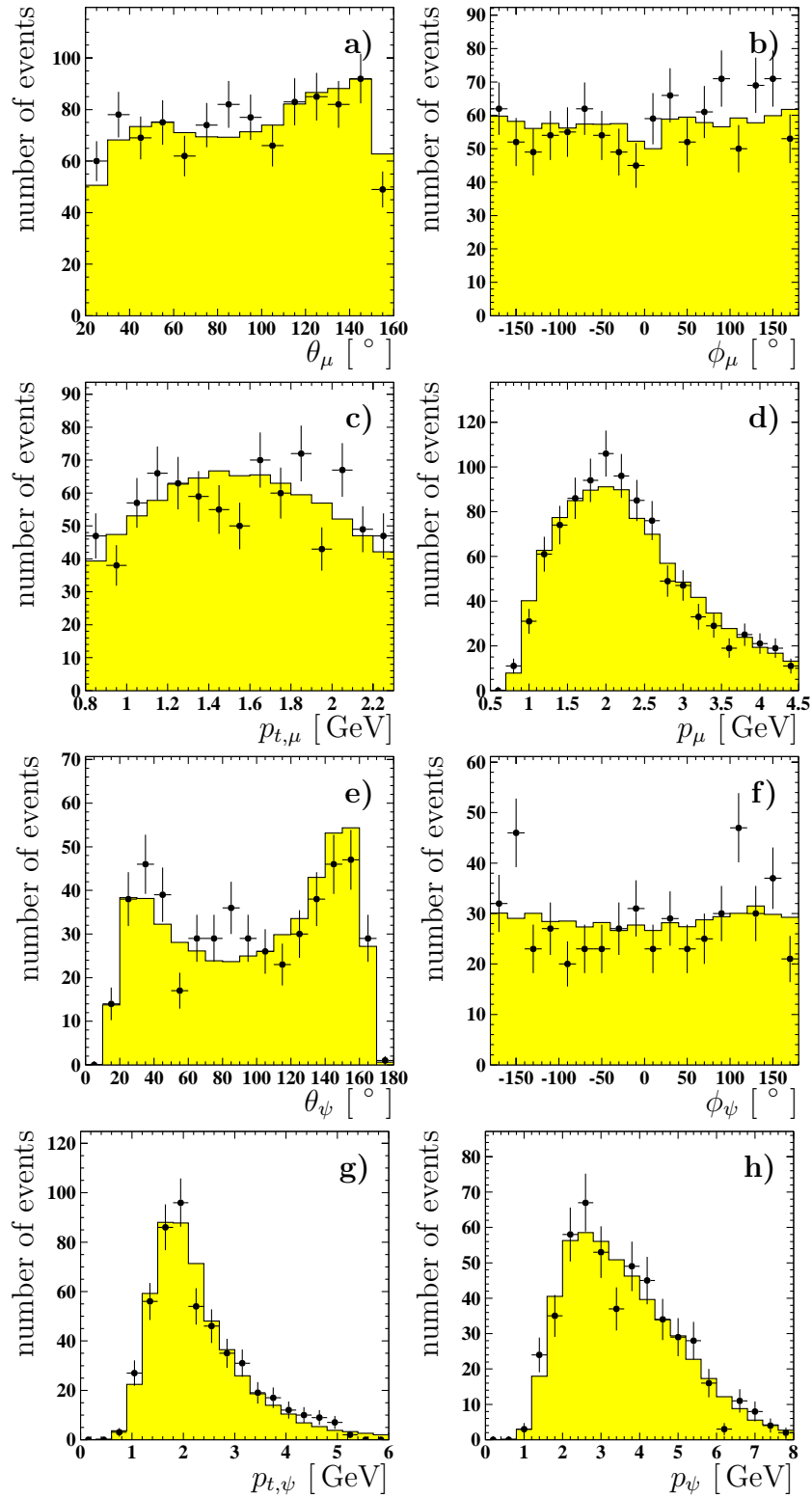
Figure 4.18: Comparison of decay muon (a-d) and J/ψ meson (e-h) distributions in data (points) and MC (shaded histograms) in **deep inelastic scattering**.

4.8 Total Efficiencies

After having checked that the MC simulation is able to describe the data it is used to determine the selection efficiency and geometrical acceptance. They are needed for the calculation of the cross section (see section 4.1). Figure 4.19 shows the total efficiency ϵ_{tot} together with the selection efficiency ϵ_{sel} and the trigger efficiency ϵ_{tri} as well as the geometrical acceptance ϵ_{acc} for the year 2000. The efficiencies are shown as functions of the kinematic variables W, t and Q^2 separately for photoproduction and deep inelastic scattering. The total efficiencies are defined such that:

$$\epsilon_{tot} = \epsilon_{acc} \cdot \epsilon_{sel} \cdot \epsilon_{tri}.$$

The geometrical acceptance describes the probability that both decay muon tracks are produced within the polar angular range $20° < \theta < 160°$. Due to the fact that the polar angle θ of the decay leptons is related to the centre-of-mass energy W, the geometrical acceptance decreases towards lower and higher values of W. The W range in the analysis is restricted to a region where $\epsilon_{acc} \gtrsim 40\%$. The selection efficiency shows the effect of the selection cuts discussed in chapter 3. The trigger efficiency is shown separately. The total efficiency describes the loss of events due to the detector, selection and trigger criteria.

The shape of the total efficiency as a function of W is dominated by the geometrical acceptance. The region of reduced selection efficiency in the photoproduction sample is due to the cuts against cosmic ray background (section 3.3.2). In the DIS sample the trigger efficiency is twice as high as in the case of photoproduction and shows almost no dependence on the kinematic variables.

In addition to the total efficiency a correction factor $(1 - f_{pd})$ is applied to the number of events, derived from the MC simulation. This correction accounts for events with proton dissociation left in the final data sample. Figure 4.20 shows the correction as a function of the kinematic variables W, t and Q^2 for the year 2000.

All steps in the analysis are done for each data taking period separately. To verify that the individual results are in agreement with each other, figures 4.21 and 4.22 show the ratio of the elastic cross sections derived for each period to the combined result. Within the errors all results are compatible with each other. The combined values are derived by calculating the mean value of the luminosity weighted individual cross sections.
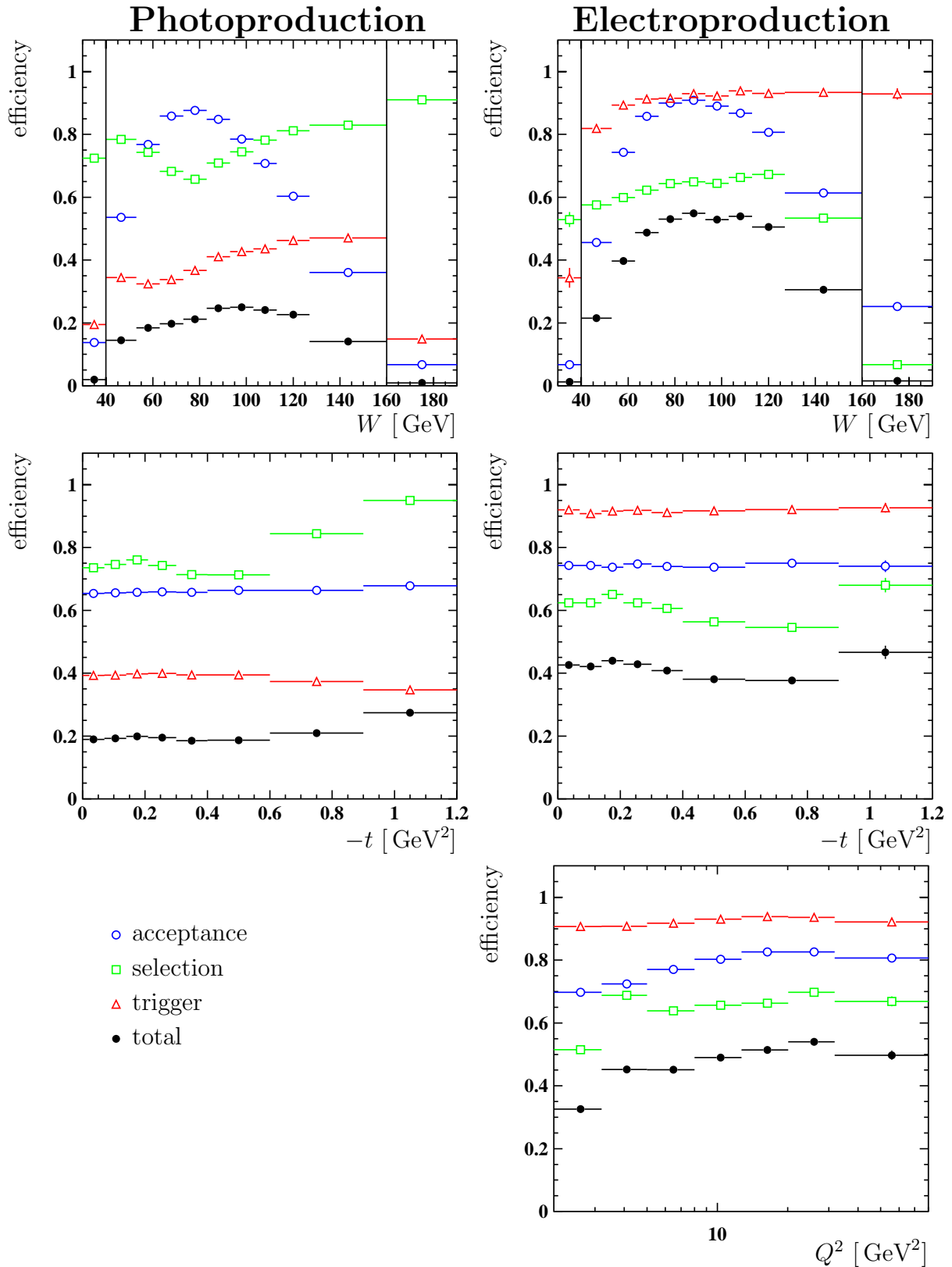
Figure 4.19: Total efficiency of the year 2000 as a function of W, t and Q^2. The left column shows the results for the photoproduction and the right column for the regime of deep inelastic scattering. In W only the range $40\,\text{GeV} < W < 160\,\text{GeV}$ is used for the final results. This cut is already applied for the efficiencies in t and Q^2.
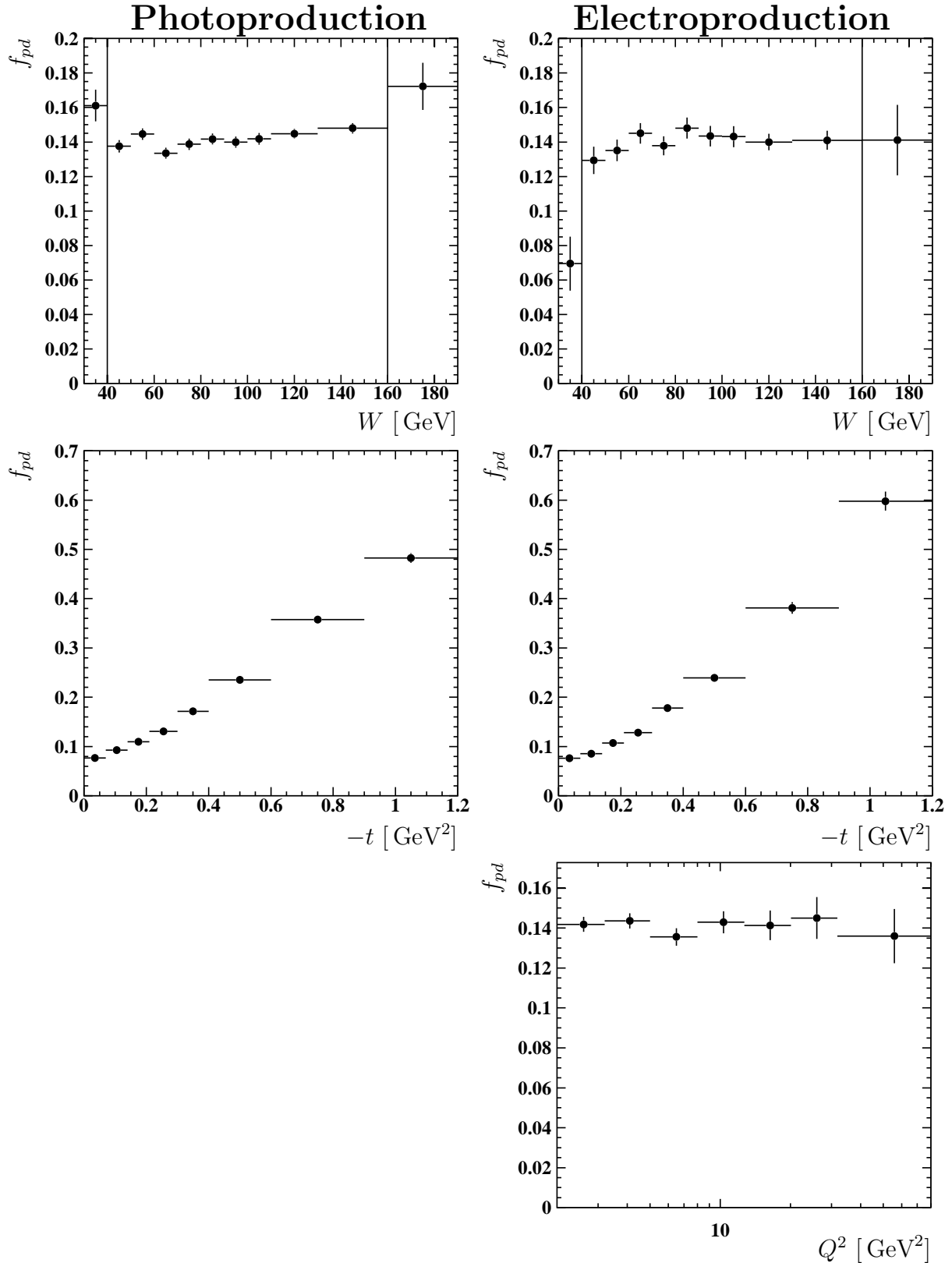
Figure 4.20: Correction factor f_{pd} as a function of W, t and Q^2 for the year 2000. The left column shows the results for the photoproduction and the right column for the regime of deep inelastic scattering. In W only the range $40\,\text{GeV} < W < 160\,\text{GeV}$ is used for the final results. This cut is already applied for the efficiencies in t and Q^2.
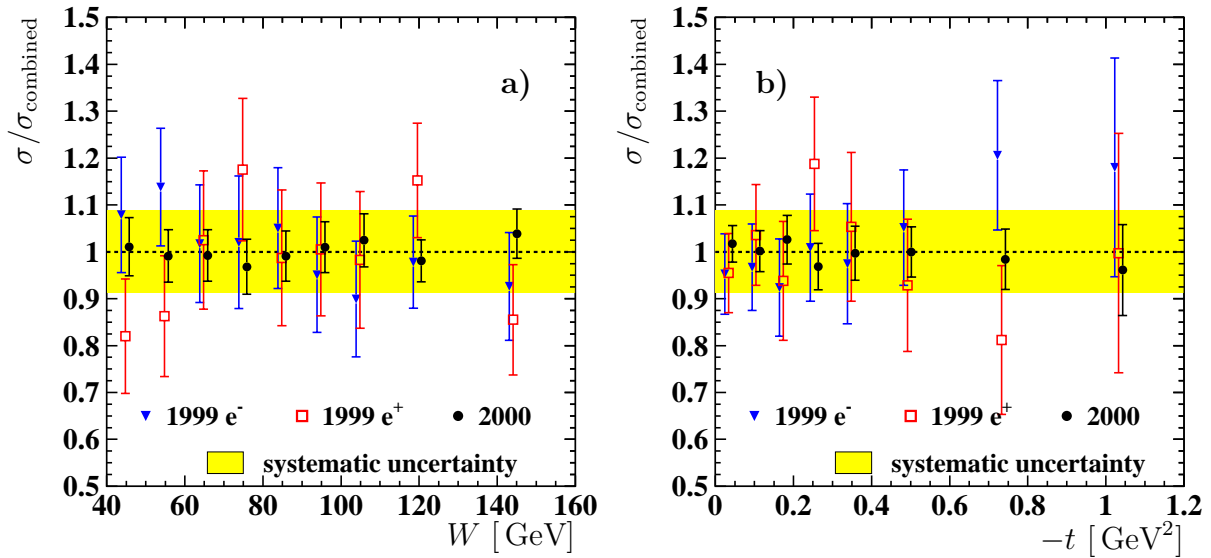
Figure 4.21: Comparison of the **photoproduction** cross sections for the individual data taking periods. a) shows the ratio of the cross section derived in a given period to the combined cross section as a function of W, while b) shows the ratio as a function of t. In both figures the data points are slightly shifted along the x-axis to make all data points visible.
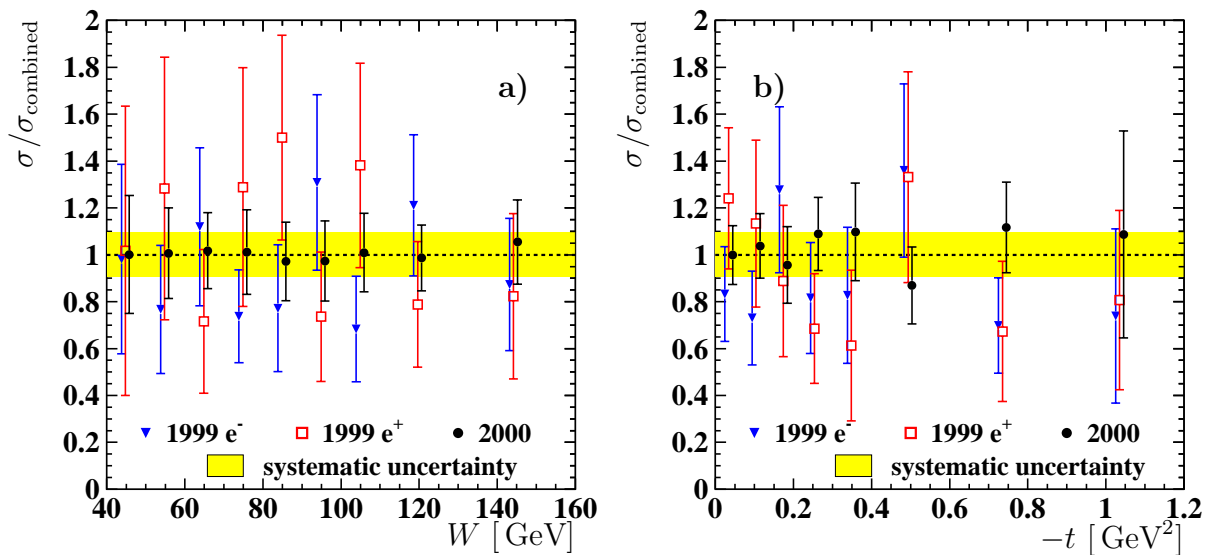
Figure 4.22: Comparison of the **DIS** cross sections for the individual data taking periods. a) shows the ratio of the cross section derived in a given period to the combined cross section as a function of W, while b) shows the ratio as a function of t. In both figures the data points are slightly shifted along the x-axis to make all data points visible.

4.9 Systematic Uncertainties

In this section the determination of the systematic uncertainties is described. Table 4.2 shows an overview of the different sources and the corresponding mean values used in this analysis. To derive the total systematic uncertainties all contributions are added in quadrature.

source	amount [%]	correlated [%]
track reconstruction	4	
z_{vtx} distribution	1	
muon identification	1.5	0.5
trigger efficiencies	5	
el / pd separation	5	2
number of signal event determination	1	
$\psi(2S)$ background	0.5	
J/ψ branching ratio	1.7	1.7
luminosity	1.4	1.4
e' description (DIS only)	4	
total systematic uncertainty (PhP)	8.8	3.0
total systematic uncertainty (DIS)	9.6	3.0

Table 4.2: Mean values of the systematic uncertainties taken into account for the cross section measurement. Some of the uncertainties are assumed to be correlated leading to a global normalisation uncertainty. For the determination of the W and t dependence of the cross sections only the uncorrelated systematic uncertainties are taken into account.

The uncertainty on the track reconstruction efficiency has been analysed in [76, 109] and estimated to be 4% for two tracks. The z position of the vertex z_{vtx} is not simulated correctly, as shown in figure 4.23. To evaluate the effect on the cross section a correction is applied to the MC simulation, shifting the peak position. This affects the cross section measurement as a function of W by 1%. No effect can be seen as a function of t, Q^2 or the decay angles.

The uncertainty on the muon identification efficiency is determined as follows. After the correction of the MC simulation as described in section 4.6.1 the largest difference between the data and MC simulation in the bins of θ and p_t is found to be $\Delta\epsilon/\epsilon = 4\%$. In a second step the whole analysis is repeated twice using a correction function for the muon identification shifted by this amount downwards and then shifted by this amount upwards. An effect of 1.5% on the cross section is seen, independent of any variable, and is slightly lower for the data taking period of the year 2000.

A large contribution to the total systematic uncertainty comes from the determination of the trigger efficiencies. Due to the lack of an independent trigger setup, which triggers a similar kinematic region, the efficiencies are determined in an the way described in section 4.6.2. The uncertainty is estimated as follows. For each trigger element the efficiency
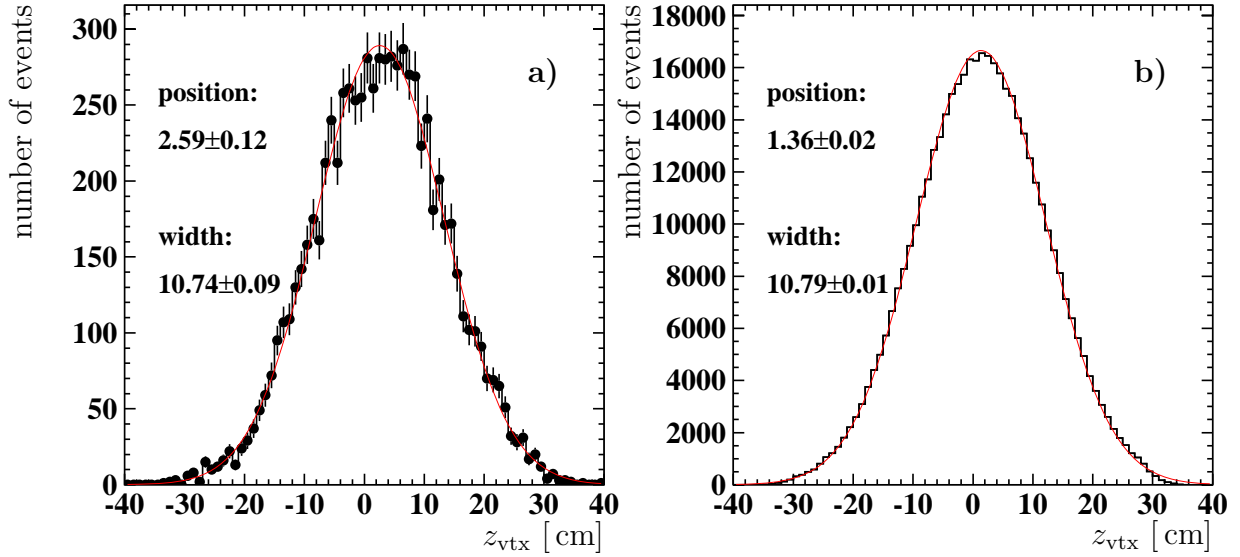
Figure 4.23: z_{vtx} position in a) data and b) MC simulation. A shift toward lower values is seen in the MC simulation. The effect on the cross section as a function of W is determined to be 1%.

is determined in data and MC as a function of W. Then the largest difference is taken to be the uncertainty for this trigger element. Finally the individual uncertainties for each trigger element are added in quadrature. For the subtriggers used in the photoproduction analysis the systematic error is estimated to be 2.5% for *s15* and 4.0% for *s54* (where the trigger element Topo_BR has the largest contribution). For the subtriggers used in the DIS sample the uncertainty is determined to be 3.0% for *s56* and 4.1% for *s61*. A change in the trigger efficiency has an effect on the W distribution, but no systematic change of the slope is observed. Therefore a global uncertainty of 5% is taken into account for the cross section determination.

The uncertainty on the separation of elastic events and events with proton dissociation consists of two components. The first part corresponds to the description of the forward detectors in the simulation. After the correction of the MC according to section 4.6.3 the largest difference (6%) between the data and simulation in the contribution of untagged events is determined in bins of W, t and Q^2. Now the analysis is repeated shifting the correction functions. The effect on the cross section is determined to be 4.5% showing a small W dependence (the uncertainty is increasing with W). The second contribution to the uncertainty is the extraction of the number of elastic and proton dissociative events from the number of tagged and untagged events (section 4.6.3). The cross section is calculated using the two different methods and the mean difference between both methods is found to be 2%. These two contributions are partially correlated. Therefore the quoted 5% error for the separation of elastic and proton dissociative events is conservative.

The systematic uncertainty of the procedure used to extract the number of signal events is determined as follows. The function used to describe the non-resonant background is changed from a power law to an exponential. In a second step the bins of the mass distribution are shifted. As a third check only the non-resonant background is fitted, while the number of signal events is determined by counting the events in the mass window of

$\pm 150\,\text{MeV}$ around the peak position. Figure 4.24 shows as an example the results of the different methods for the total photoproduction data sample. The mean difference between those methods is determined in each analysis bin and found to be less than 1%. With increasing values of Q^2 the quality of the fits decreases and the differences increase. At the same time the number of background events seen outside the mass window is decreasing. In these bins the number of signal events is determined without fits (section 4.5) and a global uncertainty of 1% is used.

The $\psi(2S)$ background is described in section 3.3, while the uncertainty on the J/ψ branching ratio is taken from [3]. The information on the luminosity is taken from [102] and summarised in table 3.1.

In the case of deep inelastic scattering an additional source of systematic uncertainty comes into play. Here the kinematic variables are reconstructed using the properties of the scattered positron. Therefore a good description of the scattered positron in the MC simulation is essential. An overall agreement can be seen in the figures 3.7 and 3.8 for the description of the scattered positron as well as for the other distributions shown in the figures 4.17 and 4.18. The statistics is much lower than in the regime of photoproduction, but also the discrepancies are somewhat larger. To get an estimate of the systematic uncertainty the mean difference between data and MC simulation is used. Therefore an additional global uncertainty of 4% is added.

In both kinematic regions some of the systematic uncertainties are correlated. These correlated uncertainties do not affect the dependences of the measured cross sections, but lead to global normalisation uncertainties. Therefore these errors are not taken into account when determining the slope parameters δ or b using $\sigma \propto W^\delta$ and $d\sigma/dt \propto e^{bt}$. Correlated quantities are the uncertainties on the luminosity as well as on the J/ψ branching ratio. In addition the uncertainties on the muon identification and the separation of the elastic and proton dissociative events are partly correlated. Taking only the uncorrelated uncertainties into account leads to a total systematic uncertainty of 7.3% and 8.3% for the J/ψ photoproduction and deep inelastic scattering respectively.
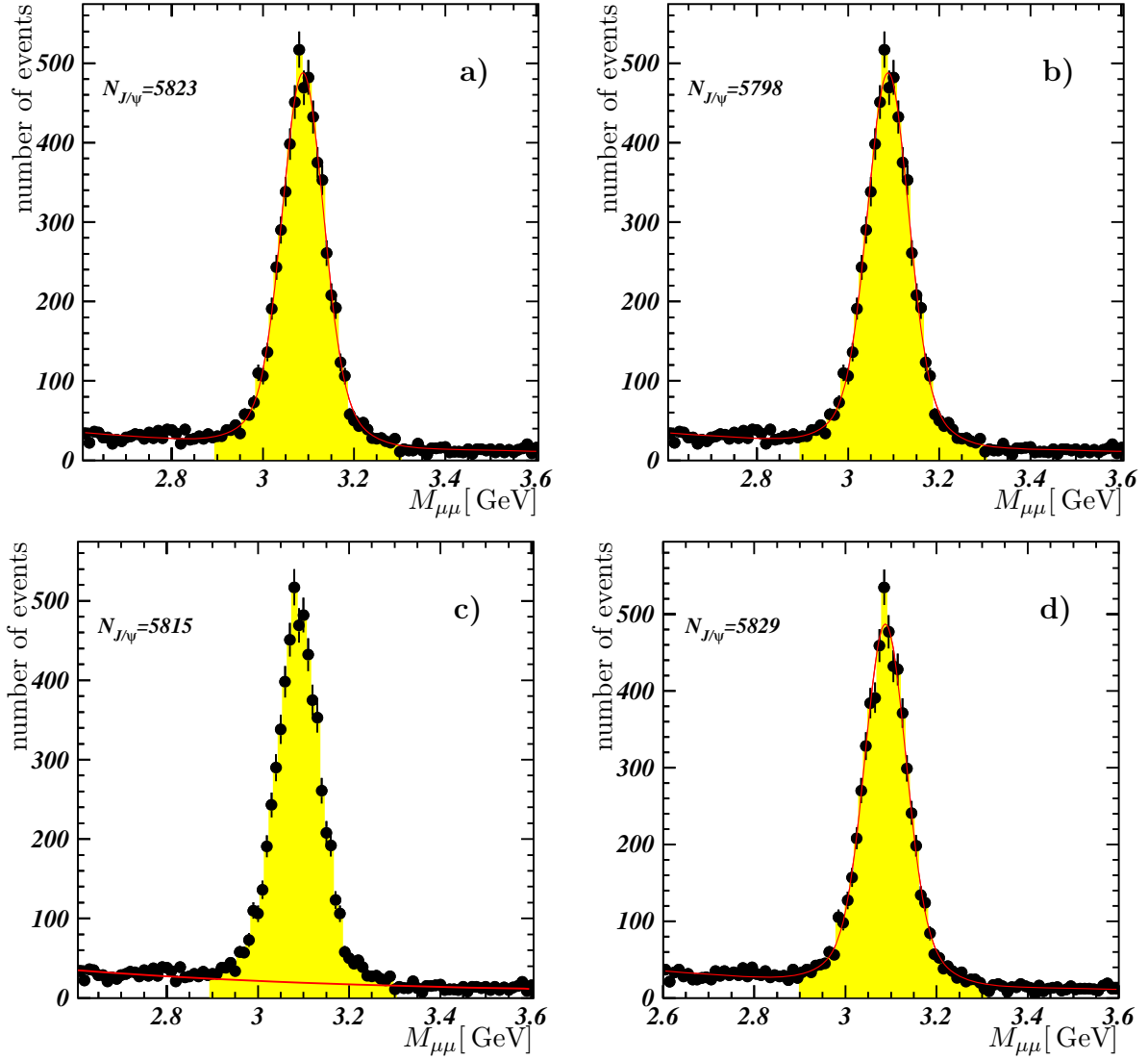
Figure 4.24: Different methods to determine the number of signal events. Shown is the total mass peak of the untagged J/ψ photoproduction of the combined data sets of the years 1999 and 2000. a)-c) show the same histogram with different fits, while d) shows a histogram with a shifted binning. The fit in a) and d) is the sum of a Gaussian and a power law distribution. In b) the background is described by an exponential function. In c) only the background is fitted by a power law distribution, while the number of signal events is extracted as the difference of all events in the mass window $2.9\,\text{GeV} < M_{\mu\mu} < 3.3\,\text{GeV}$ (shaded region) and the number of fitted background events.

5 Results

In this chapter cross sections for diffractive elastic J/ψ production are presented. To begin with the elastic photoproduction cross section is compared to previous experimental results and to theoretical predictions. In a second step the Q^2 dependence is discussed. At the end of this chapter the helicity structure of diffractive J/ψ production is studied, both in photoproduction and deep inelastic scattering.

5.1 Elastic J/ψ Photoproduction

In this section the results from the J/ψ photoproduction analysis are discussed. The cross sections are calculated using equation (4.1). Only the data sample without activity in the forward detectors is used. First the W dependence of the elastic γp cross section is investigated. Then the differential cross section $d\sigma/dt$ is analysed followed by a study of the effective Pomeron trajectory.

5.1.1 W dependence

The cross section results for the diffractive elastic photoproduction of J/ψ mesons $\sigma(\gamma p \to J/\psi p)$ as a function of the centre-of-mass energy W are listed in table 5.1 and displayed in figures 5.1 to 5.4. The first column shows the boundaries of the analysis bins together with the mean value of W in each bin. These values are derived by performing a bin centre correction as described in section 4.2. In the third column the number of observed events without forward tag is given along with the statistical errors. The fifth column shows the elastic cross section $\sigma_{\gamma p}^{\mathrm{el}}$ determined from the combined data sets of the periods 1999 (e^- and e^+) and 2000. The last column shows the results of the slope parameter b_{el}, which will be explained in section 5.1.3.

Figure 5.1 shows the elastic γp cross section $\sigma(\gamma p \to J/\psi p)$ as a function of W. The inner error bars correspond to the statistical error, the outer bars show the total error derived from the statistical error and the systematic uncertainty added in quadrature. A fit[1] of

---

[1] The errors on fit parameters given in the text are derived as follows. The fit is performed twice. First only the statistical errors of the data points are used. The resulting error on the fit parameter is then used as the statistical error on that result. In a second step the fit is repeated using the total errors. To derive the systematic error on the fit parameter the difference of the two errors is calculated in quadrature.

W [GeV]	$\langle W \rangle$ [GeV]	$N_{\text{no tag}}$	Φ_γ [10^{-4}]	$\sigma_{\gamma p}^{\text{el}}$ [nb]	$b_{\text{el}}(W)$ [GeV^{-2}]
40- 50	44.8	549± 40	224	46.0±2.4±4.0	4.09±0.20±0.03
50- 60	54.8	596± 41	174	48.4±2.3±4.3	4.36±0.18±0.02
60- 70	64.8	619± 42	141	59.6±2.8±5.2	4.73±0.20±0.02
70- 80	74.8	572± 43	117	62.7±3.2±5.5	4.30±0.22±0.03
80- 90	84.9	646± 43	99	72.6±3.4±6.4	4.43±0.20±0.03
90-100	94.9	620± 41	85	78.5±3.7±6.9	4.72±0.21±0.03
100-110	104.9	569± 39	74	82.5±4.0±7.3	4.79±0.23±0.03
110-130	119.5	875± 49	121	91.4±3.5±8.0	4.70±0.16±0.02
130-160	144.1	682± 43	135	98.2±4.4±8.6	5.16±0.19±0.02

Table 5.1: Cross section results as a function of W for the photoproduction data sample of the total data taking period in the kinematic range $-t \leq 1.2\,\text{GeV}^2$ ($\langle -t \rangle = 0.25\,\text{GeV}^2$) and $Q^2 \leq 1\,\text{GeV}^2$ ($\langle Q^2 \rangle = 0.05\,\text{GeV}^2$). $\langle W \rangle$ denotes the mean value of W in each analysis bin calculated according to equation (4.2). $N_{\text{no tag}}$ is the number of observed signal events without a forward tag together with the statistical error. Φ_γ is the photon flux used to derive the elastic γp cross section $\sigma_{\gamma p}^{\text{el}}$. $b_{\text{el}}(W)$ is the slope parameter of the t dependence (see equation (1.8)). For the last two columns the statistical and systematic errors are given separately.
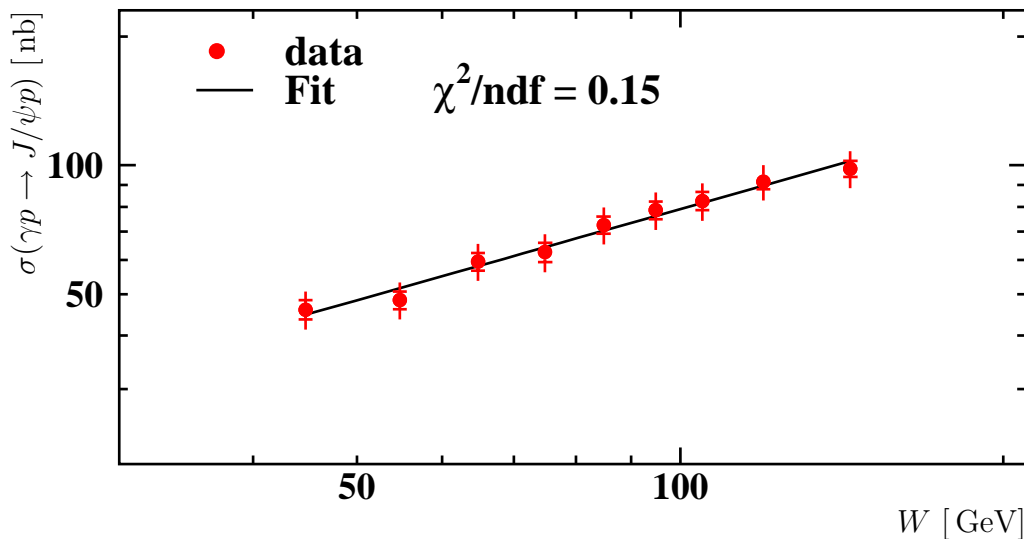
Figure 5.1: Elastic photoproduction cross section $\sigma_{\gamma p}^{\text{el}}$ as a function of the centre-of-mass energy W. The inner error bars show the statistical error, while the outer bars show the total uncertainty. The solid line shows the result of a fit $\sigma_{\gamma p}^{\text{el}} \propto (W/90\,\text{GeV})^\delta$ yielding a value of $\delta = 0.71 \pm 0.04 \pm 0.07$.

the form $\sigma_{\gamma p} \propto (W/90\,\text{GeV})^\delta$ is applied to the data yielding a value of

$$\delta = 0.71 \pm 0.04 \pm 0.07.$$

The result for δ is in good agreement with the values given in [42, 51]:

$$\begin{aligned} \delta_{\text{ZEUS}} &= 0.69 \pm 0.02 \pm 0.03 \\ \delta_{\text{H1}} &= 0.83 \pm 0.07 \end{aligned}$$

The ZEUS result (see figure 5.2) is derived from a combination of measurements of the J/ψ decay into two muons and the decay into an e^+e^- pair. The ZEUS analysis of the decay $J/\psi \to \mu^+\mu^-$ uses a slightly different kinematic region, $30\,\text{GeV} < W < 170\,\text{GeV}$ and $-t < 1.8\,\text{GeV}^2$. The fit result to the muon decay channel yields $\delta_{\text{ZEUS}} = 0.67 \pm 0.03 \pm 0.05$.

The range in W of the published H1 result (see figure 5.2) is $26\,\text{GeV} < W < 285\,\text{GeV}$, where the lowest bin is from an analysis which uses the decay $J/\psi \to \mu^+\mu^-$ in the Forward Muon Detector. The central region is the same as for this analysis, while the results for higher W values are derived from an analysis of the decay $J/\psi \to e^+e^-$. Applying the fit W^δ to the published results of H1, but replacing the central points by those of this analysis leads to

$$\delta = 0.74 \pm 0.03 \pm 0.05.$$

In this fit separate normalisation factors are applied to the individual data sets j, to account for different normalisation uncertainties:

$$\sigma_{\gamma p}^{\text{el}} = N_j \left(\frac{W}{90\,\text{GeV}} \right)^\delta$$

All normalisation factors are compatible within the errors.

Figure 5.2 shows the same data as in the previous plot. As a comparison the results from H1 and ZEUS are added. Although a very similar analysis method is used, a small shift between the published H1 results (using the data taking period 1996/97) and those from this analysis can be seen. In [77] it has been shown that the results of the year 1997, which dominate the published H1 results, are somewhat lower than those of the year 1999 and figure 4.21 shows a good agreement between results of 1999 and 2000.

Figure 5.3 shows the results from the present analysis and those at low and high W from H1. In addition, results from fixed-target experiments [110, 111] are included. The data of this analysis together with the results from H1 are used for a fit of the two-Pomeron model proposed in [55]. The fit is performed leaving only the amplitudes of the two Pomeron trajectories as free parameters. The slope and intercept of the two trajectories are fixed to [55]:

$$\begin{aligned} \text{soft} \quad &: \quad \alpha(t) = 1.0808 + 0.25\,\text{GeV}^{-2}t \\ \text{hard} \quad &: \quad \alpha(t) = 1.4180 + 0.10\,\text{GeV}^{-2}t \end{aligned} \tag{5.1}$$

The fit nicely describes the data in the kinematic range of HERA, but overestimates the results of the fixed target experiments.
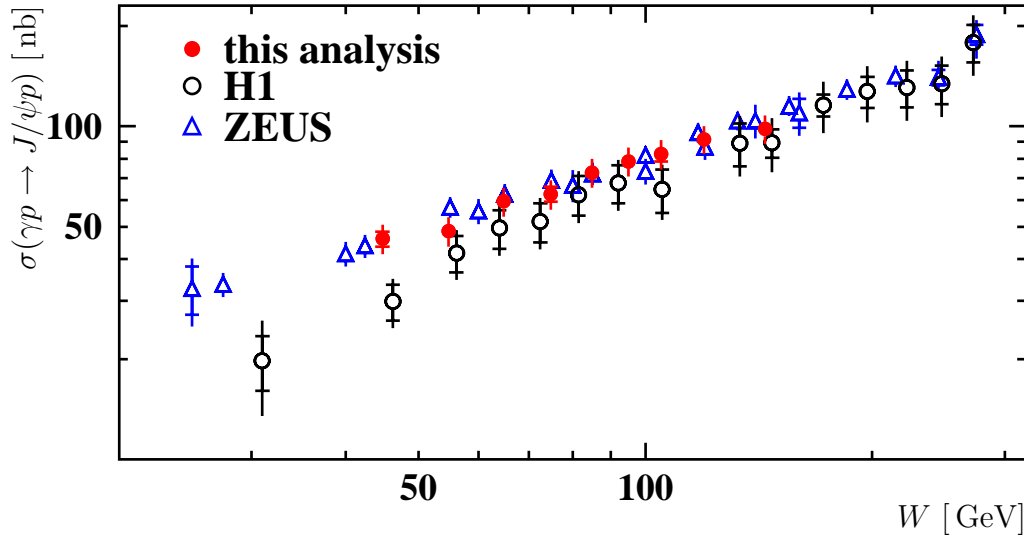
Figure 5.2: Elastic photoproduction cross section $\sigma_{\gamma p}^{\mathrm{el}}$ as a function of the centre-of-mass energy W. The inner error bars show the statistical error, while the outer bars show the total uncertainty. As a comparison the published results from H1 [42] and the combined $J/\psi \to \mu^+\mu^-$ and $J/\psi \to e^+e^-$ results from ZEUS [51] are shown.

Figure 5.4 shows again the result of this analysis together with the published H1 data outside the covered region in W. In this figure the data are compared to the results of three theoretical QCD calculations. The solid curve shows the prediction of Frankfurt, McDermott and Strikman (FMS) [17] using the CTEQ4L [112] parameterisations of the gluon density in the proton. The two other curves correspond to QCD predictions of Martin, Ryskin and Teubner (MRT) [20], using two different parameterisations of the gluon density. The dashed curve uses CTEQ5M [113], while the dotted curve uses MRST99 [114].

The MRT predictions are able to describe the slope of the elastic cross section within errors. The absolute amplitude depends also on non-perturbative effects in the model. The FMS calculation is too steep.

5.1.2 t dependence

The t dependence of the elastic J/ψ photoproduction cross section is studied in the kinematic range $40\,\mathrm{GeV} < W < 160\,\mathrm{GeV}$. The results are listed in table 5.2 and displayed in the figures 5.5 to 5.8. The first column defines the bin boundaries followed by the mean value $\langle -t \rangle$ (see section 4.2). The number of observed events in the combined data sets 1999 and 2000 is given together with their statistical errors. The fourth column shows the elastic differential photoproduction cross section $d\sigma_{\gamma p}^{\mathrm{el}}/dt$ with the statistical and systematic error. The values are derived using equation (4.1) and dividing by the bin widths. The last column shows the results for the effective Pomeron trajectory $\alpha(t)$, which will be explained in section 5.1.3.
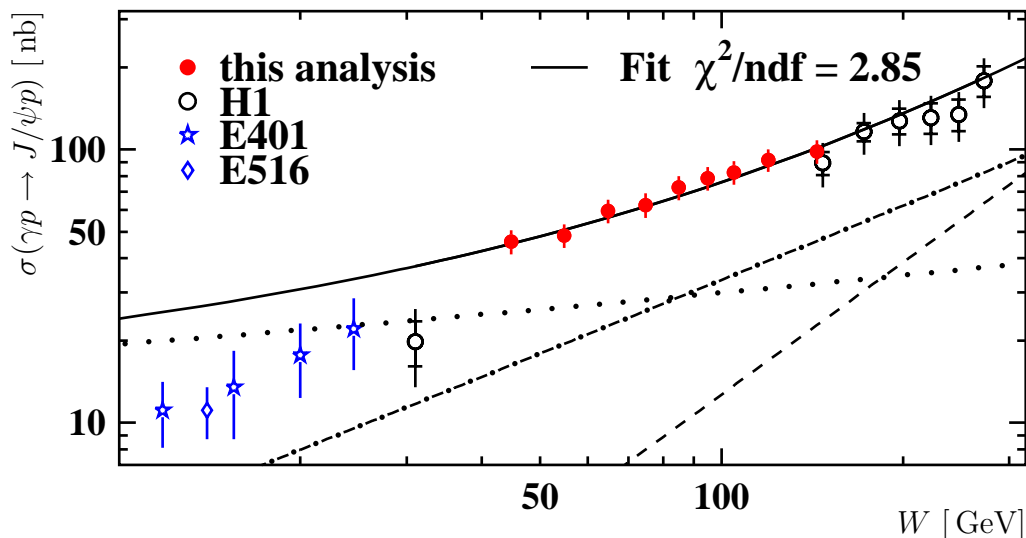
Figure 5.3: Elastic photoproduction cross section $\sigma_{\gamma p}^{\text{el}}$ as a function of the centre-of-mass energy W. The solid line shows the result of a fit of the two-Pomeron model suggested in [55]. The fit is performed using only data points of this analysis and H1. The dotted curve shows the contribution of a soft Pomeron, while the dashed line corresponds to the additional hard Pomeron. The dash-dotted line shows the interference term of both trajectories.
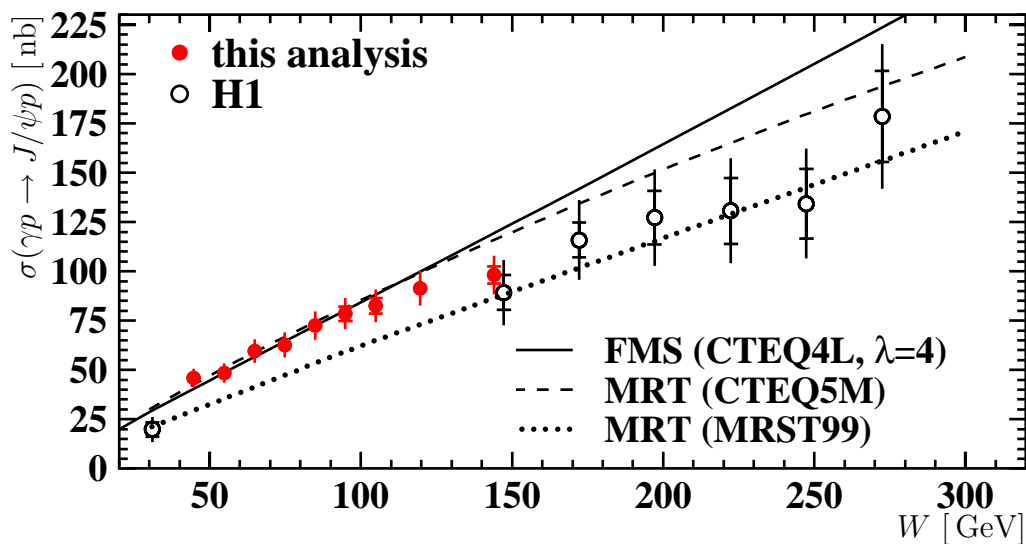
Figure 5.4: Elastic photoproduction cross section $\sigma_{\gamma p}^{\text{el}}$ as a function of the centre-of-mass energy W. The inner error bars show the statistical error, while the outer bars show the systematic uncertainty. QCD predictions [17, 20] using different parameterisations of the gluon density in the proton are compared to the data.

$\lvert t\rvert$ $\left[\,\mathrm{GeV}^2\right]$	$\langle -t\rangle$ $\left[\,\mathrm{GeV}^2\right]$	$N_{\mathrm{no\ tag}}$	$d\sigma_{\gamma p}^{\mathrm{el}}/dt$ $\left[\,\mathrm{nb}/\,\mathrm{GeV}^2\right]$	$\alpha(t)$
0.00-0.07	0.03	1603±71	284.7±9.4±25.0	1.23±0.021±0.015
0.07-0.14	0.10	1035±53	180.5±6.7±15.9	1.22±0.024±0.015
0.14-0.21	0.17	727±44	129.7±5.7±11.4	1.25±0.028±0.015
0.21-0.30	0.25	701±43	92.1±4.0± 8.1	1.20±0.026±0.015
0.30-0.40	0.35	511±37	61.2±3.1± 5.4	1.14±0.033±0.018
0.40-0.60	0.49	583±39	32.5±1.5± 2.9	1.09±0.029±0.018
0.60-0.90	0.73	383±32	10.6±0.6± 0.9	1.17±0.033±0.016
0.90-1.20	1.03	163±21	2.7±0.2± 0.3	1.02±0.052±0.019

Table 5.2: Results as a function of t for the photoproduction data sample of the total data taking period in the kinematic range $40\,\mathrm{GeV} \leq W \leq 160\,\mathrm{GeV}$ ($\langle W\rangle = 86\,\mathrm{GeV}$) and $Q^2 \leq 1\,\mathrm{GeV}^2$ ($\langle Q^2\rangle = 0.05\,\mathrm{GeV}^2$). The photon flux in this kinematic region is $\Phi_\gamma = 0.1168$. $\langle t\rangle$ denotes the mean value of t in each analysis bin calculated according to equation (4.3). $N_{\mathrm{no\ tag}}$ is the number of observed signal events without a forward tag. $\alpha(t)$ describes the W dependence of the cross section as a function of t and is discussed in section 5.1.3
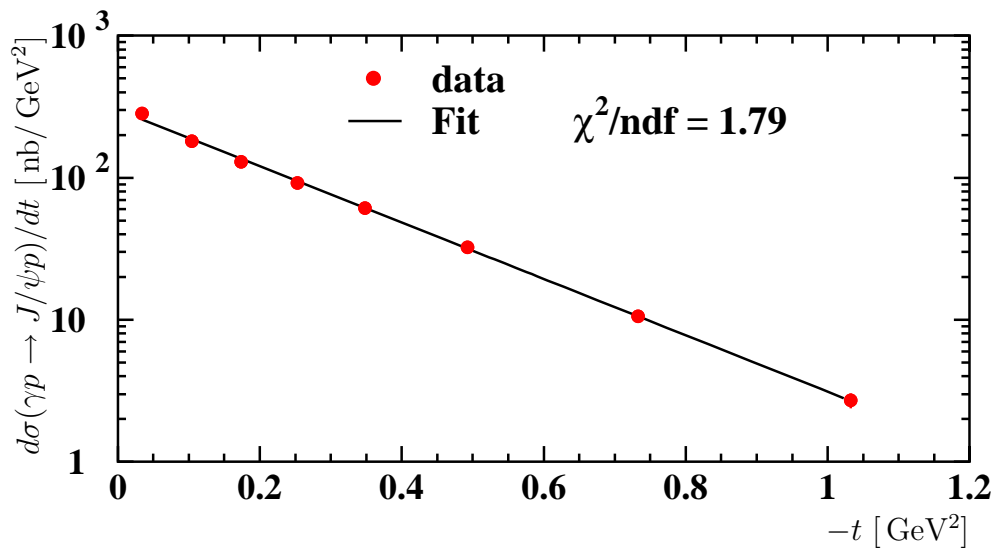
Figure 5.5: Differential elastic photoproduction cross section $d\sigma_{\gamma p}^{\mathrm{el}}/dt$ as a function of t. The solid line shows the result of a fit $\propto e^{b_{\mathrm{el}}t}$ yielding a value of $b_{\mathrm{el}} = (4.57 \pm 0.07 \pm 0.14)\,\mathrm{GeV}^{-2}$.

Figure 5.5 shows the elastic differential γp cross section as a function of t. Assuming a relation of the form

$$d\sigma_{\gamma p}^{\mathrm{el}}/dt \propto e^{b_{\mathrm{el}}t} \tag{5.2}$$

a fit[1] to the data is applied yielding a value of

$$b_{\mathrm{el}} = (4.57 \pm 0.07 \pm 0.14) \,\mathrm{GeV}^{-2}.$$

The published results from H1 and ZEUS are:

$$
\begin{aligned}
b_{\mathrm{el}}^{\mathrm{H1}} &= \left(4.73 \pm 0.25^{+0.30}_{-0.39}\right) \,\mathrm{GeV}^{-2} \\
b_{\mathrm{el}}^{\mathrm{ZEUS}} &= \left(4.15 \pm 0.05^{+0.30}_{-0.18}\right) \,\mathrm{GeV}^{-2}
\end{aligned}
$$

Again the ZEUS result is a combination of the analysis of the electron and muon decay channels of the J/ψ. Using the muon decay channel only a fit to the ZEUS data yields $b_{\mathrm{el}}^{\mathrm{ZEUS}} = \left(4.23 \pm 0.07^{+0.10+0.085}_{-0.12-0.051}\right) \,\mathrm{GeV}^{-2}$ where the third error refers to the modelling of the proton dissociative subtraction. The value measured in this analysis agrees well with all of these results within the total errors.

In [23] it is argued that the simple exponential relation of equation (5.2) is not correct. The authors expect a dependence of the form

$$\frac{d\sigma_{\gamma p}^{\mathrm{el}}}{dt} \propto \Gamma^2(t) = \frac{1}{(1 - t/m_{2g}^2)^4} \tag{5.3}$$

where $\Gamma(t)$ is a two-gluon form factor with an expected value of $m_{2g} \sim 1 \,\mathrm{GeV}$. In figure 5.6 a fit of this form to the data is performed leading to

$$m_{2g} = (0.678 \pm 0.006 \pm 0.012) \,\mathrm{GeV}.$$

The fit yields $\chi^2/ndf = 20.14$ which is much worse than that of the exponential.

In [23, 115] a combination of the equations (5.2) and (5.3) is proposed, leading to

$$\frac{d\sigma_{\gamma p}^{\mathrm{el}}}{dt} \propto \frac{1}{(1 - t/m_{2g}^2)^4} e^{bt}.$$

In a first step the value of $m_{2g} = 1 \,\mathrm{GeV}$ is fixed. The two parameter fit shown in figure 5.7 gives a better description of the data ($\chi^2/ndf = 2.88$) yielding

$$b_{\mathrm{el}} = (5.86 \pm 0.06 \pm 0.14) \,\mathrm{GeV}^{-2}.$$

In a last step m_{2g} is used as a free parameter. The result ($\chi^2/ndf = 1.70$) is shown in figure 5.8. The quality of the description of the data is compatible to the simple exponential fit. The result of the fit parameters are:

$$
\begin{aligned}
b_{\mathrm{el}} &= (3.36 \pm 0.58 \pm 0.53) \,\mathrm{GeV}^{-2} \\
m_{2g} &= (1.68 \pm 0.36 \pm 0.42) \,\mathrm{GeV}
\end{aligned}
$$

---

[1]see footnote 1 on page 73
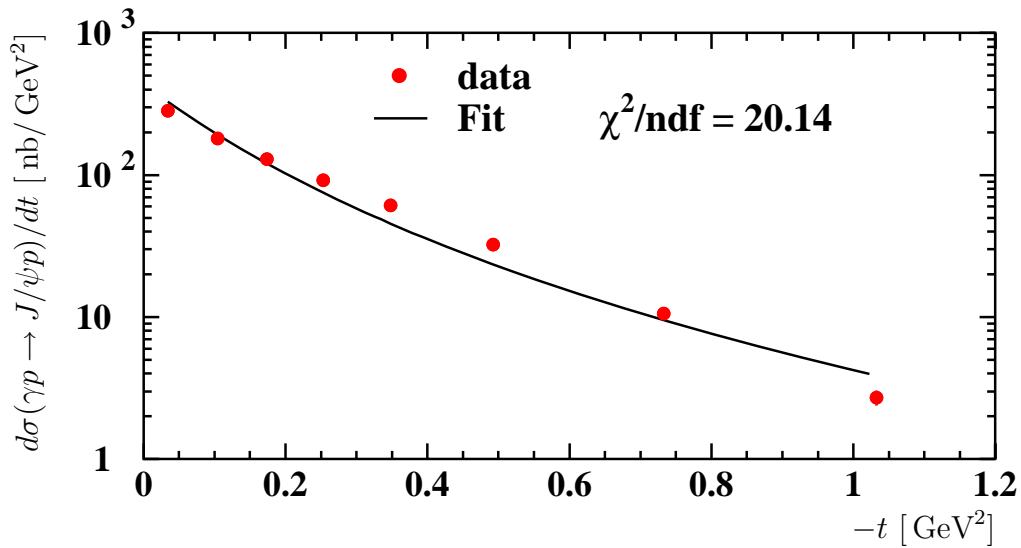
Figure 5.6: Differential elastic photoproduction cross section $d\sigma_{\gamma p}^{\mathrm{el}}/dt$ as a function of t. The same data as in figure 5.5 are shown. This time a fit of the form $\propto (1 + t/m_{2g}^2)^{-4}$ is performed as proposed in [23] yielding a value of $m_{2g} = (0.678 \pm 0.006 \pm 0.012)\,\mathrm{GeV}$.
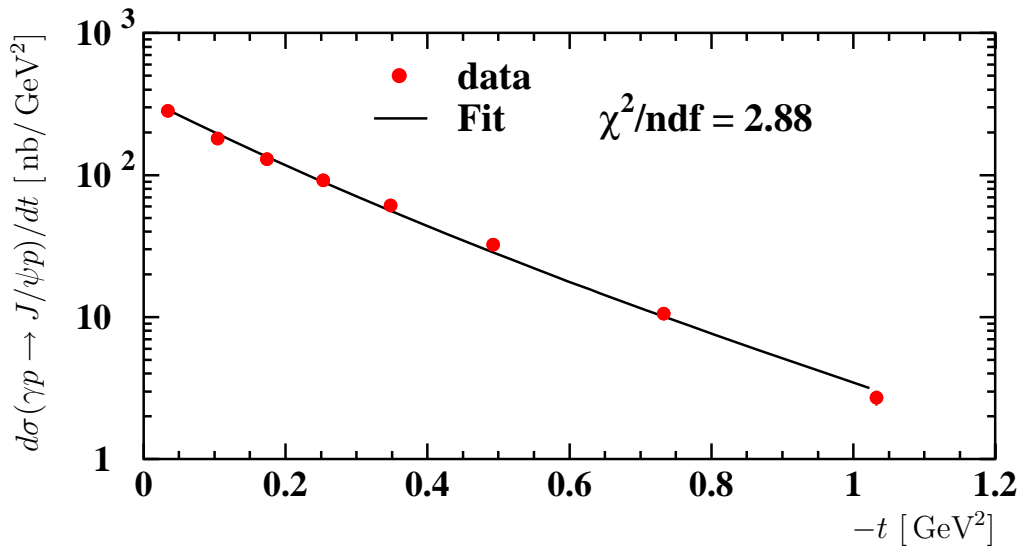
Figure 5.7: Differential elastic photoproduction cross section $d\sigma_{\gamma p}^{\mathrm{el}}/dt$ as a function of t. The same data as in figure 5.5 are shown. The solid line shows the result of a fit to the data of the form $\propto e^{bt}(1 + t/m_{2g}^2)^{-4}$ as proposed in [23]. Here the simple exponential dependence is convoluted with a contribution of a two-gluon form factor keeping $m_{2g} = 1\,\mathrm{GeV}$ fixed. The fit yields a value of $b_{\mathrm{el}} = (5.86 \pm 0.06 \pm 0.14)\,\mathrm{GeV}^{-2}$.

5.1.3 Effective Pomeron trajectory

In this section the effective Pomeron trajectory is analysed assuming a simple linear parameterisation as in equation (1.3) $\alpha(t) = \alpha_0 + \alpha' t$. The W and t dependence of the elastic photoproduction cross section are analysed simultaneously.

In a first step the W dependence is studied in eight bins of t. The result is shown in figure 5.9. A fit[1] of the form

$$d\sigma_{\gamma p}^{\mathrm{el}}/dt \propto (W/90\,\mathrm{GeV})^\delta = (W/90\,\mathrm{GeV})^{4(\alpha(t)-1)}$$

is performed for each t bin separately. The extracted values are shown in table 5.2.

Figure 5.10 shows the fit results $\alpha(t)$ as a function of t at the mean values $\langle -t \rangle$ derived using equation (4.3). Also shown is the 1σ error band of the fit. This band is derived taking the correlation coefficient of the fit parameters $\delta_{\alpha'}^{\alpha_0} = 0.646$ into account. Assuming a linear parameterisation of the trajectory leads to

$$
\begin{aligned}
\alpha_0 &= 1.240 \pm 0.015 \pm 0.018 \\
\alpha' &= (0.181 \pm 0.039 \pm 0.022)\,\mathrm{GeV}^{-2}.
\end{aligned}
$$

The intercept α_0 of this trajectory lies between the soft Pomeron and the hard Pomeron suggested in [55] and shown in equation (5.1). The slope α' is found to differ from zero by more than four standard deviations, but is also about two standard deviations below the value of the soft Pomeron. In figure 5.11 the data are compared to the published results of H1 and ZEUS. All measurements are in good agreement. The published values for the trajectory are:

$$
\begin{aligned}
\mathrm{H1}: &\quad \alpha_0 = 1.27 \pm 0.05 \\
(J/\psi \to \mu^+\mu-) &\quad \alpha' = 0.08 \pm 0.17\,\mathrm{GeV}^{-2} \\[4pt]
\mathrm{ZEUS}: &\quad \alpha_0 = 1.200 \pm 0.009^{+0.004}_{-0.010} \\
(J/\psi \to \mu^+\mu-,\ J/\psi \to e^+e^-) &\quad \alpha' = 0.115 \pm 0.018^{+0.008}_{-0.015}\,\mathrm{GeV}^{-2} \\[4pt]
\mathrm{ZEUS}: &\quad \alpha_0 = 1.198 \pm 0.011 \pm 0.015 \\
(J/\psi \to \mu^+\mu-) &\quad \alpha' = 0.099 \pm 0.023 \pm 0.020\,\mathrm{GeV}^{-2}
\end{aligned}
$$

In a second step the effective slope α' is also measured using the t dependence of the differential cross section as a function of W. Figure 5.12 shows the same data points as figure 5.9, but this time in bins of W as a function of t. In each bin an exponential is fitted to the data and the result is shown as a solid line. The results for the values of $b_{\mathrm{el}}(W)$ are listed in table 5.1.

Figure 5.13 shows the values b_{el} as a function of W. The solid curve shows the result of a fit to the data using equation (1.8). From this fit a value for the effective Pomeron slope can be extracted. The fit yields

$$
\begin{aligned}
b_{\mathrm{el}}(W) &= b(90\,\mathrm{GeV}) + 4\alpha' \ln(W/90\,\mathrm{GeV}) \\
b(90\,\mathrm{GeV}) &= (4.648 \pm 0.067 \pm 0.040)\,\mathrm{GeV}^{-2} \\
\alpha' &= (0.172 \pm 0.045 \pm 0.026)\,\mathrm{GeV}^{-2}
\end{aligned}
$$

---

[1]see footnote 1 on page 73
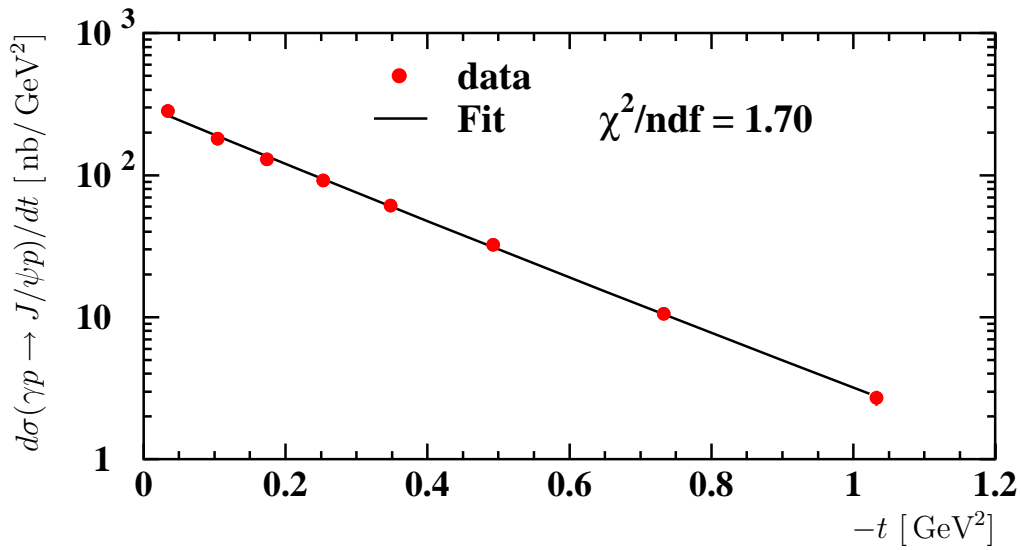
Figure 5.8: Differential elastic photoproduction cross section $d\sigma^{\text{el}}_{\gamma p}/dt$ as a function of t. The same functional form as in figure 5.7 is used to fit the data, but this time m_{2g} is used as a free parameter yielding $m_{2g} = (1.68 \pm 0.36 \pm 0.42)\,\text{GeV}$ and $b_{\text{el}} = (3.36 \pm 0.58 \pm 0.53)\,\text{GeV}^{-2}$.
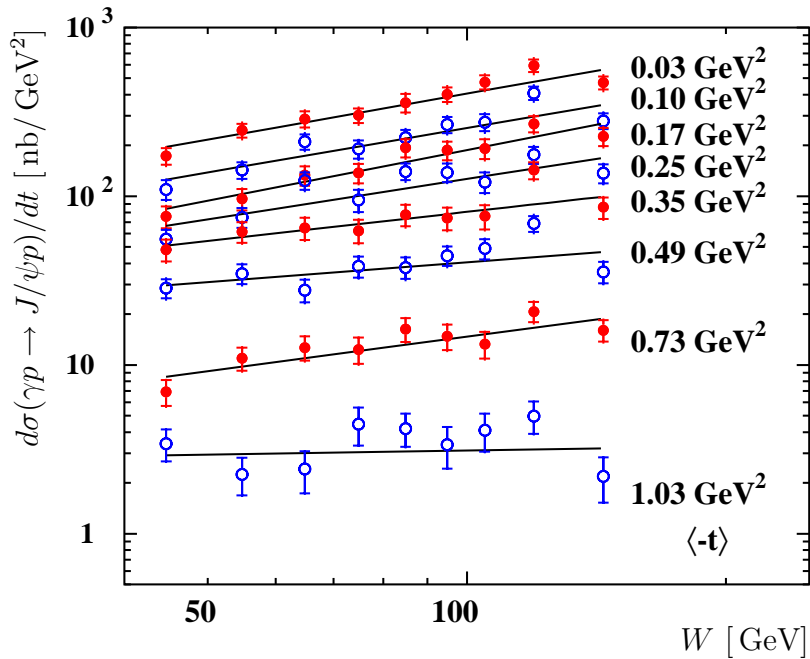
Figure 5.9: Differential elastic photoproduction cross section as a function of W measured in eight bins of t. The mean value $\langle -t \rangle$ is given for each bin on the right hand side. The inner error bars show the statistical error, while the outer error bars show the statistical error and systematic uncertainty added in quadrature. The solid lines show the result of fits to the data of the form $d\sigma^{\text{el}}_{\gamma p}/dt \propto W^{\delta} = W^{4(\alpha(t)-1)}$.
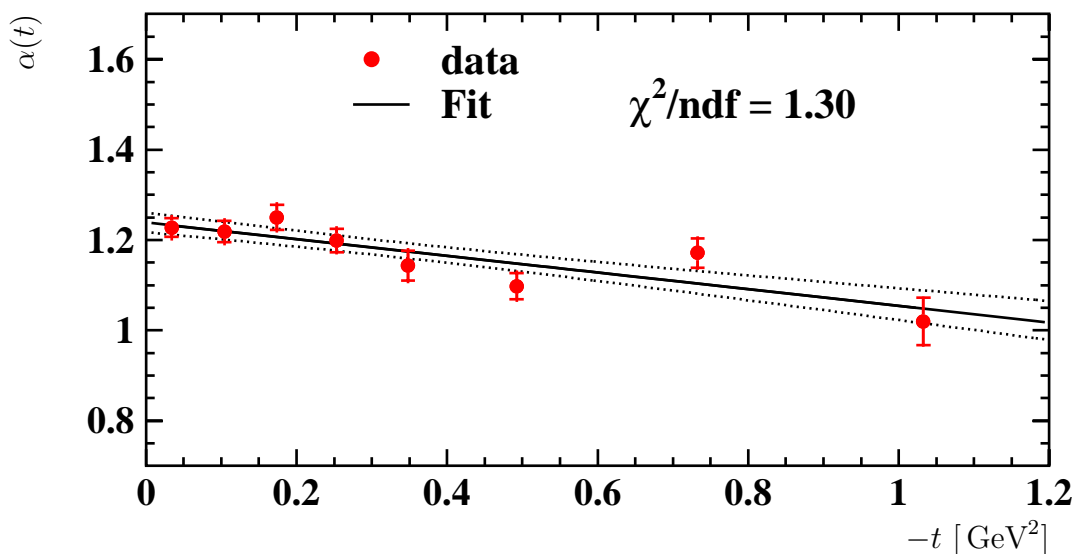
Figure 5.10: Effective Pomeron trajectory $\alpha(t)$ obtained for elastic J/ψ photoproduction. The data are derived from the fits in figure 5.9 plotted at the mean value $\langle -t \rangle$ of each bin. The inner error bars show the statistical error, while the outer error bars show the statistical error and systematic uncertainty added in quadrature. The solid line shows the result of a fit $\alpha(t) = \alpha_0 + \alpha' t$. The dotted lines show the 1σ error band of the fit taking the correlation coefficient of the fit parameters into account.
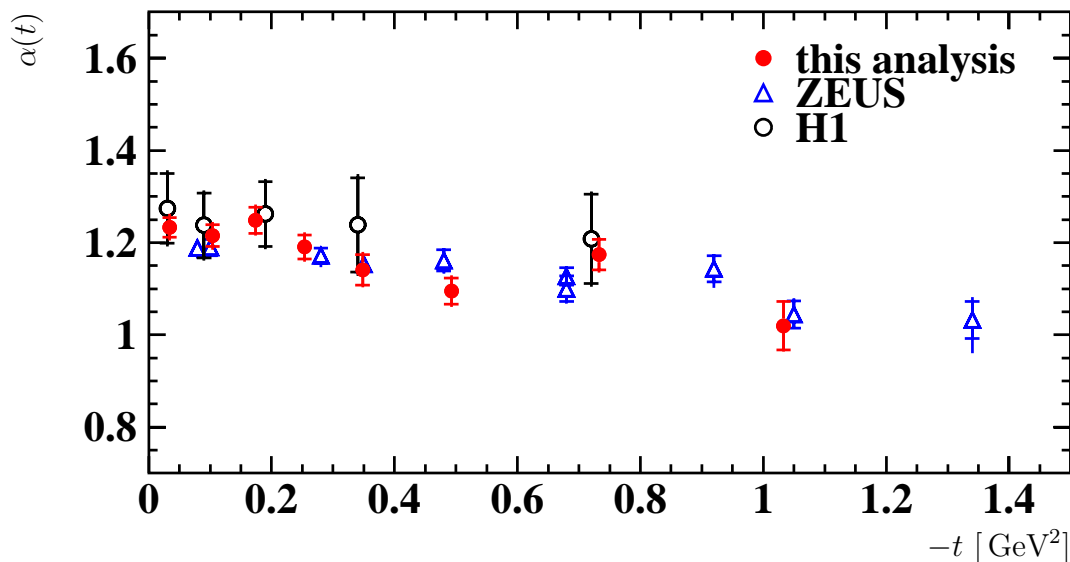
Figure 5.11: Effective Pomeron trajectory $\alpha(t)$ obtained for elastic J/ψ photoproduction. The same data as in figure 5.10 are displayed. The inner error bars show the statistical error, while the outer error bars show the statistical error and systematic uncertainty added in quadrature. The result of this analysis is compared to results from H1 [42] and ZEUS [51].
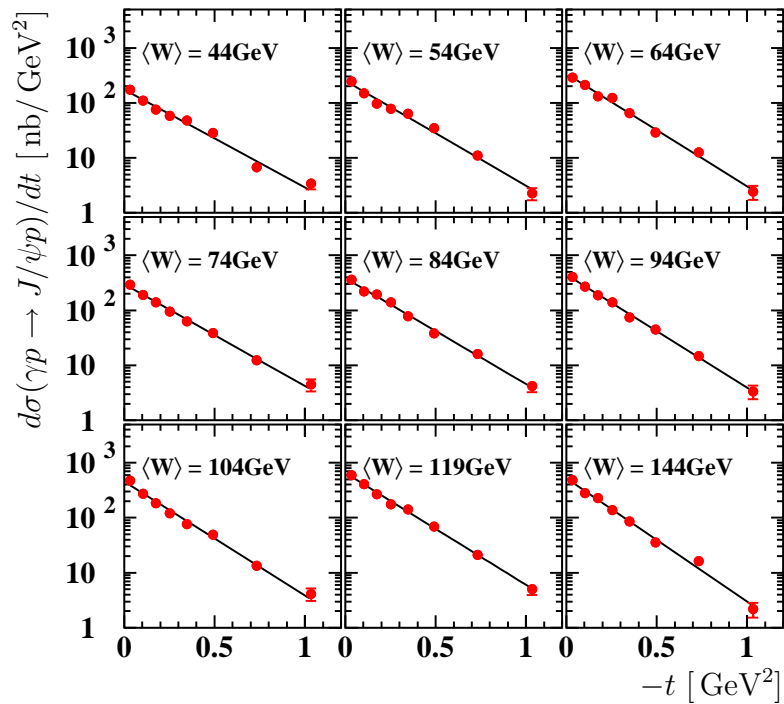
Figure 5.12: Differential elastic photoproduction cross section $d\sigma^{\text{el}}_{\gamma p}/dt$ of the elastic process $J/\psi \rightarrow \mu^+\mu-$ as a function of t in different bins of W. The mean value $\langle W \rangle$ is given for each bin. The solid lines show the result of fits to the data using an exponential form.

which is in good agreement with the value derived from the fit to $\sigma(W)$ in bins of t.

Both methods to extract α' are also combined in a two-dimensional fit. For this fit a combined χ^2 is calculated from the two equations

$$
\begin{aligned}
\sigma_{\gamma p} &\propto (W/90\,\text{GeV})^{4(\alpha_0 + \alpha' t - 1)} \\
d\sigma/dt &\propto e^{[b(90\,\text{GeV}) + 4\alpha' \ln(W/90\,\text{GeV})]t}
\end{aligned}
$$

leading to

$$
\begin{aligned}
\alpha_0 &= 1.239 \pm 0.013 \pm 0.009 \\
b_{\text{el}}(90\,\text{GeV}) &= (4.663 \pm 0.066 \pm 0.038)\,\text{GeV}^{-2} \\
\alpha' &= (0.177 \pm 0.034 \pm 0.017)\,\text{GeV}^{-2}.
\end{aligned}
$$

In figure 5.14 the published results from ZEUS are also shown. The extracted values for $b(W)$ are

$$
\begin{aligned}
\text{ZEUS:}\quad b(90\,\text{GeV}) &= (4.15 \pm 0.05^{+0.30}_{-0.18})\,\text{GeV}^{-2} \\
\alpha' &= (0.116 \pm 0.026^{+0.010}_{-0.025})\,\text{GeV}^{-2}.
\end{aligned}
$$

There is a small difference between the result of ZEUS and this analysis for the value $b(90\,\text{GeV})$ which has already been seen in [80]. The separation of elastic and proton dissociative events has the biggest effect on this value, due to a different t dependence. In this analysis the systematic uncertainty for this separation could be reduced compared to the published H1 results in [42], but it is still one of the largest contributions to the total uncertainty.
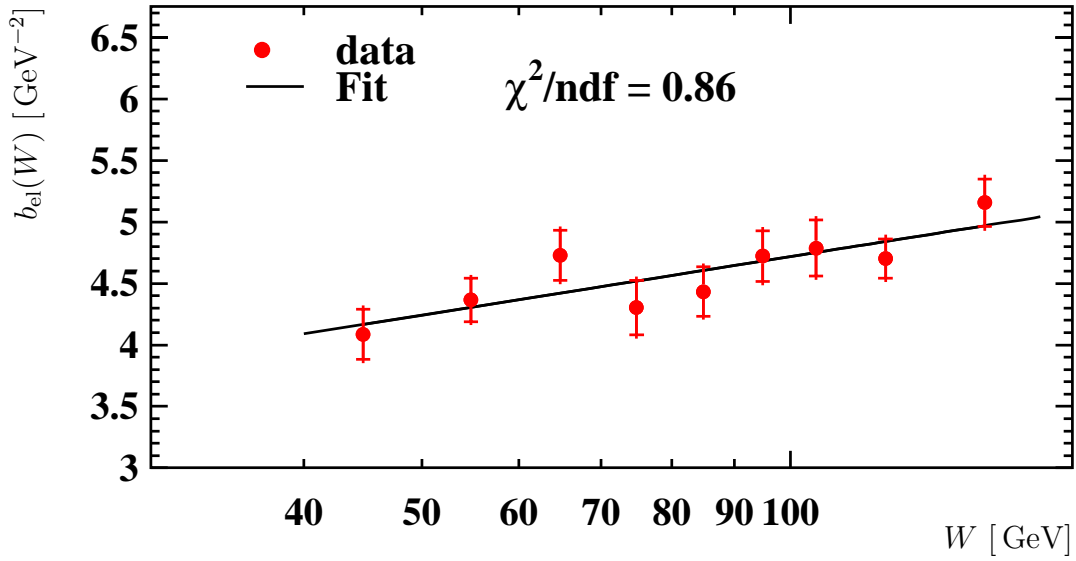
Figure 5.13: Values of the slope b of the t dependence of the differential photo-production cross section as a function of W plotted at the mean value $\langle W \rangle$ of each bin. The data are derived from the fits in figure 5.12. The inner error bars show the statistical error, while the outer error bars show the statistical error and systematic uncertainty added in quadrature. The solid line shows the result of a fit to the data of the form $b_{\mathrm{el}}(W) = b(90\,\mathrm{GeV}) + 4\alpha' \ln(W/90\,\mathrm{GeV})$.
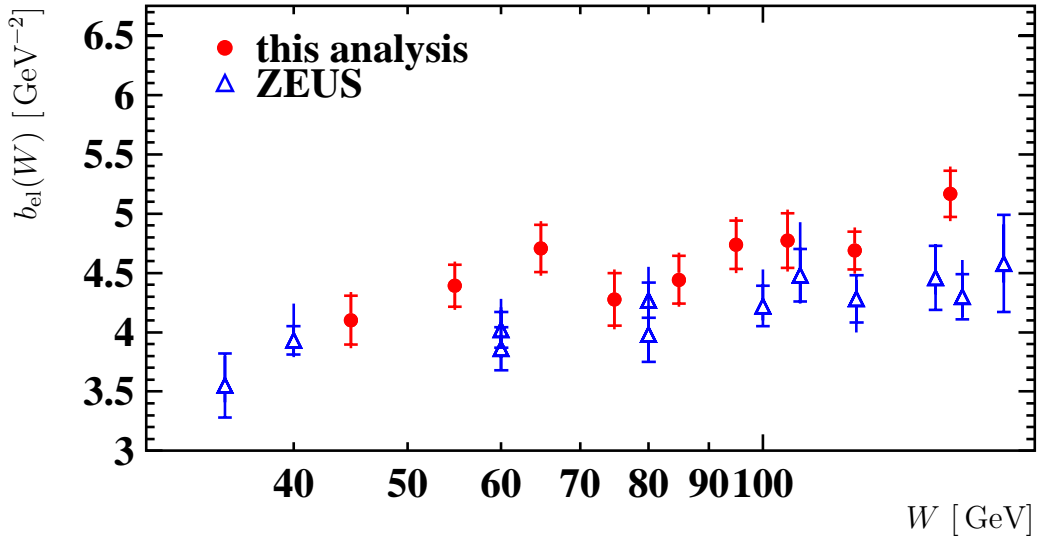
Figure 5.14: Values of the slope b of the t dependence of the differential photo-production cross section as a function of W. The same data as in figure 5.13 are displayed. The result of this analysis is compared to results from ZEUS [51].

5.2 Deep Inelastic Scattering

In this section elastic diffractive J/ψ electroproduction results are presented. The structure of this section is analogous to the previous section, but first the Q^2 dependence of the cross section is however also added. Afterwards the W dependence of the elastic cross section is analysed, followed by a study of the t dependence of the differential cross section $d\sigma_{\gamma^*p}^{\mathrm{el}}/dt$. The effective Pomeron trajectory is then measured. In all subsections the results are compared to those obtained for elastic J/ψ photoproduction. Also a comparison to results from other analyses and theoretical predictions is performed.

5.2.1 Q^2 dependence

The Q^2 dependence of the elastic diffractive cross section $\sigma(\gamma^*p \to J/\psi p)$ is shown in figure 5.15 for $40\,\mathrm{GeV} < W < 160\,\mathrm{GeV}$ and $|t| < 1.2\,\mathrm{GeV}^2$. The values are given in table 5.3. The solid line shows the result of a fit[1] to the data of this analysis of the form

$$\sigma_{\gamma^*p} \propto (M_\psi^2 + Q^2)^{-n}$$

yielding a value of

$$n = 2.460 \pm 0.080 \pm 0.048.$$

The fit gives a good description of the data ($\chi^2/ndf = 0.42$). In the fit also the value of the photoproduction cross section at $\langle Q^2 \rangle = 0.05\,\mathrm{GeV}^2$ is used. In the figure also a QCD prediction, based on a skewed parton distribution, from Martin et al. [20] using the gluon distribution CTEQ(5M) [113] is shown, which gives a reasonable description of the data.

In addition the published results from H1 [116] are shown, which are in good agreement with the results of this analysis. The result of the same fit to the published data of H1 and a preliminary result from ZEUS [117] are:

$$n_{\mathrm{H1}} = 2.38 \pm 0.11$$

$$n_{\mathrm{ZEUS}} = 2.60 \pm 0.11^{+0.09}_{-0.08}$$

All results agree within errors.

The fit is repeated in two regions of Q^2 to look for a possible change in the Q^2 dependence, which might give an estimate on the importance of non-perturbative effects. The fit result for $Q^2 < 8\,\mathrm{GeV}^2$ yields a value of $n = 2.43 \pm 0.16 \pm 0.15$, while for the region $Q^2 > 8\,\mathrm{GeV}^2$ one obtains $n = 2.73 \pm 0.29 \pm 0.14$, which is compatible with the same dependence in the whole Q^2 region. Calculations for the Colour Dipole Model in [118] predict $n \approx 2.8$ for $Q^2 \lesssim 10\,\mathrm{GeV}^2$ and $n \approx 3.2$ for $15\,\mathrm{GeV}^2 \lesssim Q^2 \lesssim 100\,\mathrm{GeV}^2$. Though the absolute values are somewhat larger than the values measured here, the tendency is the same.

For a last fit only the DIS data are used, leaving out the photoproduction result. This fit yields $n = 2.49 \pm 0.14 \pm 0.08$, which is in good agreement with the total result, but with increased errors.

---

[1]see footnote 1 on page 73
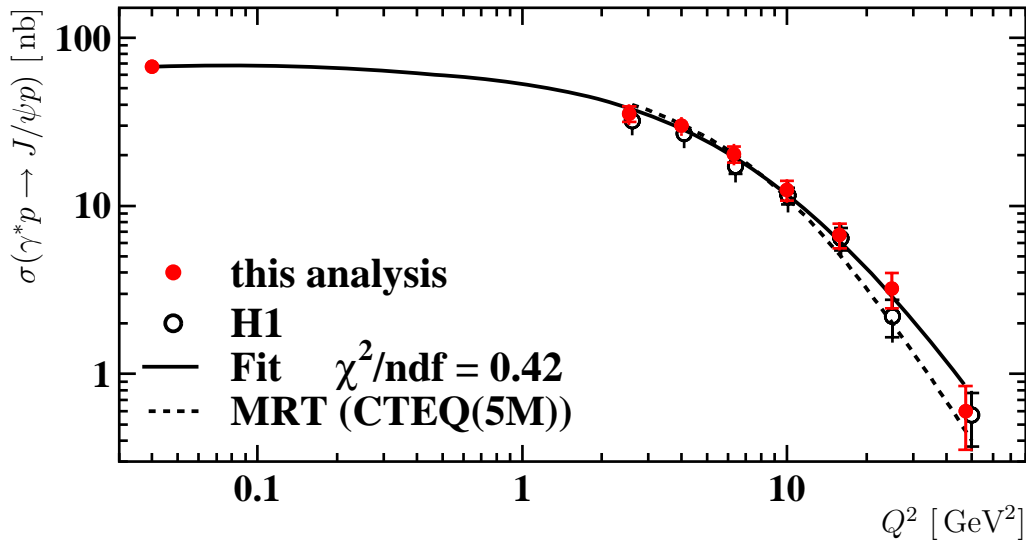
Figure 5.15: Elastic cross section for the diffractive J/ψ production as a function of Q^2. The inner error bars show the statistical error, while the outer error bars show the statistical and systematic uncertainties added in quadrature. Also shown is the photoproduction cross section at $\langle Q^2 \rangle = 0.05\,\text{GeV}^2$, as well as the published results from H1 [116]. The solid line is a fit to the data of this analysis including the photoproduction result of the form $\sigma_{\gamma^* p} \propto (M_\psi^2 + Q^2)^{-n}$ yielding a value of $n = 2.460 \pm 0.080 \pm 0.048$. The dashed curve shows a QCD prediction from Martin et al. [20] using the gluon distribution CTEQ(5M) [113].

Q^2 [GeV^2]	$\langle Q^2 \rangle$ [GeV^2]	$N_{\text{no tag}}$	Φ_γ [10^{-5}]	$\sigma^{\text{el}}_{\gamma^* p}$ [nb]
2.0- 3.2	2.5	119± 18	278	35.2±3.7±3.4
3.2- 5.0	4.0	163± 22	264	29.9±2.5±2.9
5.0- 8.0	6.3	101± 17	278	20.3±2.2±2.0
8.0-12.7	10.0	69± 14	274	12.4±1.6±1.2
12.7-20.1	15.8	40± 10	272	6.7±1.1±0.6
20.1-31.8	25.0	21± 8	269	3.2±0.8±0.3
31.8-80.0	47.3	7± 4	540	0.6±0.2±0.1

Table 5.3: Elastic electroproduction cross section as a function of Q^2. The bin boundaries are given together with the mean value of Q^2 (see section 4.2). The number of observed events without forward tag, $N_{\text{no tag}}$, is given with its statistical error. Φ_γ denotes the photon flux used to calculate the $\gamma^* p$ cross section.

5.2.2 W dependence

The W dependence of the elastic J/ψ electroproduction cross section in the range $2\,\mathrm{GeV}^2 < Q^2 < 80\,\mathrm{GeV}^2$ is shown in figure 5.16 in comparison to the photoproduction cross section (see section 5.1.1). The solid lines show the results of fits[1] of the form $\sigma \propto W^\delta$ yielding

$$
\begin{aligned}
\mathrm{PhP}: \quad \delta &= 0.71 \pm 0.04 \pm 0.07 \\
\mathrm{DIS}: \quad \delta &= 0.78 \pm 0.15 \pm 0.09
\end{aligned}
$$

In figure 5.17 the elastic J/ψ electroproduction cross section is shown as a function of W in three bins of Q^2 (see also table 5.4). The result for the photoproduction cross section is also shown in the figure ($\langle Q^2 \rangle = 0.05\,\mathrm{GeV}^2$). The solid lines show the results of fits to the data of the form $\sigma \propto W^\delta$ yielding the following values:

$$
\begin{aligned}
\delta(\langle Q^2 \rangle = 3.2\,\mathrm{GeV}^2) &= 0.67 \pm 0.20 \pm 0.14 \\
\delta(\langle Q^2 \rangle = 7.0\,\mathrm{GeV}^2) &= 0.83 \pm 0.31 \pm 0.15 \\
\delta(\langle Q^2 \rangle = 22.\,\mathrm{GeV}^2) &= 0.69 \pm 0.32 \pm 0.14
\end{aligned}
$$

All fits give a good description of the data with $\chi^2/ndf = 0.04 - 0.66$. The resulting values are compatible with each other within errors. In figure 5.18 the same data are shown in comparison with the published results from H1 [116] which use different bin boundaries at larger Q^2. A direct comparison is only possible for the first bin, which has a very similar mean value. Here the data points are in good agreement with each other within errors.

The slope parameter δ of the fits are also very similar to the one extracted in section 5.1.1 for the photoproduction sample. In some theoretical models an increase of δ with increasing values of Q^2 is expected. Due to the size of the errors no significant change in the slope is observed with increasing Q^2. This is also visible in figure 5.19. Here the extracted slope parameter δ of fits of the form $\sigma_{\gamma p} \propto W^\delta$ to the data of this analysis as well as the published results from H1 [42, 116] and ZEUS [51, 117] is shown as a function of Q^2.

---

[1] see footnote 1 on page 73
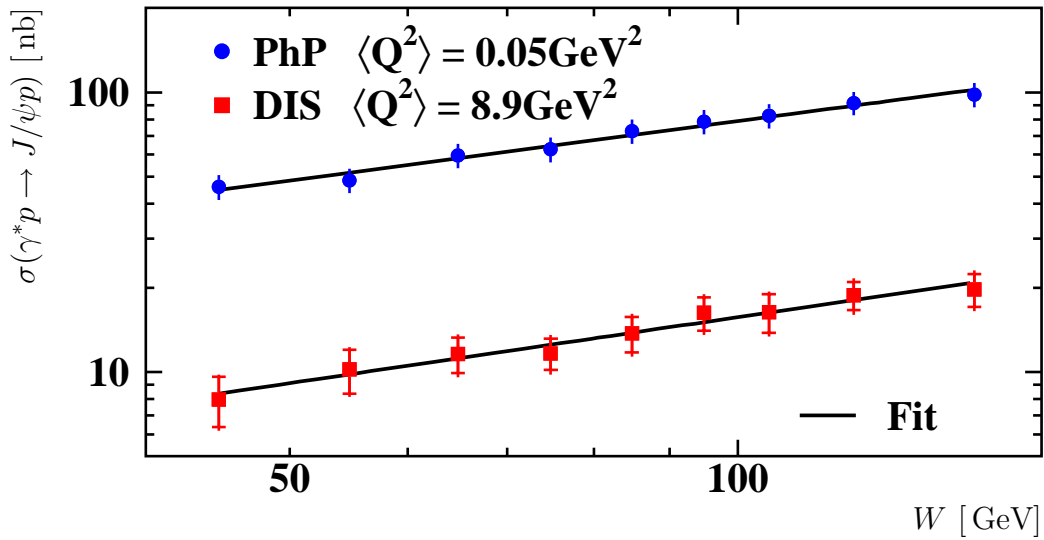
Figure 5.16: Elastic diffractive J/ψ cross section as a function of W for photopro-
duction and electroproduction. The inner error bars show the statistical error, while
the outer error bars show the statistical error and systematic uncertainty added in
quadrature. The solid lines show the results of fits to the data of the form $\sigma_{\gamma p} \propto W^\delta$.
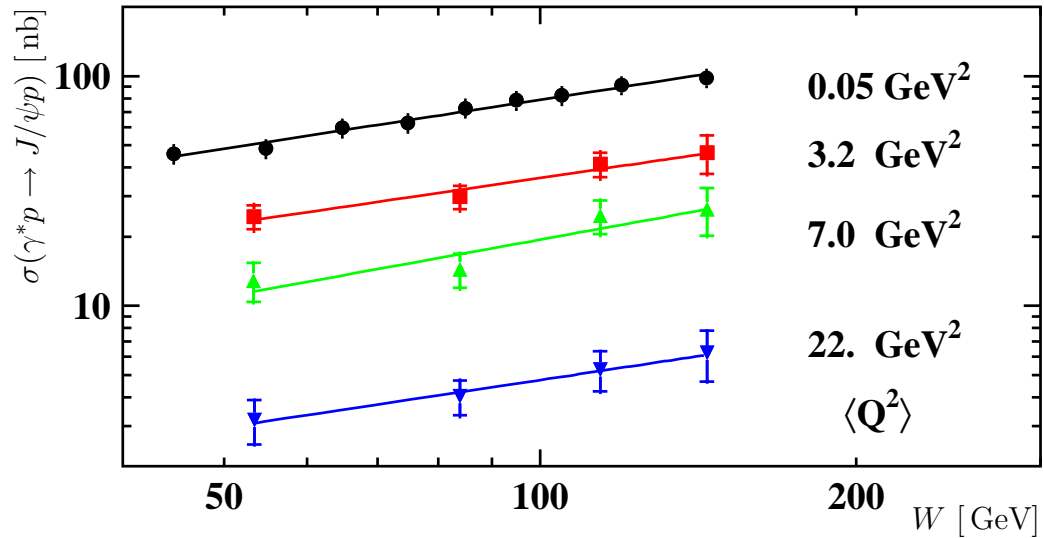
Figure 5.17: Elastic electroproduction cross section as a function of W in three bins
of Q^2. The mean value $\langle Q^2 \rangle$ in each bin is given on the right hand side of the figure.
Also displayed is the result of the photoproduction analysis with $\langle Q^2 \rangle = 0.05\,\text{GeV}^2$.
The inner error bars indicate the statistical error, while the outer bars show the
statistical and systematic uncertainties added in quadrature. The solid lines show
fits to the data of the form $\sigma_{\gamma p} \propto W^\delta$.

Q^2 $[\mathrm{GeV}^2]$	$\langle Q^2 \rangle$ $[\mathrm{GeV}^2]$	W $[\mathrm{GeV}]$	$\langle W \rangle$ $[\mathrm{GeV}]$	$N_{\mathrm{no\ tag}}$		Φ_γ $[10^{-5}]$	$\sigma_{\gamma^*p}^{\mathrm{el}}$ $[\mathrm{nb}]$
2 - 5	3.2	40- 70	53.3	84±	15	232	24.5±2.9±2.4
		70-100	83.9	90±	15	142	29.9±3.4±2.9
		100-130	114.1	78±	13	98	41.4±5.1±4.0
		130-160	144.2	29±	9	72	46.4±8.8±4.5
5 - 10	7.0	40- 70	53.3	35±	9	175	12.9±2.5±1.2
		70-100	83.9	38±	10	107	14.5±2.5±1.4
		100-130	114.1	39±	10	74	24.7±4.1±2.4
		130-160	144.2	16±	6	55	26.4±6.2±2.5
10- 80	22.	40- 70	53.3	23±	8	518	3.2±0.7±0.3
		70-100	83.9	42±	10	319	4.0±0.7±0.4
		100-130	114.1	33±	9	222	5.3±1.1±0.5
		130-160	144.2	17±	6	163	6.3±1.6±0.6

Table 5.4: Elastic electroproduction cross section of the diffractive J/ψ as a function of W in three bins of Q^2. The bin boundaries are given as well as the mean values (see section 4.2). $N_{\mathrm{no\ tag}}$ denotes the number of observed signal events without forward tag. Φ_γ is the photon flux in each analysis bin.
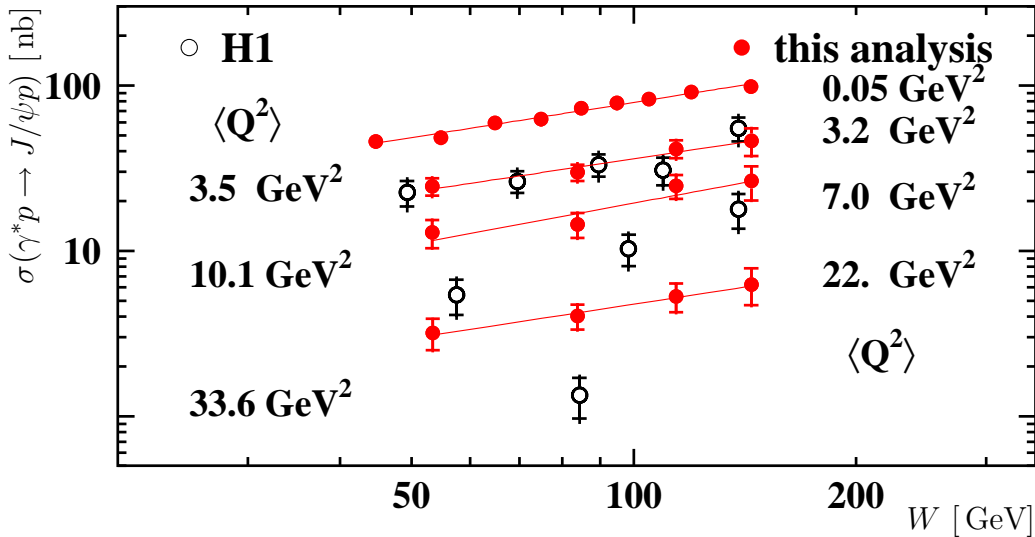
Figure 5.18: Elastic electroproduction cross section as a function of W in three bins of Q^2. The same data and fits as in figure 5.17 are shown. For comparison the published results from H1 [116] are added. The H1 results use different bin boundaries in Q^2. The mean value $\langle Q^2 \rangle$ in each bin is given in the plot for both data sets.
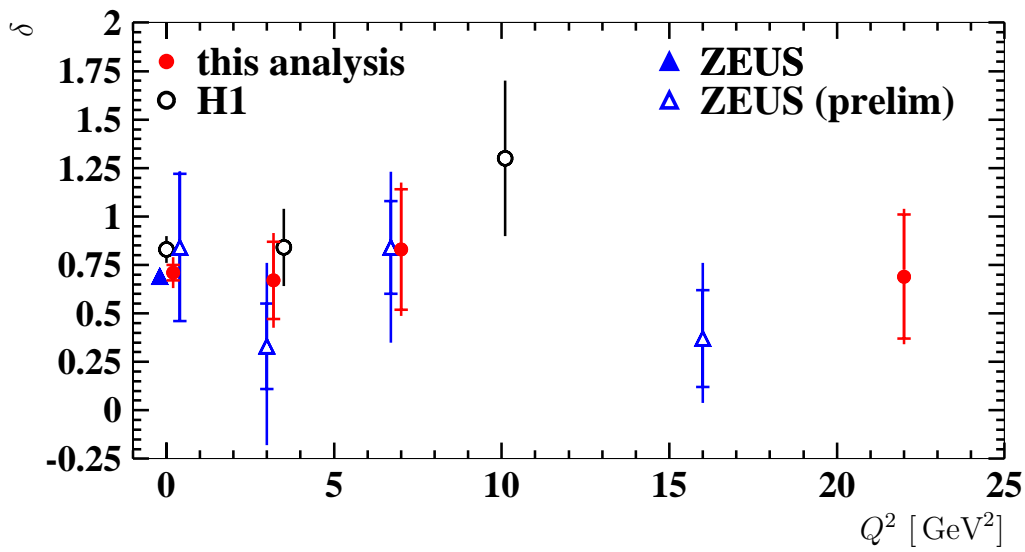
Figure 5.19: Measurements of the W dependence of the elastic J/ψ cross section as a function of Q^2. Shown are the results for δ of fits of the form $\sigma_{\gamma p} \propto W^\delta$ to the data. The inner error bars show the statistical errors only, while the outer bar show the sum of statistical errors and systematic uncertainties added in quadrature. For the data of H1 [42,116] only the total errors are given. The results from ZEUS are taken from [51,117]. For a better visibility some data points are slightly shifted along the x-axis.

5.2.3 t dependence

Figure 5.20 shows a comparison of the differential cross section $d\sigma/dt$ as a function of t for photoproduction and deep inelastic scattering. Fits[1] of the form $d\sigma/dt \propto e^{bt}$ yield

$$
\begin{aligned}
\text{PhP}: \quad b_{\text{el}} &= (4.57 \pm 0.07 \pm 0.14)\,\text{GeV}^{-2} \\
\text{DIS}: \quad b_{\text{el}} &= (4.10 \pm 0.16 \pm 0.20)\,\text{GeV}^{-2}
\end{aligned}
$$

The result for J/ψ electroproduction is in good agreement with a previous result from H1 [116] derived in a similar kinematic region of deep inelastic scattering.

$$
\text{H1}: \quad b_{\text{el}} = (4.1 \pm 0.3 \pm 0.4)\,\text{GeV}^{-2}
$$

In order to analyse the effect of Q^2 on the b slope figure 5.21 shows the differential electroproduction cross section $d\sigma/dt$ as a function of t in three bins of Q^2. The numerical values are listed in table 5.5.

The solid lines in the figure show the result of exponential fits to the data. The slope parameters b_{el} derived in each bin are:

$$
\begin{aligned}
b_{\text{el}}(\langle Q^2 \rangle = 3.2\,\text{GeV}^2) &= (4.11 \pm 0.26 \pm 0.20)\,\text{GeV}^{-2} \\
b_{\text{el}}(\langle Q^2 \rangle = 7.0\,\text{GeV}^2) &= (3.50 \pm 0.44 \pm 0.23)\,\text{GeV}^{-2} \\
b_{\text{el}}(\langle Q^2 \rangle = 22.\,\text{GeV}^2) &= (3.50 \pm 0.55 \pm 0.23)\,\text{GeV}^{-2}
\end{aligned}
$$

Figure 5.22 shows the extracted values of b_{el} as a function of Q^2. For comparison published results from H1 [42,116] and ZEUS [51,53] are included in the figure. The values of b_{el} agree with each other within errors and show a tendency of slight decreasing with increasing Q^2. This observation is in agreement with predictions in [20,118]. In [20] a Q^2 dependence of the slope parameter b_{el} is predicted:

$$
b(Q^2) = \frac{4}{\langle -t \rangle + 0.71\,\text{GeV}^2} + \frac{2}{Q^2 + M_{q\bar{q}}^2 + \langle -t \rangle} + 2\alpha' \ln\left(\frac{W^2 M_{q\bar{q}}^2}{(Q^2 + M_{q\bar{q}}^2)^2}\right) \tag{5.4}
$$

In figure 5.22 this equation is fitted to the data of the present analysis using $\langle -t \rangle = 0.3\,\text{GeV}^2$ and $W = 86\,\text{GeV}$ corresponding to the mean values in the data. The mass is chosen as $M_{q\bar{q}} = M_\psi$. Only α' is used as a free parameter for the fit, which gives a reasonable description of the data ($\chi^2/ndf = 2.69$). The fit yields $\alpha' = 0.020 \pm 0.005 \pm 0.009$. This result is smaller than the result derived for J/ψ photoproduction in section 5.1.3, however it is in good agreement with the result obtained for J/ψ electroproduction, which will be discussed in the following section.

---

[1]see footnote 1 on page 73
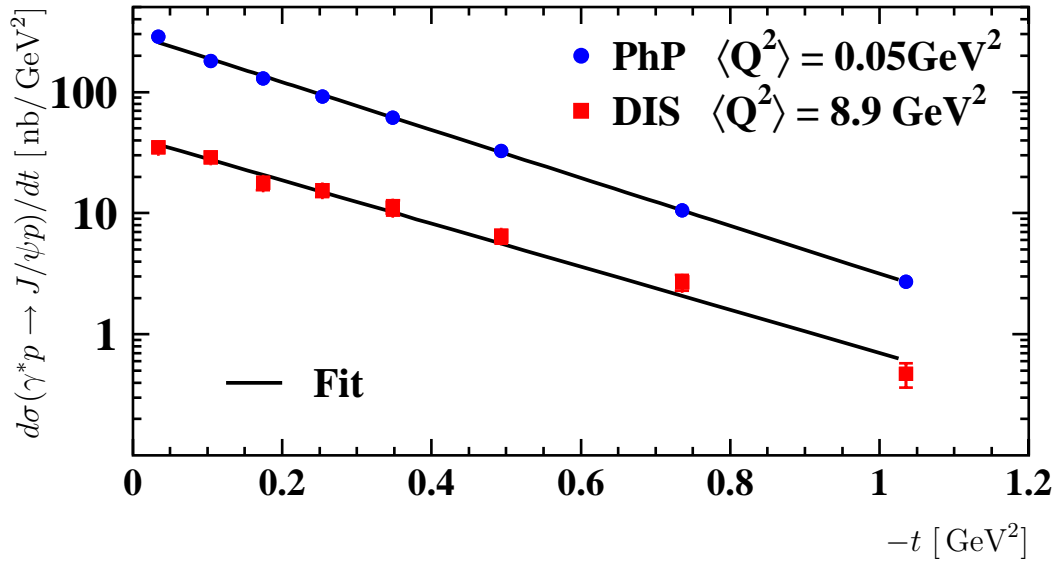
Figure 5.20: Differential cross section for elastic J/ψ production as a function of t. The results for J/ψ photoproduction (PhP) and the production in deep inelastic scattering (DIS) are shown. The solid lines show the results of fits of the form $d\sigma/dt \propto e^{bt}$.
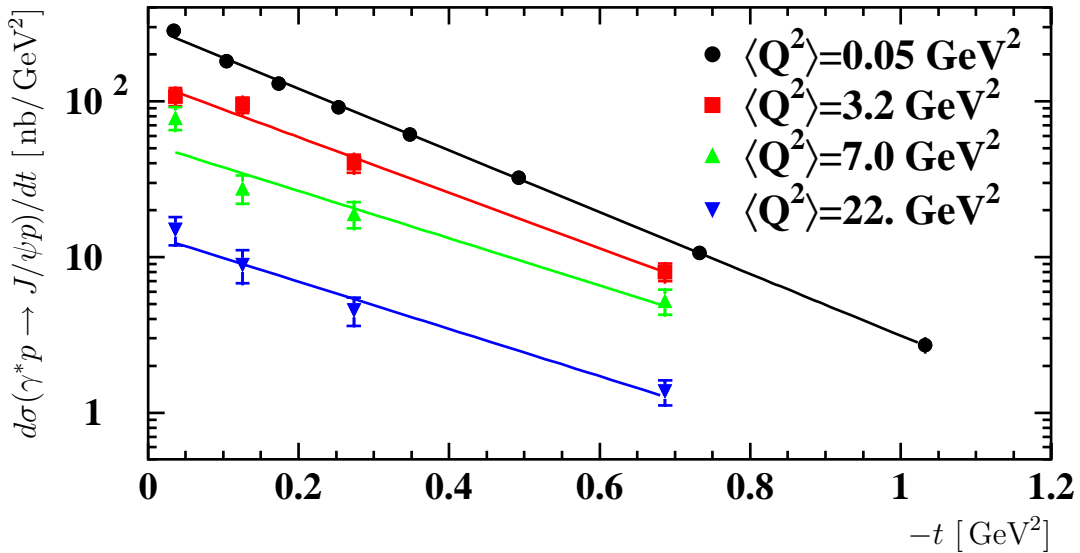
Figure 5.21: Differential cross section for elastic J/ψ electroproduction as a function of t in three bins of Q^2. The results for J/ψ photoproduction are also shown. The values of Q^2 increase from top to bottom. The mean value $\langle Q^2 \rangle$ in each bin is given in the plot (see section 4.2). The inner error bars indicate the statistical error, while the outer bars show the statistical and systematic uncertainties added in quadrature.

Q^2 [GeV^2]	$\langle Q^2\rangle$ [GeV^2]	$-t$ [GeV^2]	$\langle -t\rangle$ [GeV^2]	$N_{\text{no tag}}$		$d\sigma_{\gamma^*p}^{\text{el}}/dt$ [nb/GeV^2]
2 - 5	3.2	0.00-0.08	0.04	53±	10	107.3±14.2±10.3
		0.08-0.18	0.13	71±	11	95.1±11.0± 9.1
		0.18-0.38	0.27	63±	9	40.2± 5.4± 3.9
		0.38-1.20	0.68	56±	10	8.0± 1.0± 0.8
5 - 10	7.0	0.00-0.08	0.04	36±	8	78.6±13.2± 7.5
		0.08-0.18	0.13	20±	6	27.7± 5.7± 2.7
		0.18-0.38	0.27	27±	7	18.9± 3.7± 1.8
		0.38-1.20	0.68	31±	7	5.2± 1.0± 0.5
10- 80	22.	0.00-0.08	0.04	25±	7	15.0± 3.1± 1.4
		0.08-0.18	0.13	21±	6	8.9± 2.1± 0.9
		0.18-0.38	0.27	23±	7	4.5± 0.9± 0.4
		0.38-1.20	0.68	32±	8	1.4± 0.2± 0.1

Table 5.5: Differential cross section for elastic J/ψ electroproduction as a function of t in three bins of Q^2. Given are the bin boundaries as well as the mean value of each bin (see section 4.2). $N_{\text{no tag}}$ denotes the number of observed signal events without forward tag.
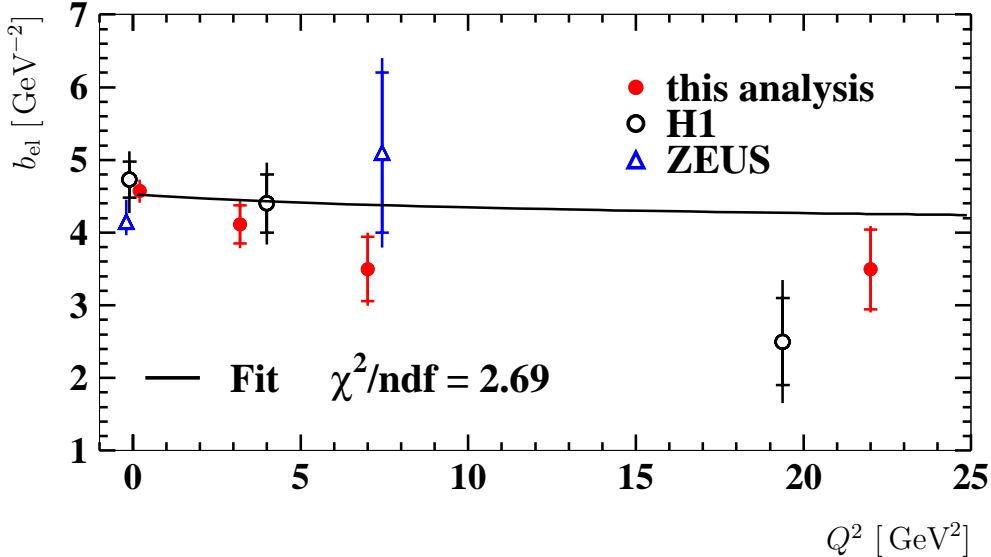
Figure 5.22: Slope parameter b_{el} derived from fits $d\sigma_{\gamma^*p}^{\text{el}}/dt \propto e^{bt}$ as a function of Q^2. The inner error bars indicate the statistical error, while the outer bars show the statistical and systematic uncertainties added in quadrature. For comparison the published results from H1 [42, 116] and ZEUS [51, 53] are also shown. For a better visibility the photoproduction points are slightly shifted along the x-axis. The solid line shows a fit of equation (5.4) to the data according to a prediction in [20].

5.2.4 Effective Pomeron trajectory

In this section the effective Pomeron trajectory is extracted for elastic J/ψ electroproduction. Following the method described in section 5.1.3 the W dependence of the cross section is analysed in different bins of t. The full range $2\,\mathrm{GeV}^2 < Q^2 < 80\,\mathrm{GeV}^2$ is used. The result is shown in figure 5.23.

The solid curves show the results of fits[1] to the data. As before fits of the form $d\sigma/dt \propto (W/90\,\mathrm{GeV})^{4(\alpha(t)-1)}$ are performed in each t range and the fit result $\alpha(t)$ is quoted in table 5.6.

Figure 5.24 shows the values of α as a function of t. The result for the elastic J/ψ photoproduction sample is included for comparison. Both data samples are fitted assuming a linear trajectory and the fit results are shown in the figure. The result of a fit $\alpha(t) = \alpha_0 + \alpha't$ to the DIS data is

$$\begin{aligned}
\alpha_0 &= 1.187 \pm 0.053 \pm 0.025 \\
\alpha' &= (0.024 \pm 0.138 \pm 0.083)\,\mathrm{GeV}^{-2}.
\end{aligned}$$

α_0 is compatible with the photoproduction result within statistical errors. α' is compatible with zero, i.e. no shrinkage, but within errors it is also compatible with the photoproduction result. The dashed lines in the figure show the 1σ error band of the fit taking the correlation coefficients of the fit parameters $\delta_{\alpha'}^{\alpha_0} = 0.667$ into account.

A similar result is obtained by analysing the t dependence of the cross section in bins of W (figure 5.25). Here an exponential is fitted to the data in each region of W leading to the values for $b_{\mathrm{el}}(W)$ given in table 5.7.

Figure 5.26 shows the fit results $b_{\mathrm{el}}(W)$ as a function of W together with the result from the elastic J/ψ photoproduction sample. A fit of the form $b_{\mathrm{el}}(W) = b(90\,\mathrm{GeV}) + 4\alpha'\ln(W/90\,\mathrm{GeV})$ yields for the DIS data

$$\begin{aligned}
b(90\,\mathrm{GeV}) &= (3.80 \pm 0.20 \pm 0.14)\,\mathrm{GeV}^{-2} \\
\alpha' &= (0.016 \pm 0.151 \pm 0.094)\,\mathrm{GeV}^{-2}
\end{aligned}$$

The result is in very good agreement with the result derived analysing the W dependence of the cross section in bins of t. It is compatible with no shrinkage predicted in [27] for deep inelastic scattering.

As for J/ψ photoproduction cross section a two-dimensional fit is performed analysing the W and t dependence simultaneously. The fit leads to the following values:

$$\begin{aligned}
b(90\,\mathrm{GeV}) &= (3.86 \pm 0.20 \pm 0.14)\,\mathrm{GeV}^{-2} \\
\alpha' &= (0.018 \pm 0.103 \pm 0.064)\,\mathrm{GeV}^{-2} \\
\alpha_0 &= 1.181 \pm 0.045 \pm 0.029
\end{aligned}$$

The errors are slightly reduced compared to the one-dimensional fits.
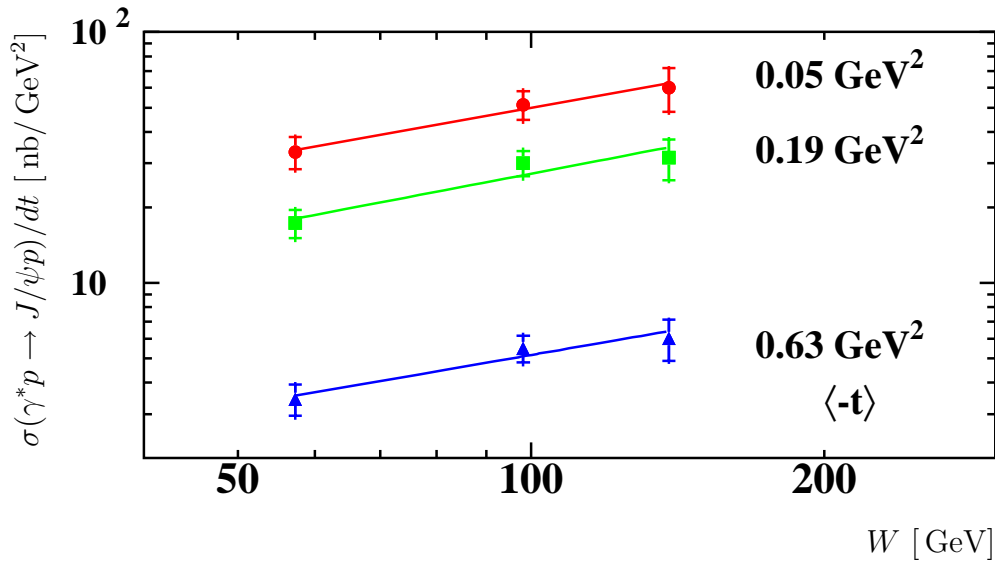
Figure 5.23: Differential cross section for elastic J/ψ electroproduction as a function of W in three bins of t at $\langle Q^2 \rangle = 8.9\,\text{GeV}^2$. The mean value $\langle -t \rangle$ of each bin is given on the right hand side of the figure. The inner error bars indicate the statistical error, while the outer bars show the statistical and systematic uncertainties added in quadrature. The solid lines show the result of fits of the form $d\sigma^{\text{el}}_{\gamma^* p}/dt \propto (W/90\,\text{GeV})^{4(\alpha(t)-1)}$ to the data.

t	$\alpha(t)$
$[\,\text{GeV}^2]$	
0.00-0.08	$1.17 \pm 0.06 \pm 0.04$
0.08-0.30	$1.19 \pm 0.05 \pm 0.04$
0.30-1.20	$1.17 \pm 0.06 \pm 0.04$

Table 5.6: Effective Pomeron trajectory $\alpha(t)$ measured in three bins of t for elastic J/ψ electroproduction for $2\,\text{GeV}^2 < Q^2 < 80\,\text{GeV}^2$ and $40\,\text{GeV} < W < 160\,\text{GeV}$.

W	$b_{\text{el}}(W)$
$[\,\text{GeV}]$	GeV^{-2}
40- 80	$3.77 \pm 0.34 \pm 0.23$
80-120	$3.79 \pm 0.29 \pm 0.22$
120-160	$3.84 \pm 0.45 \pm 0.23$

Table 5.7: Slope parameter $b_{\text{el}}(W)$ measured in three bins of W for elastic J/ψ electroproduction for $2\,\text{GeV}^2 < Q^2 < 80\,\text{GeV}^2$ and $40\,\text{GeV} < W < 160\,\text{GeV}$.
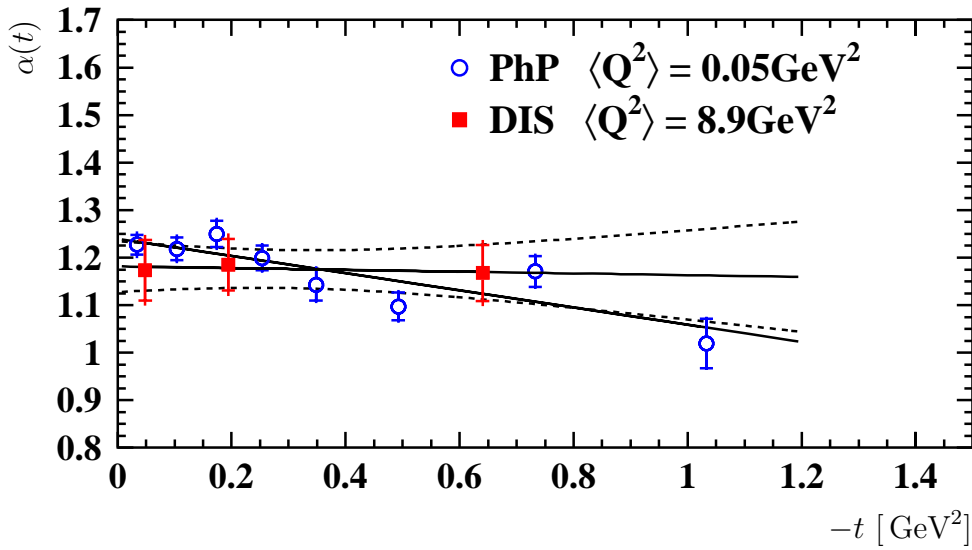
Figure 5.24: Effective Pomeron trajectory α as a function of t. Shown are the results for J/ψ photoproduction (PhP) in comparison with the result in deep inelastic scattering (DIS). The inner error bars indicate the statistical error, while the outer bars show the statistical and systematic uncertainties added in quadrature. The solid lines show the results of linear fits to the data. The dashed lines show the 1σ error band for the DIS data taking the correlation coefficients of the fit parameters into account.
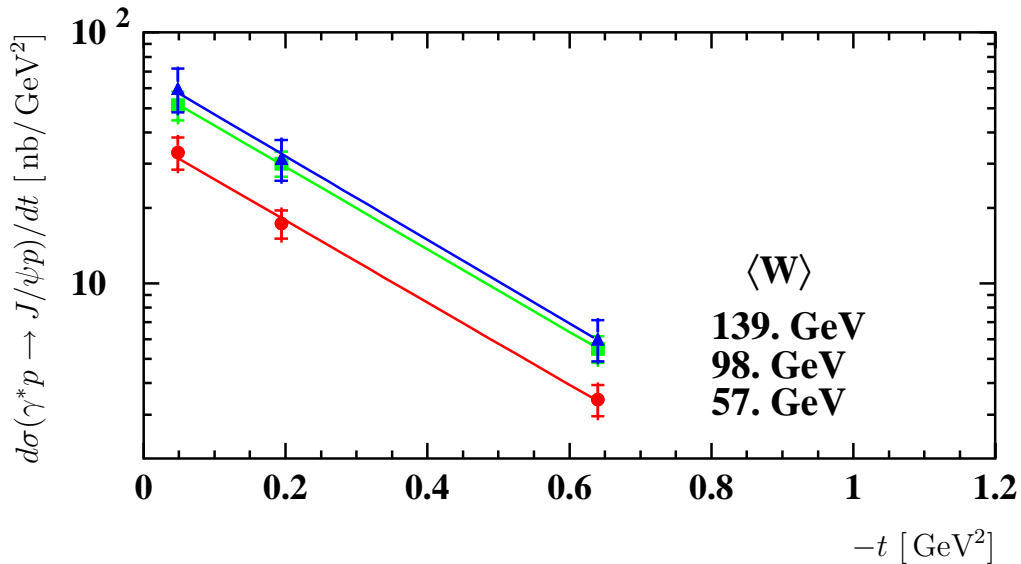
Figure 5.25: Differential cross section for elastic J/ψ electroproduction as a function of t in three bins of W at $\langle Q^2 \rangle = 8.9\,\text{GeV}^2$. The mean value $\langle W \rangle$ of each bin is given on the right hand side of the plot. The inner error bars indicate the statistical error, while the outer bars show the statistical and systematic uncertainties added in quadrature. The solid lines show the result of fits of the form $d\sigma/dt \propto e^{b(W)t}$ to the data.
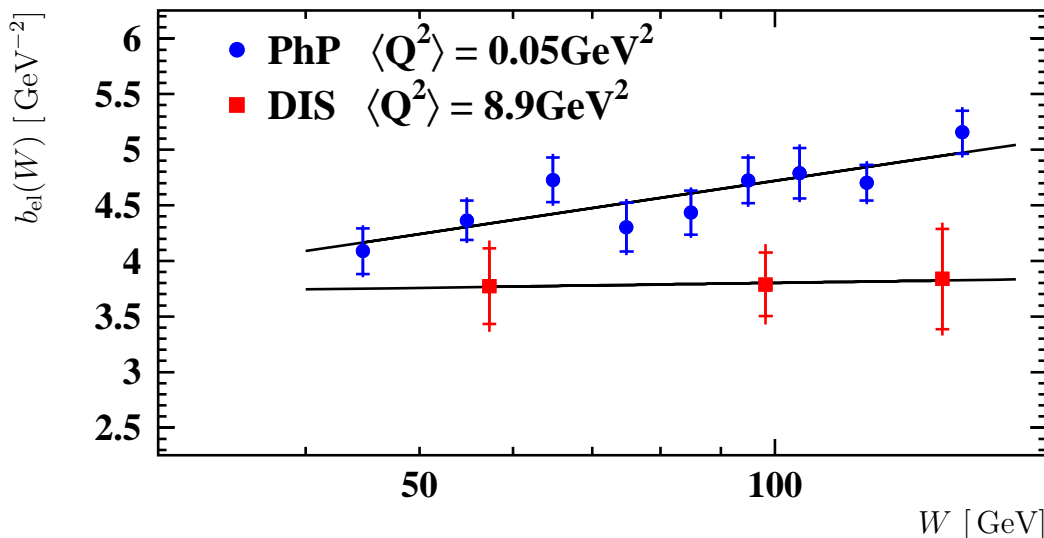
Figure 5.26: Slope parameter b_{el} as a function of W. Shown are the results for J/ψ photoproduction (PhP) in comparison with the result in deep inelastic scattering (DIS). The inner error bars indicate the statistical error, while the outer bars show the statistical and systematic uncertainties added in quadrature. The solid lines show the results of fits of the form $b_{el}(W) = b(90\,\text{GeV}) + 4\alpha' \ln(W/90\,\text{GeV})$.

5.3 Helicity Structure

In this section the helicity structure of diffractive J/ψ photoproduction and electroproduction is analysed. No difference in the structure is expected for elastic and proton dissociative diffractive J/ψ production. Therefore, in order to increase the statistics, the diffractive cross section is analysed calculating the combined cross sections according to equation (4.1) without separation of tagged and untagged events. This also reduces the systematic uncertainties, because the uncertainty on the separation of elastic and proton dissociative events given in table 4.2 does not affect the result. Therefore total systematic uncertainties of 7.1% and 8.1% are used for J/ψ photoproduction and electroproduction respectively. All results have been verified using just the elastic cross sections and no differences have been found within the statistical errors.

The three decay angles introduced in section 1.3 are measured and spin density matrix elements are extracted from fits to the differential cross sections. The results are compared to theoretical predictions for s-channel helicity conservation (SCHC).

Figure 5.27 shows the total efficiencies derived for the combined data sets of tagged and untagged events for the year 2000. Shown are the efficiencies for J/ψ photoproduction and electroproduction as a function of $\cos\theta^*$, ϕ^* and Ψ.

The $\cos\theta^*$ distribution of the beam-sign daughter muon in the J/ψ rest frame is analysed first. The cross section is predicted as follows:

$$\frac{d\sigma}{d\cos\theta^*} \propto 1 + r_{00}^{04} + \left(1 - 3r_{00}^{04}\right)\cos^2\theta^* \tag{5.5}$$
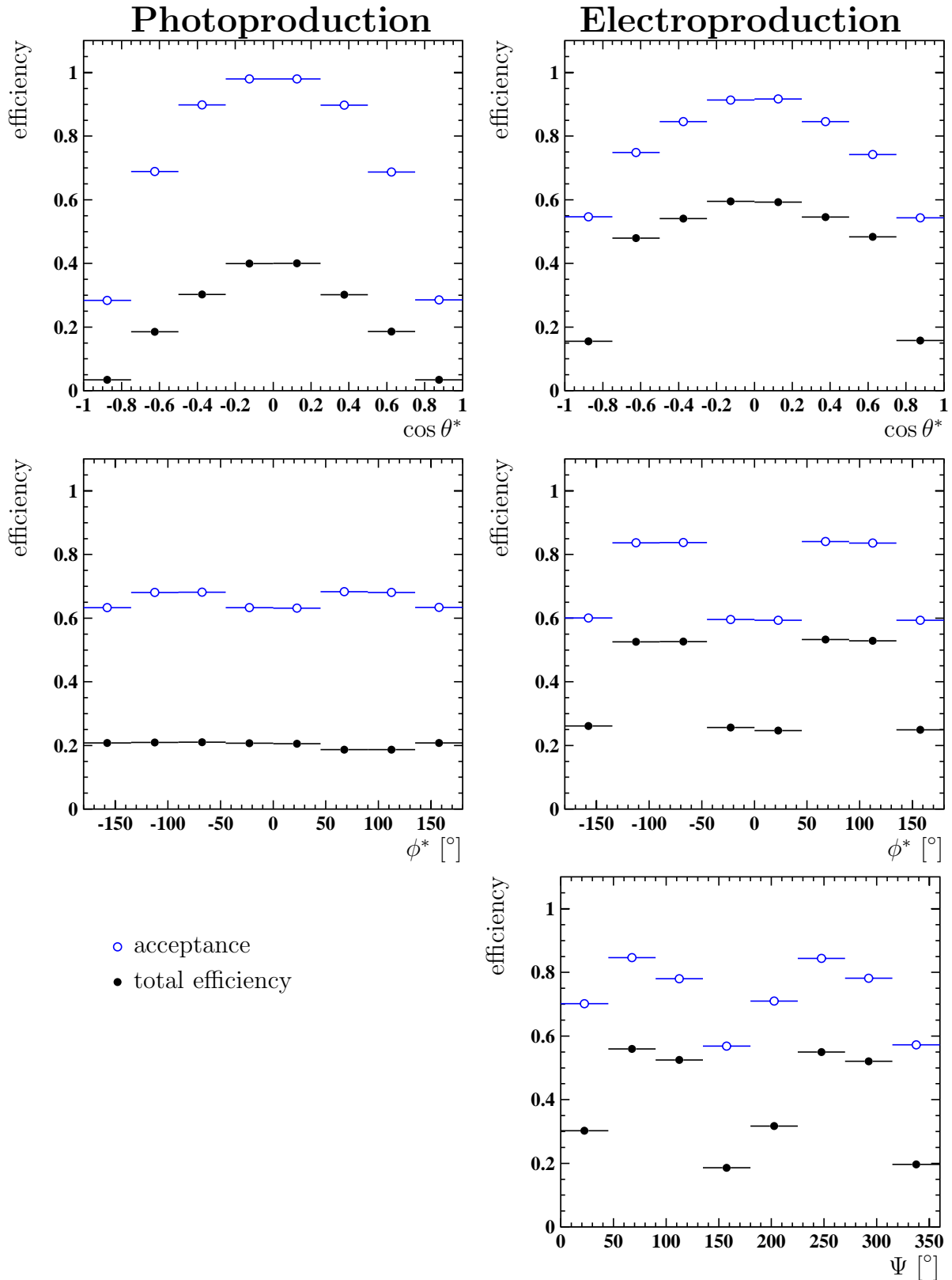
Figure 5.27: Total efficiency of the year 2000 as a function of $\cos\theta^*$, ϕ^* and Ψ derived for the combined data sample using tagged and untagged events. The left column shows the results for the photoproduction and the right column for the regime of deep inelastic scattering.

Figure 5.28 shows the differential cross section $d\sigma/d\cos\theta^*$ as a function of $\cos\theta^*$ in four bins of Q^2. The first region $\langle Q^2 \rangle = 0.05\,\text{GeV}^2$ corresponds to the photoproduction sample, while the other three use the data sample for deep inelastic scattering. The solid curves show the results of fitting equation (5.5) to the data. The extracted values for the spin density matrix element r_{00}^{04} are listed in table 5.8.

In the case of SCHC $r_{00}^{04} = 0$ is expected for the limit $Q^2 \to 0\,\text{GeV}^2$. The data support this assumption. Therefore the matrix element can be used to determine the ratio R of the longitudinal to transversely polarised cross sections.

$$R = \frac{1}{\varepsilon} \frac{r_{00}^{04}}{1 - r_{00}^{04}}$$

ε is defined by equation (1.14) and in the kinematic range of this analysis $\langle \varepsilon \rangle = 0.993$. The corresponding values of R (see table 5.8) are shown as a function of Q^2 in figure 5.29. In addition the published results from H1 [116] and preliminary results from ZEUS [117] are shown. Calculations in pQCD predict a Q^2 dependence of R of the form [20]

$$R = \xi \frac{Q^2}{M_\psi^2}.$$

The solid line in figure 5.29 shows the result of a fit to the data of this analysis yielding $\xi = 0.27 \pm 0.20$. Also two QCD predictions are shown in the figure. The dashed curve shows a prediction from Martin et al. [20], which is somewhat steeper than the data. In addition there is the prediction from Hayashigaki et al. [31], taking Fermi motion effects into account, which gives a reasonable description of the data.

The extracted values of R are used to derive the cross sections for transversely and longitudinally polarised virtual photons using equation (1.13) and (1.15):

$$\sigma_{\gamma^*p} = \sigma_{\gamma^*p}^T + \varepsilon\sigma_{\gamma^*p}^L \qquad \text{and} \qquad R = \frac{\sigma_{\gamma^*p}^L}{\sigma_{\gamma^*p}^T}$$

The resulting values for $\sigma_{\gamma^*p}^L$ and $\sigma_{\gamma^*p}^T$ are displayed in figure 5.30. The transverse component dominates at $Q^2 \approx 0\,\text{GeV}^2$ and decreases with increasing Q^2, while $\sigma_{\gamma^*p}^L$ is more or less constant and very small.

As in section 5.2.1 a fit[1] to the data of the form $\sigma_{\gamma^*p} \propto (M_\psi^2 + Q^2)^{-n}$ is performed. For the transversely polarised photons the fit yields

$$n^T = 2.89 \pm 0.24 \pm 0.15$$

while for $\sigma_{\gamma^*p}^L$

$$n^L = 0.28 \pm 0.75 \pm 1.75.$$

The extracted value for n^T is within errors in agreement with the result $n = 2.460 \pm 0.080 \pm 0.048$ obtained for the combined cross section. Due to the size of the errors no statement about n^L is possible.

---

[1]see footnote 1 on page 73
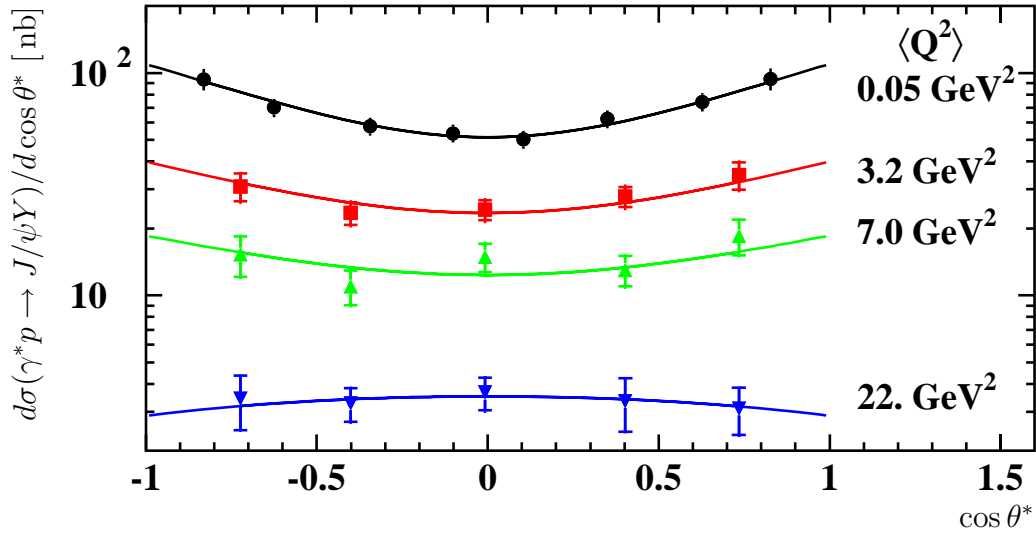
Figure 5.28: Differential cross section for diffractive J/ψ production as a function of $\cos\theta^*$ in four bins of Q^2. The mean value $\langle Q^2 \rangle$ is given on the right hand side of the figure. The first bin corresponds to J/ψ photoproduction, while the others use the data sample for deep inelastic scattering. The solid curves show the results of fits of the form $d\sigma/d\cos\theta^* \propto 1 + r_{00}^{04} + \left(1 - 3r_{00}^{04}\right)\cos^2\theta^*$.

$\langle Q^2 \rangle$	r_{00}^{04}	r_{1-1}^{04}	R
0.05	-0.03±0.02±0.05	0.00±0.02±0.05	-0.03±0.02±0.05
3.2	0.08±0.11±0.07	-0.25±0.11±0.06	0.09±0.13±0.08
7.0	0.14±0.17±0.08	-0.41±0.16±0.06	0.16±0.23±0.11
22.0	0.42±0.21±0.08	-0.44±0.14±0.05	0.73±0.63±0.21

Table 5.8: Results of the decay angle analysis. The first error is the resulting error performing the fits to the data using the statistical errors only. The second error gives the systematic uncertainty. r_{00}^{04} and r_{1-1}^{04} are elements of the spin density matrix extracted as described in the text. $R = \sigma_L/\sigma_T$ is the ratio of the longitudinal to the transverse cross section derived from the matrix element r_{00}^{04}.
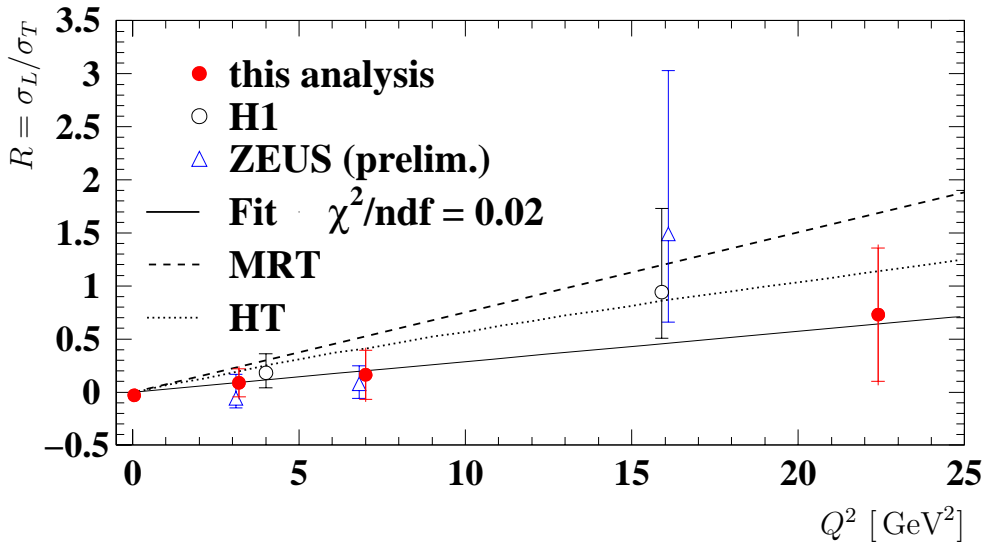
Figure 5.29: Ratio of the longitudinal to the transverse cross section as a function of Q^2. For comparison the published results from H1 [116] and preliminary results from ZEUS [117] are also shown. The solid curve shows a fit to the data of this analysis of the form $R = \xi(Q^2/M_\psi^2)$. The dashed curve shows the prediction of Martin et al. [20], while the dotted line corresponds to the prediction of Hayashigaki et al. [31].
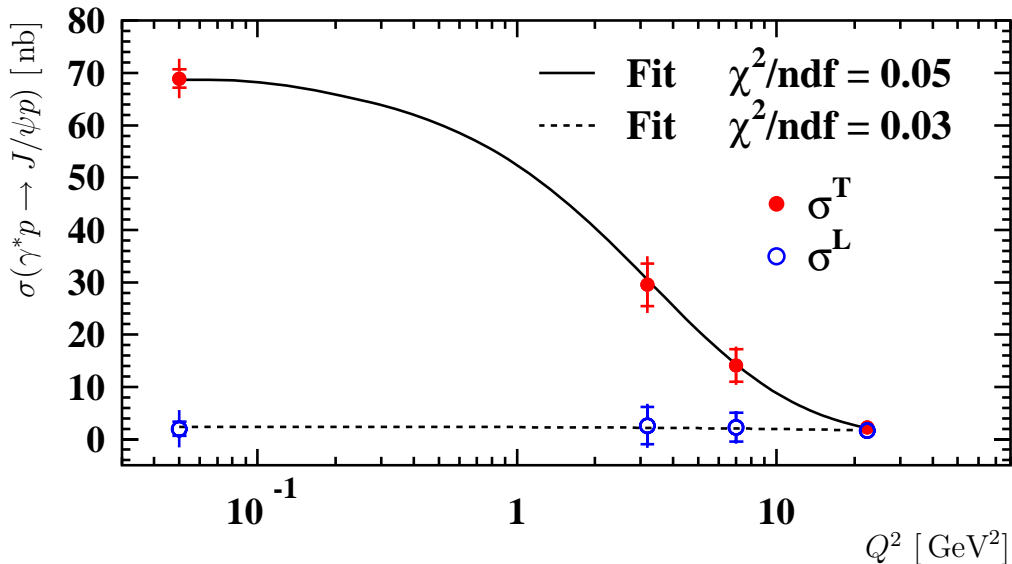
Figure 5.30: Elastic cross section for elastic J/ψ production by transversely (σ^T) and longitudinally (σ^R) polarised virtual photons as a function of Q^2. The inner error bars show the statistical errors only, while the outer error bars show the statistical errors and the systematic uncertainties added in quadrature. Fits of the form $(Q^2 + M_\psi^2)^{-n}$ yield $n^T = 2.89 \pm 0.24 \pm 0.15$ and $n^L = 0.28 \pm 0.75 \pm 1.75$.

$\langle Q^2 \rangle$	r^1_{1-1}	$\Delta(r^1_{1-1}, r^{04}_{00})$
3.2	$0.18\pm0.10\pm0.06$	$-0.28\pm0.15\pm0.10$
7.0	$0.29\pm0.15\pm0.06$	$-0.14\pm0.23\pm0.10$
22.0	$0.24\pm0.17\pm0.07$	$0.05\pm0.27\pm0.12$

Table 5.9: Results of the decay angle analysis for deep inelastic scattering. The first error is the resulting error performing the fits to the data using the statistical errors only. The second error gives the systematic uncertainty. r^1_{1-1} is an elements of the spin density matrix extracted as described in the text. Δ defined by equation (5.7) is the result of a comparison of the two matrix elements r^{04}_{00} and r^1_{1-1}. In the case of SCHC $\Delta = 0$ is expected.

The second angle analysed is ϕ^* which is the angle between the J/ψ production plane and the decay plane in the $\gamma^* p$ centre-of-mass frame. The cross section is described by

$$\frac{d\sigma}{d\phi^*} \propto 1 + r^{04}_{1-1} \cos(2\phi^*) \tag{5.6}$$

where in the case of SCHC $r^{04}_{1-1} = 0$ is expected for all Q^2. Figures 5.31 and 5.32 show the differential cross section $d\sigma/d\phi^*$ as a function of ϕ^* in four bins of Q^2 ranging from photoproduction to larger values of Q^2.

In figure 5.31 the solid curves show the results for fitting the data with equation (5.6). The extracted values of the parameter r^{04}_{1-1} are listed in table 5.8. For J/ψ photoproduction the data support the assumption of SCHC, while with increasing Q^2 smaller values of r^{04}_{1-1} are observed. In a similar analysis of elastic ρ electroproduction [52] the results for r^{04}_{1-1} are all compatible with zero, while other violations of SCHC were found there.

In figure 5.32 the data are fitted by a constant, corresponding to $r^{04}_{1-1} = 0$ (SCHC). In both figures the values χ^2/ndf describing the quality of the fits are given. In the case of J/ψ electroproduction the fits using equation (5.6) yield lower values of χ^2/ndf.

The third angle analysed is $\Psi = \phi^* - \Phi$, where Φ is the angle between the scattering plane of the beam lepton and the J/ψ production plane. This angle can only be measured in the region of deep inelastic scattering where the scattered positron is observed. The data are shown in figure 5.33 and are fitted by:

$$\frac{d\sigma}{d\Psi} \propto 1 - \varepsilon r^1_{1-1} + \cos(2\Psi)$$

where ε is defined as before. The values for the fit parameter r^1_{1-1} are given in table 5.9. In the case of SCHC the two spin density matrix elements r^{04}_{00} and r^1_{1-1} are related by $2r^1_{1-1} = 1 - r^{04}_{00}$. Table 5.9 shows the results of the difference

$$\Delta = r^1_{1-1} - \frac{1}{2}(1 - r^{04}_{00}) \tag{5.7}$$

obtained from the extracted values of r^{04}_{00} and r^1_{1-1} in each Q^2 region. All values of Δ are compatible with zero and therefore with SCHC within the rather large errors.
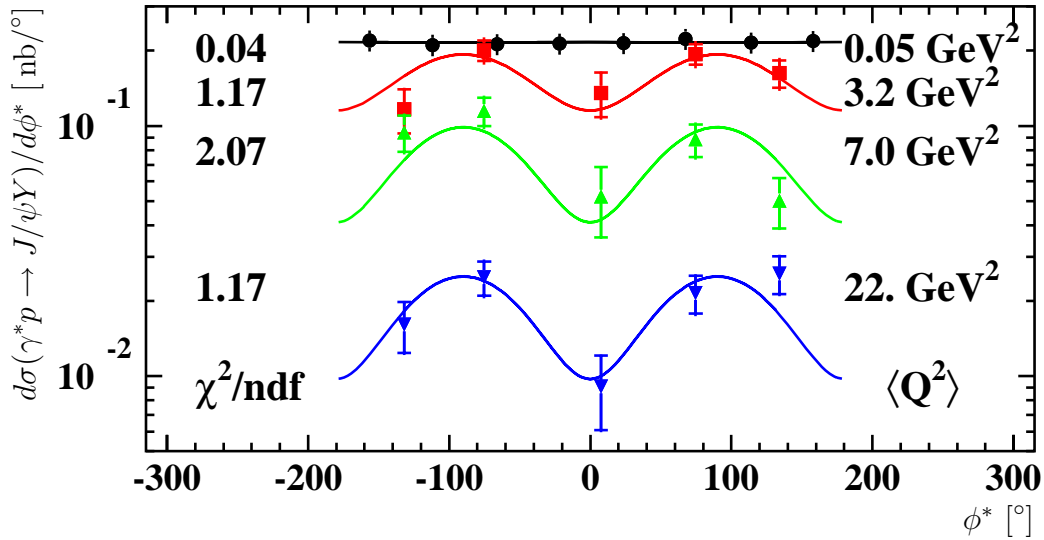
Figure 5.31: Differential cross section for diffractive J/ψ production as a function of the decay angle ϕ^* in four bins of Q^2. The mean value $\langle Q^2 \rangle$ is given on the right hand side of the figure. The first bin corresponds to J/ψ photoproduction, while the others use the data sample for deep inelastic scattering. The solid curves show the results of fits of the form $d\sigma/d\phi^* \propto 1 + r_{1-1}^{04} \cos(2\phi^*)$. On the left hand side of the figure the values χ^2/ndf of the fits are given.
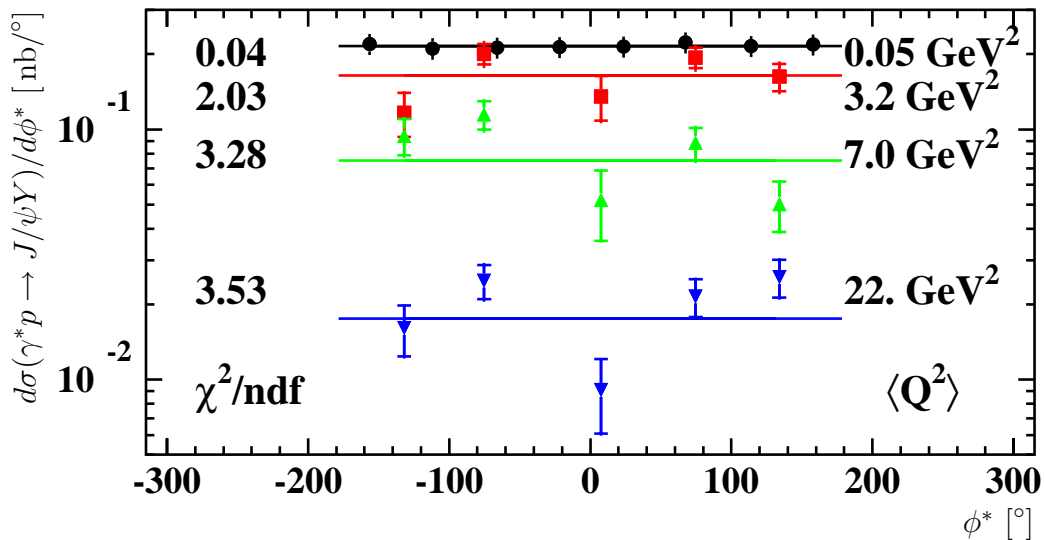
Figure 5.32: Differential cross section for diffractive J/ψ production as a function of the decay angle ϕ^* in four bins of Q^2. The same data as in figure 5.31 are shown. The solid curves show the results of fits of constants to the data. On the left hand side of the figure the values χ^2/ndf of the fits are given.
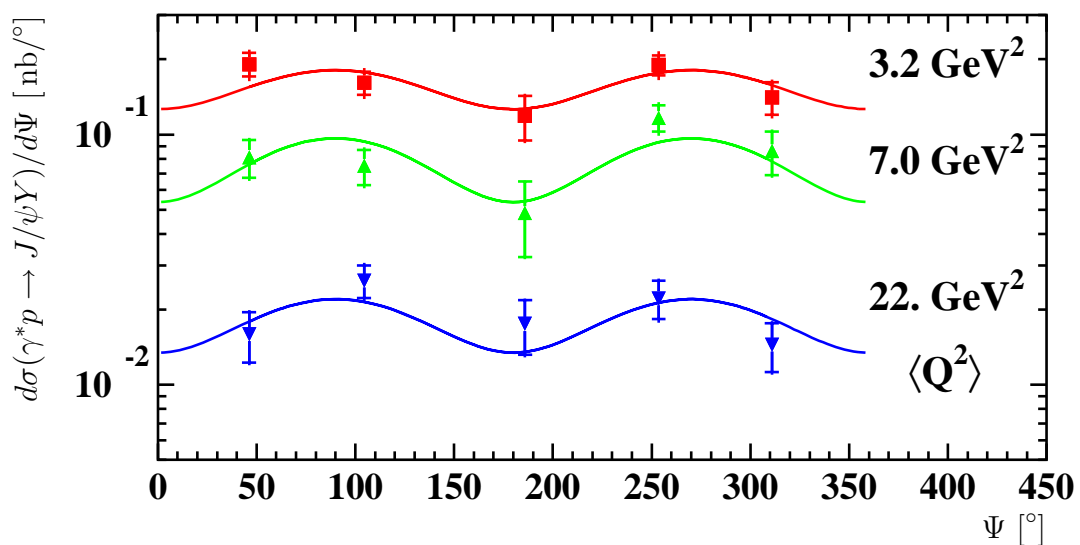
Figure 5.33: Differential cross section for diffractive J/ψ electroproduction as a function of the decay angle Ψ in three bins of Q^2. The mean value $\langle Q^2 \rangle$ is given on the right hand side of the figure. The solid curves show the results of fits of the form $d\sigma/d\Psi \propto 1 - \varepsilon r^1_{1-1} + \cos(2\Psi)$.

Summary and Conclusions

In this thesis the elastic J/ψ production in photoproduction ($Q^2 < 1\,\mathrm{GeV}^2$) and deep inelastic scattering ($2\,\mathrm{GeV}^2 < Q^2 < 80\,\mathrm{GeV}^2$) was studied. The data have been collected with the H1 detector at the ep-collider HERA during the years 1999 and 2000. The analysed data correspond to an integrated luminosity of $54.79\,\mathrm{pb}^{-1}$. The J/ψ mesons have been identified using the decay into a pair of muons. Two data samples have been selected in the kinematic range of $40\,\mathrm{GeV} < W < 160\,\mathrm{GeV}$ and $-t < 1.2\,\mathrm{GeV}^2$ according to the photon virtuality Q^2. The number of elastic J/ψ candidates has been derived using events without activity in the forward region of the detector only and correcting for remaining proton dissociation. Only for the study of the helicity structure of J/ψ production the inclusive cross section has been analysed to increase statistics and reduce the systematic uncertainties.

In this analysis an effort has been made to increase the statistics compared to previous analyses in addition to the increase of the integrated luminosity. Therefore only one of the two decay muons has been required to be identified as a muon leading to an increase of the data sample of $\sim 50\%$. Also the selection cuts to reduce the background from cosmic ray muons have been revised increasing the data samples by $\sim 2\%$. In total about 5800 signal events in the region of photoproduction and about 550 events in the deep inelastic scattering sample have been selected.

The selected data have been compared in detail to a Monte Carlo simulation, in order to verify the selection and detector efficiencies implemented in the simulation. Where necessary, the MC simulation has been corrected for efficiencies of the muon identification, the triggers and the forward tagging. With the increased statistics a more detailed study of the muon identification in the Liquid Argon Calorimeter and the Central Muon Detector in the polar angular range $20° < \theta_\mu < 160°$ has been achieved. With this improved description of the muon identification the corresponding systematic uncertainty has been reduced from $\sim 5\%$ to $\sim 1.5\%$. The correction procedure for the description of the forward tagging follows a slightly different way compared to previous analysis, but is compatible in the final result. The resulting total systematic uncertainties have been estimated to be 8.8% and 9.6% for J/ψ photoproduction and electroproduction respectively.

The elastic γp photoproduction cross section shows a steep rise with the centre-of-mass energy W. Taking only the uncorrelated systematic errors into account the fit W^δ to the data yields a value of $\delta = 0.71 \pm 0.04 \pm 0.07$, where the second error is systematic. This value is in good agreement with previous analyses from H1 and ZEUS. In terms of Regge formalism this rise cannot be described by the soft Pomeron alone. An additional

hard Pomeron is necessary which however fails to describe the fixed target data at low centre-of-mass energy.

In QCD the steep rise results from the dependence of the cross section on the gluon density. Predictions using pQCD calculations are able to describe the rise well, while the normalisation also depends on non-perturbative effects and is more uncertain.

The t dependence of the elastic cross section has been measured and in the region considered ($-t < 1.2\,\mathrm{GeV}^2$) is well described by a simple exponential ansatz $d\sigma/dt \propto e^{bt}$ with a value of $b = 4.57 \pm 0.07 \pm 0.14\,\mathrm{GeV}^{-2}$. This value is again in good agreement with previous measurements. In some pQCD calculations a contribution from a two-gluon form factor is predicted. A fit taking only this two-gluon form factor into account yields a worse description of the data, while the convolution with the exponential behaviour describes the data well.

In the photoproduction region the effect of shrinkage has been observed. Studying the W and t dependence of the cross section simultaneously revealed an effective Pomeron trajectory with intercept $\alpha_0 = 1.239 \pm 0.013 \pm 0.009$ and slope $\alpha' = 0.177 \pm 0.034 \pm 0.017\,\mathrm{GeV}^{-2}$. These values are in agreement with previous results from H1 and ZEUS and show a smaller slope than for the standard Regge soft Pomeron. The same two-dimensional fit shows a W-dependence of the b slope with $b(90\,\mathrm{GeV}) = 4.663 \pm 0.066 \pm 0.038\,\mathrm{GeV}^{-2}$. The value of $b(90\,\mathrm{GeV})$ is slightly higher than the value published by ZEUS, but agrees within errors. It is in good agreement with previous measurements from H1.

In a second part of this analysis the elastic diffractive production of J/ψ mesons in deep inelastic scattering has been studied. The Q^2 dependence of the elastic cross section has been measured and found to be described by $\sigma_{\gamma p} \propto (M_\psi^2 + Q^2)^{-n}$ with $n = 2.46 \pm 0.08 \pm 0.05$ taking the photoproduction data into account. The W dependence has been found to be similar to the one in photoproduction yielding $\delta = 0.78 \pm 0.15 \pm 0.09$. The t dependence of the elastic differential cross section $d\sigma/dt$ shows a tendency towards lower values of b with increasing photon virtuality Q^2. For $2\,\mathrm{GeV}^2 < Q^2 < 80\,\mathrm{GeV}^2$ $b = 4.10 \pm 0.16 \pm 0.20\,\mathrm{GeV}^{-2}$ has been measured.

In this analysis the effective Pomeron trajectory has been measured for the first time in the region of deep inelastic scattering using the H1 detector. The Pomeron intercept has been found to be $\alpha_0 = 1.18 \pm 0.05 \pm 0.03$ and slope $\alpha' = 0.02 \pm 0.10 \pm 0.06\,\mathrm{GeV}^{-2}$. This result is compatible with no shrinkage at high photon virtualities, but due to the size of the errors it is also compatible with the result in photoproduction. The W dependence of the slope parameter b was observed with α' as above and $b(90\,\mathrm{GeV}) = 3.80 \pm 0.20 \pm 0.14\,\mathrm{GeV}^{-2}$, which is more than three standard deviations lower than the photoproduction result.

In both kinematic regions the helicity structure of the diffractive J/ψ production has been analysed using the cross sections for the combined elastic and the proton dissociative production. The three spin density matrix elements r_{00}^{04}, r_{1-1}^{04} and r_{1-1}^{1} have been extracted. All results support the assumption of s-channel helicity conservation in the regime of photoproduction, while with increasing Q^2 small deviations are visible. Using the matrix element r_{00}^{04} the ratio of the longitudinal to the transverse cross section R has been derived and found to be in good agreement with previous measurements from H1 and ZEUS.

Finally it can be summarised that the photoproduction analysis has confirmed previous measurements with increased statistics and reduced statistical and systematic uncertainties. The analysis in the region of deep inelastic scattering could be extended compared to previous analyses, because of the increased statistics. Nevertheless the statistical errors are still dominant for the measurement of the J/ψ electroproduction.

There are several ways to improve the results on the elastic J/ψ production. First of all the J/ψ decay into an electron-positron pair can be analysed leading to an increase of the statistics by a factor of < 2. For the J/ψ photoproduction analysis, this would not lead to large improvements, because in this kinematic region the systematic uncertainties are of the same order as the statistical errors. In the region of deep inelastic scattering however such an increase in statistics will improve the analysis.

Another way to improve the results is to extend the kinematic region by including larger values of W. In the region of large W the decay leptons cannot both be detected as tracks in the central tracker. The decay of J/ψ mesons into e^+e^--pairs is used and the e^+ and e^- are observed as energy clusters in the backward calorimeter. Most notably the measurement of the effective Pomeron trajectory would benefit from such an increase in W.

During the data taking of HERA II a general increase of statistics is expected due to increased luminosity.

A Run Selection

In the following table the run ranges of the three data taking periods are given. Also a list of all runs manually excluded is given together with a short comment on the reason.

first run-last run	comment
231721-241649	**1999** e^-
232050- 232050	LAr event mixing
233881- 233881	LAr event mixing
235158- 235216	zVtx-trigger not loaded
236542- 236553	LAr Calo & triggers shifted 8 nsec
244968-259461	**1999** e^+
244968- 246605	major problems with L4
246721- 247667	zVtx_Cls broken
249723- 249740	problem unknown
250688- 251871	problems with zVtx_Cls on L2 and missing TB7
250909- 250914	problem unknown
251468- 251471	problem unknown
251926- 251999	problem unknown
252007- 252010	problem unknown
254291- 254308	wrong L2TT setting
	$\rightarrow$ rejecting all Triggers validated by L2TT
256687- 262144	FT switched off
257601- 259461	wire in CJC1 broken
262204-279215	**2000** e^+
262204- 262144	wire in CJC1 broken
263235- 263235	L2 & L4 transparent
263620- 263620	problem unknown
263649- 263673	large PRT noise
263741- 263741	problem unknown
263793- 263793	L4 transparent
264773- 264773	L4 transparent
264974- 265366	large FMD noise
265404- 265888	large PRT noise
265427- 265428	no FMD readout
265572- 265572	lumi cableing problem
265582- 265596	no FMD readout

first run-last run	comment
265599- 265599	no FMD readout
265602- 265604	no FMD readout
265650- 265692	FMD and forward tracker problems
265705- 265707	no FMD readout
266497- 266838	no FMD readout
266885- 266921	large PRT noise
267255- 267255	problem unknown
267262- 267262	problem unknown
267507- 268060	problem unknown
267604- 267604	no FMD readout
267616- 267616	no FMD readout
267890- 267890	problem unknown
268104- 268104	problem unknown
268277- 268277	problem unknown
268325- 268325	noisy Mu_Bar
268420- 268420	noisy Mu_Bar
268423- 268423	no FMD readout
268607- 268607	L4 transparent
268673- 268674	L4 transparent
268955- 268955	noisy Mu_ECQ
268962- 268962	noisy Mu_ECQ
269297- 269297	noisy Mu_Bar
269315- 269315	noisy Mu_Bar
269318- 269318	noisy Mu_ECQ
269360- 269360	no FMD readout
269398- 269398	noisy Mu_Bar
269413- 269416	no FMD readout
269425- 269425	no FMD readout
269430- 269430	no FMD readout
269760- 269760	L2 & L4 transparent
270145- 270145	L4 transparent
270443- 270446	no FMD readout
270506- 270506	no FMD readout
270625- 270632	no FMD readout
270635- 270661	no FMD readout
270667- 270696	no FMD readout
270986- 270987	noisy Mu_ECQ
270989- 270993	noisy Mu_ECQ
270995- 270996	noisy Mu_ECQ
271002- 271002	noisy Mu_ECQ
271037- 271037	noisy Mu_ECQ
271047- 271049	noisy Mu_ECQ
271054- 271057	noisy Mu_ECQ
271880- 271880	no FMD readout

first run-last run	comment
271966- 271966	no FMD readout
	and L2 & L4 transparent
272122- 272352	L2NN not working
272447- 272451	no FMD readout
272459- 272461	no FMD readout
272469- 272469	no FMD readout
272687- 272687	noisy Mu_Bar
272695- 272695	noisy Mu_Bar
272722- 272722	noisy Mu_Bar
272744- 272744	noisy Mu_Bar
272765- 272765	noisy Mu_Bar
273038- 273038	no FMD readout
273164- 273165	no FMD readout
273170- 273171	no FMD readout
273173- 273173	no FMD readout
273182- 273182	no FMD readout
273193- 273193	no FMD readout
273236- 273236	no FMD readout
273241- 273241	no FMD readout
273245- 273246	no FMD readout
273330- 273333	no FMD readout
273400- 273401	no FMD readout
274095- 274095	L2 & L4 transparent
274595- 274623	no FMD readout
275248- 275248	L4 transparent
275301- 275301	L4 transparent
275607- 275730	L2NN not working
275979- 275986	no FMD readout
277751- 277751	noisy Mu_ECQ
278010- 278012	L2 & L4 transparent
278014- 278014	L2 & L4 transparent
278035- 278035	L4 transparent
278066- 278066	L2 & L4 transparent
278225- 278226	L2 & L4 transparent
278686- 278979	shifted vertex
278695- 278695	L4 transparent
278997- 278997	noisy Mu_ECQ
279005- 279005	noisy Mu_ECQ
279046- 279046	no FMD readout
	and L2 & L4 transparent

Bibliography

[1] J.J.Aubert et al., *Experimental observation of a heavy particle J*, Phys. Rev. Lett. **33**, 1404 (1974).

[2] J.E.Augustin et al., *Discovery of a Narrow Resonance in e^+ e^- Annihilation*, Phys. Rev. Lett. **33**, 1406 (1974).

[3] K.Hagiwara et al., *Review of Particle Physics*, Physical Review D **66** (2002).

[4] J.J.Sakurai, *Vector meson dominance and high-energy electron proton inelastic scattering*, Phys. Rev. Lett. **22**, 981 (1969).

[5] J.J.Sakurai and D.Schildknecht, *Generalized vector dominance and inelastic electron - proton scattering*, Phys. Lett. **B40**, 121 (1972).

[6] T.H.Bauer, R.D.Spital, D.R.Yennie and F.M.Pipkin, *The Hadronic Properties of the Photon in High-Energy Interactions*, Rev. Mod. Phys. **50**, 261 (1978).

[7] G.A.Schuler and T.Sjöstrand, *Towards a complete description of high-energy photoproduction*, Nucl. Phys. **B407**, 539 (1993).

[8] T.Regge, *Introduction to complex orbital momenta*, Nuovo Cim. **14**, 951 (1959).

[9] T.Regge, *Bound states, shadow states and Mandelstam representation*, Nuovo Cim. **18**, 947 (1960).

[10] J.J.Sakurai, *Theory of strong interactions*, Annals Phys. **11**, 1 (1960).

[11] P.D.B.Collins, *An Introduction to Regge Theory and High Energy Physics* (Cambridge University PRess, 1977).

[12] M.G.Ryskin, *Diffractive J/ψ electroproduction in LLA QCD*, Z. Phys. **C57**, 89 (1993).

[13] S.J.Brodsky, L.Frankfurt, J.F.Gunion, A.H.Mueller and M.Strikman, *Diffractive leptoproduction of vector mesons in QCD*, Phys. Rev. **D50**, 3134 (1994), hep-ph/9402283.

[14] M.G.Ryskin, R.G.Roberts, A.D.Martin and E.M.Levin, *Diffractive J/ψ photoproduction as a probe of the gluon density*, Z. Phys. **C76**, 231 (1997), hep-ph/9511228.

[15] J.C.Collins, D.E.Soper and G.Sterman, *Soft gluons and factorization*, Nucl. Phys. **B308**, 833 (1988).

[16] J.C.Collins, L.Frankfurt and M.Strikman, *Factorization for hard exclusive electro-production of mesons in QCD*, Phys. Rev. **D56**, 2982 (1997), hep-ph/9611433.

[17] L.Frankfurt, W.Koepf and M.Strikman, *Diffractive heavy quarkonium photo- and electroproduction in QCD*, Phys. Rev. **D57**, 512 (1998), hep-ph/9702216.

[18] M.McDermott, L.Frankfurt, V.Guzey and M.Strikman, *Unitarity and the QCD-improved dipole picture*, Eur. Phys. J. **C16**, 641 (2000), hep-ph/9912547.

[19] A.D.Martin and M.G.Ryskin, *The effect of off-diagonal parton distributions in diffractive vector meson electroproduction*, Phys. Rev. **D57**, 6692 (1998), hep-ph/9711371.

[20] A.D.Martin, M.G.Ryskin and T.Teubner, Q^2 *dependence of diffractive vector meson electroproduction*, Phys. Rev. **D62**, 014022 (2000), hep-ph/9912551.

[21] T.Teubner, *Theory of elastic vector meson production*, (1999), hep-ph/9910329.

[22] L.Frankfurt, M.McDermott and M.Strikman, *A fresh look at diffractive J/ψ photoproduction at HERA, with predictions for THERA*, JHEP **03**, 045 (2001), hep-ph/0009086.

[23] L.Frankfurt and M.Strikman, *Two-gluon form factor of the nucleon and J/ψ photoproduction*, Phys. Rev. **D66**, 031502 (2002), hep-ph/0205223.

[24] J.C.Collins, *Proof of factorization for diffractive hard scattering*, Phys. Rev. **D57**, 3051 (1998), hep-ph/9709499.

[25] J.C.Collins, *Factorization in hard diffraction*, J. Phys. **G28**, 1069 (2002), hep-ph/0107252.

[26] D.Y.Ivanov, A.Schäfer, L.Szymanowski and G.Krasnikov, *Exclusive photoproduction of a heavy vector meson in QCD*, (2004), hep-ph/0401131.

[27] J.Bartels and H.Kowalski, *Diffraction at HERA and the confinement problem*, Eur. Phys. J. **C19**, 693 (2001), hep-ph/0010345.

[28] A.H.Mueller and B.Patel, *Single and double BFKL pomeron exchange and a dipole picture of high-energy hard processes*, Nucl. Phys. **B425**, 471 (1994), hep-ph/9403256.

[29] N.Nikolaev and B.G.Zakharov, *The Triple pomeron regime and the structure function of the pomeron in the diffractive deep inelastic scattering at very small x*, Z. Phys. **C64**, 631 (1994), hep-ph/9306230.

[30] N.Nikolaev and B.G.Zakharov, *Pomeron structure function and diffraction dissociation of virtual photons in perturbative QCD*, Z. Phys. **C53**, 331 (1992).

[31] A.Hayashigaki and K.Tanaka, *Transverse quark motion inside charmonia in diffractive photo- and electroproductions*, (2004), hep-ph/0401053.

[32] A.Donnachie and P.V.Landshoff, *Total cross-sections*, Phys. Lett. **B296**, 227 (1992), hep-ph/9209205.

[33] A.Donnachie and P.V.Landshoff, *Soft interactions*, (1997), hep-ph/9703366.

[34] S.Okubo, *Phi meson and unitary symmetry model*, Phys. Lett. **5**, 165 (1963).

[35] J.Iizuka, K.Okada and O.Shito, *Systematics and phenomenology of boson mass levels. 3*, Prog. Theor. Phys. **35**, 1061 (1966).

[36] G.Zweig, *An SU(3) Model for Strong Interaction Symmetry and its breaking*, In *Lichtenberg, D. B. (Ed.), Rosen, S. P. (Ed.): Developments In The Quark Theory Of Hadrons, Vol. 1*, 22- 101 and CERN Geneva - TH. 401 (REC.JAN. 64) 24p.

[37] G.Alberi and G.Goggi, *Diffraction of subnuclear waves*, Phys. Rept. **74**, 1 (1981).

[38] K.Goulianos, *Diffractive interactions of hadrons at high-energies*, Phys. Rept. **101**, 169 (1983).

[39] H1 Collaboration, S.Aid et al., *Measurement of the total photon proton cross section and its decomposition at 200 GeV centre of mass energy*, Z. Phys. **C69**, 27 (1995), hep-ex/9509001.

[40] H1 Collaboration, S.Aid et al., *Elastic photoproduction of ρ^0 Mesons at HERA*, Nucl. Phys. **B463**, 3 (1996), hep-ex/9601004.

[41] H1 Collaboration, S.Aid et al., *Elastic and inelastic photoproduction of J/ψ mesons at HERA*, Nucl. Phys. **B472**, 3 (1996), hep-ex/9603005.

[42] H1 Collaboration, C.Adloff et al., *Elastic photoproduction of J/ψ and Υ mesons at HERA*, Phys. Lett. **B483**, 23 (2000), hep-ex/0003020.

[43] H1 Collaboration, C.Adloff et al., *Diffractive photoproduction of psi(2S) mesons at HERA*, Phys. Lett. **B541**, 251 (2002), hep-ex/0205107.

[44] ZEUS Collaboration, M.Derrick et al., *Measurement of total and partial photon proton cross- sections at 180-GeV center-of-mass energy*, Z. Phys. **C63**, 391 (1994).

[45] ZEUS Collaboration, M.Derrick et al., *Measurement of elastic ρ^0 photoproduction at HERA*, Z. Phys. **C69**, 39 (1995), hep-ex/9507011.

[46] ZEUS Collaboration, M.Derrick et al., *Measurement of elastic ω photoproduction at HERA*, Z. Phys. **C73**, 73 (1996), hep-ex/9608010.

[47] ZEUS Collaboration, M.Derrick et al., *Measurement of the reaction $\gamma^* p \rightarrow \phi p$ in deep inelastic $e^+ p$ scattering at HERA*, Phys. Lett. **B380**, 220 (1996), hep-ex/9604008.

[48] ZEUS Collaboration, J.Breitweg et al., *Measurement of elastic J/ψ photoproduction at HERA*, Z. Phys. **C75**, 215 (1997), hep-ex/9704013.

[49] ZEUS Collaboration, J.Breitweg et al., *Elastic and proton-dissociative ρ^0 photoproduction at HERA*, Eur. Phys. J. **C2**, 247 (1998), hep-ex/9712020.

[50] ZEUS Collaboration, J.Breitweg et al., *Measurement of elastic Υ photoproduction at HERA*, Phys. Lett. **B437**, 432 (1998), hep-ex/9807020.

[51] ZEUS Collaboration, S.Chekanov et al., *Exclusive photoproduction of J/psi mesons at HERA*, Eur. Phys. J. **C24**, 345 (2002), hep-ex/0201043.

[52] H1 Collaboration, C.Adloff et al., *Elastic electroproduction of ρ mesons at HERA*, Eur. Phys. J. **C13**, 371 (2000), hep-ex/9902019.

[53] ZEUS Collaboration, J.Breitweg et al., *Exclusive electroproduction of ρ^0 and J/ψ mesons at HERA*, Eur. Phys. J. **C6**, 603 (1999), hep-ex/9808020.

[54] L.Frankfurt, M.F.McDermott and M.Strikman, *Diffractive photoproduction of Υ at HERA*, JHEP **02**, 002 (1999), hep-ph/9812316.

[55] A.Donnachie and P.V.Landshoff, *Small x: Two pomerons!*, Phys. Lett. **B437**, 408 (1998), hep-ph/9806344.

[56] R.Fiore, L.L.Jenkovszky, F.Paccanoni and A.Prokudin, *The pomeron in exclusive J/ψ vector meson production*, (2003), hep-ph/0305289.

[57] G.A.Schuler and J.Terron, *Elastic and diffractive photoproduction of J/ψ mesons*, CERN-TH-6403-92.

[58] P.Newman, *A study of the dynamics of diffractive photoproduction at HERA*, Dissertation, University of Birmingham, 1996.

[59] F.E.Low, *A model of the bare pomeron*, Phys. Rev. **D12**, 163 (1975).

[60] S.Nussinov, *Colored quark version of some hadronic puzzles*, Phys. Rev. Lett. **34**, 1286 (1975).

[61] L.Frankfurt, W.Koepf and M.Strikman, *Hard diffractive electroproduction of vector mesons in QCD*, Phys. Rev. **D54**, 3194 (1996), hep-ph/9509311.

[62] S.D.Holmes, W.-Y.Lee and J.E.Wiss, *High-Energy Photoproduction of Charmed States*, Ann. Rev. Nucl. Part. Sci. **35**, 397 (1985).

[63] K.Schilling and G.Wolf, *How to analyze vector meson production in inelastic lepton scattering*, Nucl. Phys. **B61**, 381 (1973).

[64] P.Joos et al., *ρ production by virtual photons*, Nucl. Phys. **B113**, 53 (1976).

[65] B.Humpert and A.C.D.Wright, *Does ψ photoproduction conserve helicity?*, Phys. Lett. **B65**, 463 (1976).

[66] B.Humpert and A.C.D.Wright, *Spin and mass dependence of models for ψ photo-production*, Phys. Rev. **D15**, 2503 (1977).

[67] A.R.Clark et al., *Polarisation of Muoproduced J/ψ (3100)*, Phys. Rev. Lett. **45**, 2092 (1980).

[68] I.Royen, *Helicity in diffractive vector meson production*, Phys. Lett. **B513**, 337 (2001), hep-ph/0006044.

[69] J.Meyer et al., *Guide to Simulation Program H1SIM*, Hamburg, 1991.

[70] R.Brun, R.Hagelberg, M.Hansroul and J.C.Lassalle, *GEANT: Simulation Program for Particle Physics Experiments*, User Guide and Reference Manual, CERN-DD-78-2-REV.

[71] B.List and A.Mastroberardino, DIFFVM: A monte carlo generator for diffractive processes in ep scattering, p. 396, 1999, DESY-PROC-1999-02.

[72] S.P.Baranov, O.Dünger, H.Shooshtari and J.A.M.Vermaseren, LPAIR: A generator for lepton pair production, in *Physics at HERA vol.3*, p. 1478, 1991.

[73] A.Kwiatkowski, H.Spiesberger and H.J.Möhring, *HERACLES: An event generator for e p interactions at HERA energies including radiative processes: VERSION 1.0*, Comp. Phys. Commun. **69**, 155 (1992).

[74] X.Janssen, *Electroproduction diffractive de mesons ρ a HERA*, Dissertation, Universite Libre de Bruxelles, 2002.

[75] A.Meyer, *Charmonium Production in Deep Inelastic Scattering at HERA*, Dissertation, Universität Hamburg, 1998.

[76] S.Mohrdieck, *Inelastische J/ψ -Erzeugung in Elektroproduktion am H1-Experiment bei HERA*, Dissertation, Universität Hamburg, 2000.

[77] D.Schmidt, *Diffraktive Photoproduktion von Charmonium im H1-Detektor bei HERA*, Dissertation, Universität Hamburg, 2001.

[78] S.Schiek, *Untersuchung der inelastischen Photoproduktion von J/ψ -Mesonen im H1-Detektor bei HERA*, Dissertation, Universität Hamburg, 1997.

[79] G.Schmidt, *Untersuchung der diffraktiven Photoproduktion von J/ψ -Mesonen im H1-Detektor bei HERA*, Dissertation, Universität Hamburg, 1997.

[80] P.Merkel, *Diffractive Photoproduction of Heavy Vector Mesons at HERA*, Dissertation, Universität Hamburg, 1999.

[81] K.Krüger, *Photoproduction of J/ψ mesons at medium and low elasticities at HERA*, Dissertation, Universität Hamburg, 2001.

[82] H1 Collaboration, I.Abt et al., *The H1 detector at HERA*, Nucl. Instrum. Meth. **A386**, 310 (1997).

[83] H1 Collaboration, I.Abt et al., *The Tracking, calorimeter and muon detectors of the H1 experiment at HERA*, Nucl. Instrum. Meth. **A386**, 348 (1997).

[84] H1 Calorimeter Group, B.Andrieu et al., *The H1 liquid argon calorimeter system*, Nucl. Instrum. Meth. **A336**, 460 (1993).

[85] H1 Calorimeter Group, B.Andrieu et al., *Results from pion calibration runs for the H1 liquid argon calorimeter and comparisons with simulations*, Nucl. Instrum. Meth. **A336**, 499 (1993).

[86] H1 Calorimeter Group, B.Andrieu et al., *Electron / pion separation with the H1 LAr calorimeters*, Nucl. Instrum. Meth. **A344**, 492 (1994).

[87] H1 Calorimeter Group, B.Andrieu et al., *Beam tests and calibration of the H1 liquid argon calorimeter with electrons*, Nucl. Instrum. Meth. **A350**, 57 (1994).

[88] H1 SPACAL Group, R.D.Appuhn et al., *The H1 lead/scintillating-fibre calorimeter*, Nucl. Instrum. Meth. **A386**, 397 (1997).

[89] P.Biddulph et al., *The H1 forward muon spectrometer*, Nucl. Instrum. Meth. **A340**, 304 (1994).

[90] H1 Collaboration, Luminosity Measurement in the H1 Experiment at HERA, in proceedings of *XXVIII ICHEP Warsaw*, 1996.

[91] F.Sefkow, E.Elsen, H.Krehbiel, U.Straumann and J.Coughlan, *Experience with the first level trigger of H1*, IEEE Trans. Nucl. Sci. **42**, 900 (1995).

[92] S.Egli et al., *Calculating Event Weights in Case of Downscaling on Trigger Levels 1-4*, H1 internal note, H1-IN-517(04/1997).

[93] R.Riedlberger, *The H1 trigger with emphasis on tracking triggers*, H1 internal note, H1-IN-419(01/1995).

[94] H.Beck, *Principles and operation of the z-vertex trigger*, H1 internal note, H1-IN-479(05/1996).

[95] V.Boudry et al., *Design and CERN-test results*, H1 internal note, H1-IN-430(03/1995).

[96] T.Nicholls et al., *Concept, design and performance of the second level trigger of the H1 detector*, IEEE Trans. Nucl. Sci. **45**, 810 (1998).

[97] J.C.Bizot et al., *Proposal for a topological level 2 trigger*, H1 internal note, H1-IN-181(06/1991).

[98] L.Goerlich et al., *Strategy Studies for the H1 Topological L2-Trigger (L2TT)*, H1 internal note, H1-IN-508(01/1997).

[99] J.Fent et al., *A Neural Network Second Level Trigger for the H1-Experiment at HERA*, H1 internal note, H1-IN-457(10/1995).

[100] J.Köhne et al., *Realization of a Second Level Neural Network Trigger for the H1 Experiment at HERA*, H1 internal note, H1-IN-509(01/1997).

[101] S.Mohrdieck, *Neuronaler Netzwerk-Trigger fuer Myonen im H1-Detektor bei HERA*, Diploma thesis, Universität Hamburg, 1997.

[102] S.Levonian, *H1 Lumi Summary*, H1 internal information, 2000.

[103] L.West, *How to use the Heavy Flavour Working Group Track, Muon and Electron Selection Code*, H1 internal software manual, 1997.

[104] B.Naroska, S.Schiek and G.Schmidt, *Lepton Identification in the H1 Detector at Low Momenta*, H1 internal note H1-05/97-518, 1997.

[105] F.Jacquet and A.Blondel, in *Proc. of the Study for an ep Facility for Europe*, edited by U.Amaldi, p. 377, 1979, DESY-79-048.

[106] S.Bentvelsen, J.Engelen and P.Kooijman, Reconstruction of (x, q^2) and extraction of structure functions in neutral current scattering at hera, in *Proc. of the workshop 'Physics at HERA', Vol.1*, edited by W.Buchmüller and G.Ingelman, pp. 23–41, 1992.

[107] A.Rostovtsev and V.Soloshenko, *Corrections to the Weizsäcker-Williams Approximation of photon flux in ep collisions*, H1 internal note, H1-IN-309(08/1993).

[108] V.M.Budnev, I.F.Ginzburg, G.V.Meledin and V.G.Serbo, *The Two photon particle production mechanism. Physical problems. Applications. Equivalent photon approximation*, Phys. Rept. **15**, 181 (1974).

[109] A.Schwank, *Effizienzbestimmung von Detektorkomponenten des H1-Experiments mit Hilfe kosmischer Strahlung*, Diploma thesis, Universität Hamburg, 1998.

[110] M.Binkley et al., ***J/ψ** photoproduction from 60 GeV /c to 300 GeV /c*, Phys. Rev. Lett. **48**, 73 (1982).

[111] B.H.Denby et al., *Inelastic and elastic photoproduction of J/ψ (3097)*, Phys. Rev. Lett. **52**, 795 (1984).

[112] H.L.Lai et al., *Improved parton distributions from global analysis of recent deep inelastic scattering and inclusive jet data*, Phys. Rev. **D55**, 1280 (1997), hep-ph/9606399.

[113] CTEQ, H.L.Lai et al., *Global QCD analysis of parton structure of the nucleon: CTEQ5 parton distributions*, Eur. Phys. J. **C12**, 375 (2000), hep-ph/9903282.

[114] A.D.Martin, R.G.Roberts, W.J.Stirling and R.S.Thorne, *Parton distributions: A new global analysis*, Eur. Phys. J. **C4**, 463 (1998), hep-ph/9803445.

[115] M.Strikman, *private communication*, 2004.

[116] H1 Collaboration, C.Adloff et al., *Charmonium production in deep inelastic scattering at HERA*, Eur. Phys. J. **C10**, 373 (1999), hep-ex/9903008.

[117] ZEUS Collaboration, T.Abe et al., *Exclusive electroproduction of charmonium at HERA*, Submitted to the International Europhysics Conference on High Energy Physics , Budapest, Hungary, July 12-18, 2001.

[118] J.Nemchik, N.N.Nikolaev, E.Predazzi, B.G.Zakharov and V.R.Zoller, *The diffraction cone for exclusive vector meson production in deep inelastic scattering*, J. Exp. Theor. Phys. **86**, 1054 (1998), hep-ph/9712469.

Danksagung

Es gibt eine Vielzahl an Personen, die teils direkt aber auch indirekt zum Gelingen dieser Arbeit beigetragen haben.

An erster Stelle sei hier Frau Prof. Dr. Naroska genannt. Ihr verdanke ich eine hervorragende und umfangreiche Betreuung während der gesamten Zeit dieser Arbeit. Herrn Prof. Dr. Bartels danke ich für die Erstellung des Zweitgutachtens.

Des weiteren möchte ich mich bei Katja Krüger, Duncan Brown, Benno List und Andreas Meyer bedanken, die zum Teil schon seit dem frühen Stadium der schriftlichen Arbeit als Korrekturleser hilfreich waren. Auch für zahlreiche Gespräche über die Arbeit aber auch fachfremden Themen bin ich ihnen sehr dankbar. Erweitert wurde diese Gruppe noch durch die übrigen Mitglieder der Arbeitsgruppe, die ein angenehmes Arbeitsklima ermöglichten.

Natürlich gilt auch allen anderen Mitgliedern der H1 Kollaboration mein Dank, denn ohne sie hätte es diese Arbeit niemals gegeben. Insbesondere sei hier noch Xavier Janssen genannt, der mir bei der Arbeit mit den Monte Carlo Generatoren sehr geholfen hat.

Aber nicht nur innerhalb der Kollaboration gibt es Personen die zum Gelingen der Arbeit beigetragen haben. Privat gilt daher mein Dank an erster Stelle meiner lieben Frau, die leider all zu häufig während dieser Arbeit auf gemeinsame Zeiten warten mußte und mich dennoch ständig unterstützt hat.

Natürlich möchte ich auch meinen Eltern und meinem Bruder danken, die mich schon während des Studiums kräftig unterstützt haben.

Abschließend sei noch allen anderen Freunden und Kollegen gedankt, die sich in der bisherigen Aufzählung nicht wieder gefunden haben. Ich weiß, daß ich ohne deren Mitwirken nicht in dieser Zeit zu diesem Ergebnis gekommen wäre.